# ABSTRACT

Title of Dissertation: PROPULSION-MACHINE-INTEGRATED UNIVERSAL ONBOARD CHARGERS FOR ELECTRIC VEHICLES

Chuan Shi, Doctor of Philosophy, 2018

Dissertation directed by: Professor Alireza Khaligh
Department of Electrical and Computer Engineering

Onboard level-1 and level-2 battery chargers are widely utilized in electric vehicles (EVs) for home overnight or office daytime charging. However, onboard level-1 and level-2 chargers suffer from power limitations and long charging time. On the other hand, high-power off-board chargers are utilized for fast charging, but they are bulky, expensive and require comprehensive evolution of charging infrastructures. Onboard chargers integrated with the propulsion systems of EVs provide a promising solution for fast charging of EV battery packs without contributing to additional weight and burden on the vehicle. This dissertation presents integrated charging systems, using the propulsion machine and its inverter for onboard battery charging. The proposed integrated onboard chargers do not need any modification of the propulsion systems to implement onboard battery charging. The integrated charging approaches are highly practical and applicable for commercial EVs in market. Initially, a single-phase propulsion-machine-integrated onboard charger is introduced and developed, which is capable of power factor correction (PFC) and battery voltage/current regulation without any bulky add-on passive components. The machine windings are utilized as mutually coupled inductors for PFC, and the inverter along with the machine windings constructs a two-channel interleaved boost converter. The input current ripple cancellation effect of the interleaved circuit is analyzed in detail, and the operation principles of the charging systems are presented. The feasibility of the single-phase integrated charger is proved by experimental results. Then, two approaches for three-phase propulsion-machine-integrated onboard charging are introduced and investigated. In the first approach, the charger topology is composed of a three-phase six-switch power electronics interface and the propulsion system. The proposed interface, mainly consisting of semiconductors, has small size and high power density, enabling onboard installment. The detailed operation modes of the topology are presented. In addition, the control-oriented modeling of the charging system is conducted, and a control system is designed to enable both the unity PFC and the battery voltage/current regulation. A 3.3kW prototype is designed, developed and tested for the validation of the proposed concept. The second approach is based on a three-phase three-switch power electronics interface, which is intended to be an even smaller interface. The power density of the three-switch interface increases by 40% in comparison to the first approach. The modeling and control strategy of the charging system are investigated and presented. A 5kW prototype is designed and built to validate the charging system and its control strategy.

# PROPULSION-MACHINE-INTEGRATED UNIVERSAL ONBOARD CHARGERS FOR ELECTRIC VEHICLES

by

CHUAN SHI

Dissertation submitted to the Faculty of the Graduate School of the
University of Maryland, College Park, in partial fulfillment
of the requirements for the degree of
Doctor of Philosophy
2018

Advisory Committee:
Professor Alireza Khaligh, Chair
Professor Robert W. Newcomb
Professor Neil Goldsman
Professor Pamela Abshire
Professor F. Patrick McCluskey, Dean's Representative

# Dedication

*To my parents, Duanwei and Jing.*

# Acknowledgements

I am forever grateful because of the immeasurable support, encouragement, and advice from those around me throughout the five years of my Ph.D. study. First and foremost, I would like to express my deepest gratitude to my Ph.D. advisor, Prof. Alireza Khaligh, for his guidance and support. He led me into realm of power electronics, where I found my genuine research interests. He provided me with invaluable support, constant encouragement, and insightful comments. From him, I learned more than I could ever have asked for. I would also like to thank my family members, who have supported me from the beginning of this academic journey. You were there for me when I encountered difficulties and there to share the joy of my accomplishments. I hope the completion of this degree makes you proud. I am very grateful to Prof. Robert W. Newcomb, Prof. Neil Goldsman, Prof. Pamela Abshire, and Prof. Patrick McCluskey for their attendance of my dissertation defense. I would also like to express my gratitude to my brilliant colleagues in the Maryland Power Electronics Laboratory (MPEL) for their insightful comments and technical suggestion on my research. This work is sponsored by the National Science Foundation (NSF) award number 1507546 (GOALI: Integrated On-Board Universal SiC-based Fast Charging for Plug-In Electric Vehicles), which is gratefully acknowledged.

# Table of Contents

# List of Tables

# List of Figures

# Chapter 1: Introduction

The battery chargers for electric vehicles (EVs) can be divided into three power levels: level 1, level 2 and level 3 [1], [2]. The level 1 and level 2 chargers are generally used to charge the battery packs of EVs at home or office. The level 3 chargers are commonly installed in charging stations, such as parking lots and shopping centers [3]. Alternatively, based on the installation location, the EV battery chargers can be sorted as on-board and off-board chargers. The onboard chargers usually utilize the level 1 or level 2 single-phase charging. On the other hand, the level 3 charging is usually adopted for the off-board chargers. Typically, all these chargers are composed of two stages: a AC-DC stage for rectifying the grid AC voltage with power factor correction (PFC) and a DC-DC stage for battery current/voltage regulation [4]-[6].

## 1.1 Motivation

The onboard and off-board battery chargers for an EV are illustrated in Figure 1.1. Conventional onboard and off-board chargers have their own advantages and challenges. Using conventional level-1 and level-2 onboard chargers, it takes a long time (between 4 to 20 hours) to fully charge a typical 24kWh EV battery pack [3], [7] due to their charging power limitations. The typical power levels for level-1 onboard chargers are 1.4kW and 1.9kW. The typical power levels of level-2 onboard chargers are 3.3kW and 6.6kW [8]. Three-phase off-board chargers have the capability of DC fast charging of EVs [9]-[12]. It takes around 30min to fully charge a typical 24kWh battery pack using a 40kW three-phase off-board charger [13]. However, three-phase off-board chargers are large, expensive and require a comprehensive evolution of charging infrastructures.

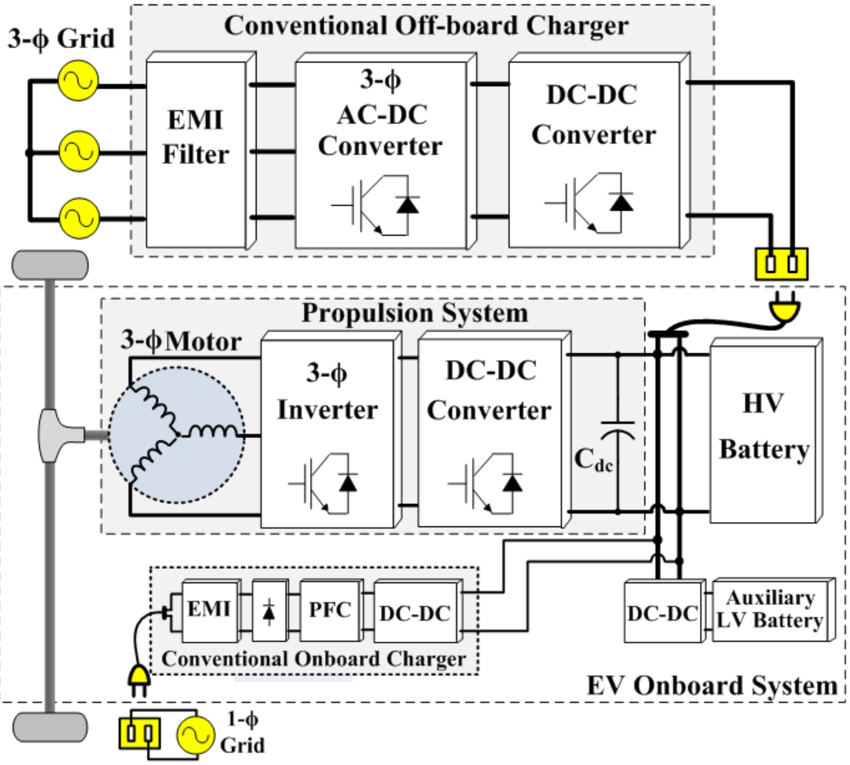

Figure 1.1. Conventional power electronics interfaces for an electric vehicle.

The typical propulsion system of an EV is composed of a propulsion machine, an inverter, an optional DC-DC converter, and battery packs. All these components are rated at high power, comparable to the level 3 battery charging power levels. Generally, commercial EVs utilize three-phase AC machines, which are mainly induction machines (IM) or permanent magnet synchronous machines (PMSM) for electric propulsion, such as the 310-kW IM for Tesla Model S, the 115-kW IM for Toyota Rav4 EV, the 80-kW PMSM for Nissan Leaf, and the 111-kW PMSM for Chevy Volt [14]-[16]. In a three-phase propulsion system, the bidirectional three-phase inverter should be designed at the same power level as the propulsion machine. The inverter enables the energy flow from the battery to the propulsion machine in propulsion mode and back to the battery via regenerative braking [14]. Since the battery voltage has a wide range of variations in charging mode, a bidirectional DC-DC converter is optionally utilized to regulate the DC-link voltage of the inverter (typically 360 V or 720 V [17]), which is designed to be higher than the peak voltage over the propulsion machine considering the overall efficiency of the propulsion system.

A propulsion-machine-integrated onboard charger not only provides high-power charging without substantial addition of cost and weight, but also simplifies the evolution of high-power charging infrastructures.

## 1.2 Challenges of integrated onboard chargers

The challenges in enabling propulsion-machine-integrated onboard chargers are addressed as follows.

1. **Applicable to commercial EVs in market.** The topologies of integrated chargers should be applicable to commercial EVs in market. The integrated charging approach should not require the access to the inaccessible terminals of EVs, such as the neutral point of the machine windings. Moreover, no multi-phase propulsion systems, such as six-phase or nine-phase propulsion systems, should be allowed to do integrated charging for EVs for the reason that only three-phase propulsion systems are utilized in the commercial EVs. In addition, the specially-designed multi-phase machines and multi-phase inverters increase the cost and complexity of the overall system.

2. **Maintain high efficiency.** Integrated onboard chargers should maintain high efficiencies as conventional chargers. No contactors should be used to rearrange the connection of the machine windings and the inverter in transition from charging mode to propulsion mode since the usage of contactors causes additional large power loss. Moreover, rearrangement of circuits increases the system complexity and reduces the system reliability.

3. **No rotation of the propulsion machine during charging.** In charging mode, the rotor of the propulsion machine is not allowed to rotate.

## 1.3 Proposed Approaches and Contributions

### 1.3.1 Single-Phase Integrated Charger

Single-phase integrated charging approaches have been investigated in previous research. The integrated charging approaches in [18]-[23] require the access to the normally inaccessible neutral point of the machine windings for battery charging, and the integrated charger in [24] need the access to the inaccessible middle points of machine windings for battery charging. In fact, other than the phase-terminals of the machine and the two terminals of the DC-link capacitor, other terminals, such as the neutral point and the mid-points of machine windings, are inaccessible for the traditional there-phase propulsion systems of EVs in market. The traditional propulsion machines have to be specially designed to provide access to the aforementioned inaccessible terminals. Thus, the existing integrated chargers are not applicable for EVs in market.

The integrated chargers in [25]-[27] utilize the six-phase or nine-phase propulsion systems, which are rarely applied in commercial EVs. The integrated chargers in [28] use contactors to rearrange the connection of the machine windings and the inverter for integrated charging, resulting in low efficiency. An integrated topology was proposed in [29], but the rotor would rotate when the system were affected by a small disturbance. The integrated chargers in [30], [31] use specially-designed split-winding machines to enable integrated charging, and the propulsion machine would rotate if the parameters have tiny deviations from the theoretical values. The existing integrated charging approaches, mostly for single-phase integrated charging [32]-[35], are complex and usually require access to the inaccessible points of propulsion systems.

To solve these limitations, a novel single-phase integrated onboard charger is proposed, which is composed of an add-on passive diode bridge and the propulsion system. As illustrated in Figure 1.2, a diode bridge is connected between a phase terminal of the propulsion machine (phase A for example) and the negative terminal of the inverter's DC-link. The proposed scheme is applicable for any three-phase AC propulsion system and only needs access to phase terminals (A, B, C) of propulsion machines, which is feasible for all the commercial EVs in the market.

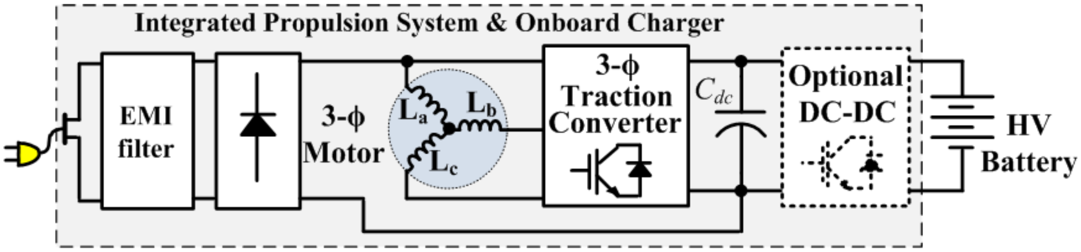

Figure 1.2. Proposed single-phase integrated charger using propulsion system.

**1$^{st}$ Contributions**: The first practical single-phase propulsion-machine-integrated onboard charger for EVs is proposed, investigated and implemented. The proposed integrated charging method only needs an add-on diode bridge, which is connected to two terminals of an EV propulsion system to construct the single-phase integrated charger. Bulky passive components, such as large PFC inductors and DC-link capacitors, are not required. There is no need for rearrangement of the circuit in transition from the propulsion mode to the charging mode. The proposed method reduces the cost of implementing high-power integrated charging and significantly reduces the size of the integrated charging system.

### 1.3.2 Three-Phase Integrated Chargers with a Six-Switch Interface

For the three-phase integrated charging, a few approaches have been proposed before in literature [8], [36]. These approaches have similar limitations as previous single-phase ones. In [37], a three-phase integrated charging approach using two PMSMs was proposed. The neutral point of the machine windings is needed for integrated charging, and propulsion systems have to be modified to provide the neutral point as an accessible external terminal.

In [38], a three-phase integrated charging approach was proposed. A contactor was introduced to reconfigure the connection of machine windings. However, the contactor, between the machine windings and the power mains, causes additional power loss and increases the control complexity.

The three-phase integrated chargers in [39] require specially-designed split-winding electric machines to construct the charging circuit. The two half-windings of each phase are in opposite space distribution, which cancel the torque in each phase. Thus, there is no torque generation during charging. However, the midpoints of machine windings are not accessible for conventional EV propulsion systems.

The three-phase integrated chargers proposed in [40] suffer from torque generation in charging mode. In order to solve this issue, the integrated chargers using multiphase machines were proposed in [41]. However, special multiphase machines and multiphase inverters are required. These integrated charging approaches are not suitable for the EVs, where conventional three-phase propulsion systems dominate.

Table 1.1 summarizes the state-of-the-art three-phase integrated charging approaches, which are categorized into three types based on the method of integration. The limitations of each type are analyzed as well.

**2nd Contribution:** A practical three-phase integrated onboard charger with six-switch interface is proposed for three-phase onboard charging. The proposed three-phase six-switch power electronics interface, mainly composed of semiconductors, is connected between one phase-terminal of the propulsion machine and the negative terminal of the battery pack, as shown in Figure 1.3. The propulsion machine is utilized as three coupled inductors, and the power switches of the inverter are utilized to construct the integrated charger. The configuration of the integrated charger is simple, directly connecting the three-phase interface to two terminals of the propulsion system. Additionally, a control strategy is designed and implemented for the proposed system.

Table 1.1

State-of-art high-power integrated chargers

| Approach Category | Topology | Issues |
|---|---|---|
| **1.Multi-phase Propulsion System** | 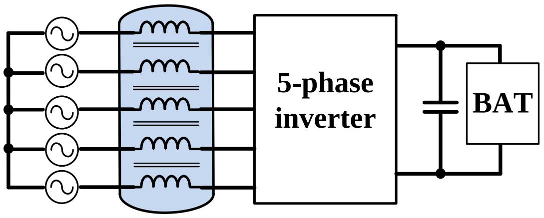 | • Special multiple-phase propulsion system is needed<br>• Access to the neutral point is needed |
| **2.Split-winding Propulsion Machines** | 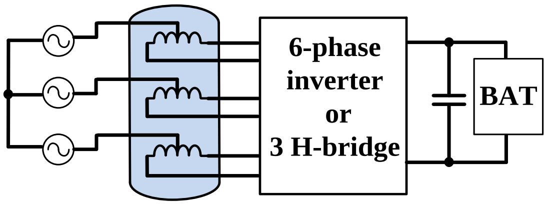 | • Access to the mid-points of windings is needed<br>• Specially-designed machine is required |
| **3.Reconfiguration of Machine Windings** | 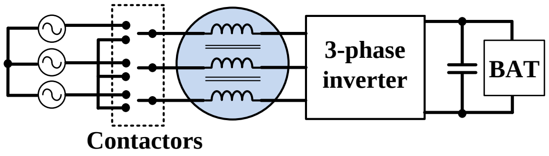 | • Contactors are needed.<br>• Additional power loss is caused by contactors |

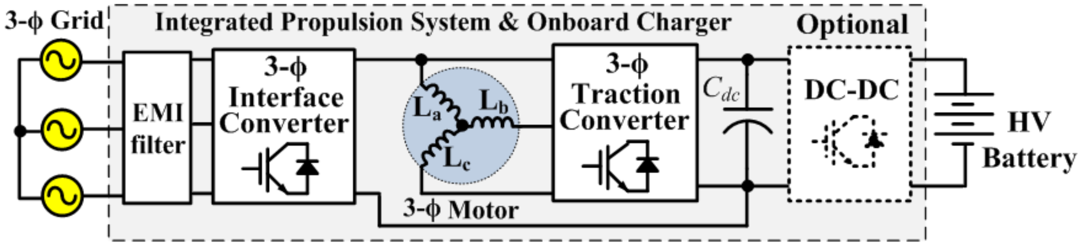

Figure 1.3. Schematic of the proposed three-phase integrated charger for EVs.

### 1.3.3 Three-Phase Integrated Chargers with a Three-Switch Interface

To further reduce the size and weight of the integrated charger, an integrated three-phase onboard charger with three-phase three-switch interface was proposed.

The three-phase interface is only composed of power semiconductors without any bulky inductor or capacitor (except the small size input EMI filter). The machine windings serve as coupled inductors for the integrated charging system.

**3rd Contribution:** A three-phase integrated charger with three-switch interface is proposed for three-phase onboard charging. The three-phase interface only needs three active power switches, simplifying the system and further reducing the size of the integrated charger. Furthermore, a control strategy is proposed and implemented, enabling the control of the input current, machine-winding currents and the battery voltage.

Compared with the traditional integrated chargers, the proposed single-phase and three-phase propulsion-machine-integrated chargers possess all the following advantages:

(i) integrated onboard battery charging,
(ii) onboard single-phase / three-phase interface of small size,
(iii) no need for machine/inverter rearrangement,
(iv) no need for access to inaccessible points of machine windings,
(v) no rotation of propulsion machine during charging.

## 1.4 Overview

The contents of this dissertation are divided into five chapters to discuss the integrated chargers for EVs. In Chapter 2, the operation principles and the design of the first proposed single-phase integrated onboard charger are presented. The electrical model of the propulsion machine is discussed to derive the equivalent inductances of the machine windings in the battery-charging mode. The steady-state analysis of charging operation is also presented. In addition, experimental results are provided for validation of the single-phase integrated charger. In Chapter 3, the three-phase integrated onboard charger with six-switch interface is investigated. The operation modes and steady-state characteristics are theoretically analyzed based on a comprehensive modeling of the circuit. Moreover, the control strategy of the three-phase integrated charger is discussed. A proof-of-concept prototype is developed to verify the three-phase integrated charging and the proposed control strategy.

In Chapter 4, the three-phase integrated charger with six-switch interface is investigated. The operational modes of the integrated charger are discussed in detail. The design of the cascaded control strategy is provided based on the small signal modeling of the circuit. Furthermore, a prototype is developed for validation of the proposed integrated charger and its control strategy. Chapter 5 presents the conclusions and the future work of the propulsion-machine-integrated onboard chargers for EVs.

# Chapter 2: Single-Phase Propulsion-Machine Integrated Charger

The topology of the proposed single-phase propulsion-machine integrated onboard charger is shown in Figure 2.1. The propulsion machine serves as a three-winding mutually-coupled inductor for energy storage and ripple cancellation. The machine windings and the inverter construct a two-channel interleaved boost converter. The diode bridge along with the propulsion system develops an AC-DC PFC converter, capable of output voltage/current regulation.

One of the three-phase inverter bridges, $S_1/S_2$ bridge for example, is connected to the positive terminal of the diode bridge rectifier. In this case, the $S_1/S_2$ bridge is disabled, while the other two bridges, $S_3/S_4$ and $S_5/S_6$, are utilized to develop an interleaved boost converter.

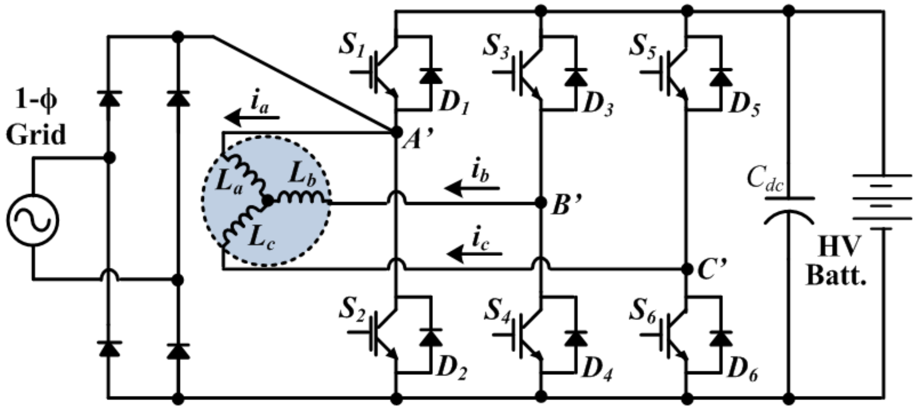

Figure 2.1. Proposed single-phase integrated onboard charger using propulsion system.

In propulsion mode, the high-voltage (HV) battery pack provides the propulsion power through three-phase inverter to the propulsion machine as shown in Figure 2.2(a), and the add-on diode bridge has no impact on the inverter operation. In charging mode, the grid ac line voltage is rectified by the diode-bridge as shown in

Figure 2.2(b), and the machine windings along with the inverter develop a two-channel interleaved boost converter, capable of PFC and output voltage/current regulation. $S_1$ and $S_2$ are kept open in charging mode. The body diode $D_2$ is reverse biased by the positive output voltage of the diode bridge rectifier. As for $D_1$, it only turns on to charge the output capacitor during the start-up when the output capacitor voltage is lower than the input voltage. In steady state, $D_1$ is reverse biased since the output voltage is higher than the input voltage, due to the boost operation of the converter. Considering the total harmonic distortion (THD) requirement of a grid, the converter is operated in the continuous conduction mode (CCM).

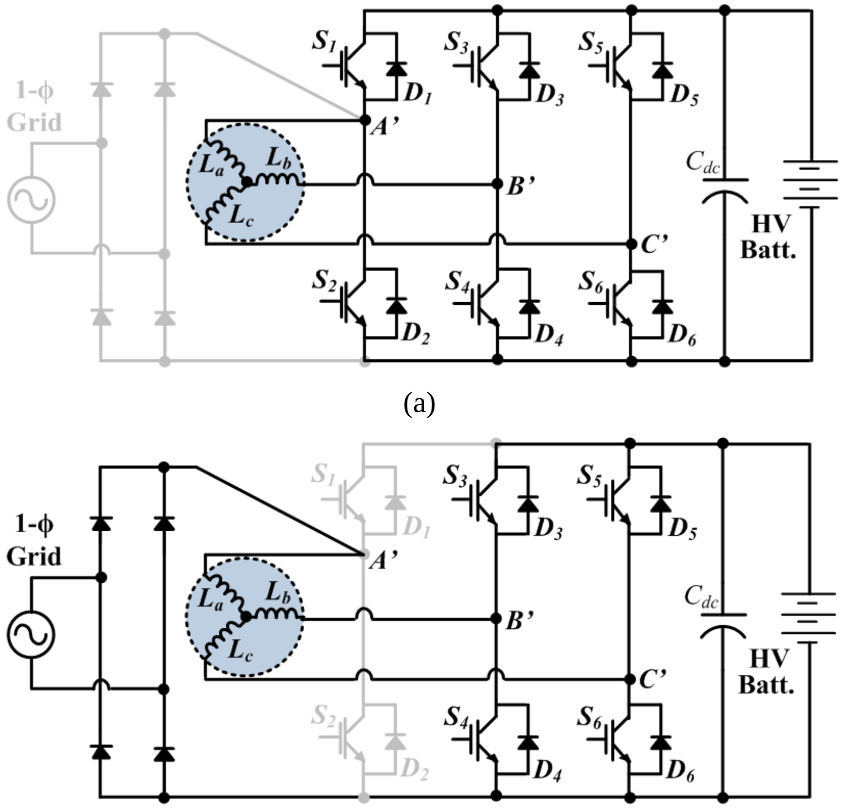

(a)

(b)

Figure 2.2. Operation modes of single-phase integrated onboard charger with propulsion machine: (a) propulsion mode; (b) charging mode.

## 2.1 Electrical Model of Propulsion Machine

PMSMs are dominant propulsion machine options for EVs [42]-[44], due to the advantages in terms of high power density, high efficiency and light weight/volume ratio [45]. Usually, the round-rotor structure is utilized for high-efficient operation at high rotating speeds (1500rpm–14000rpm or even higher), which is the case for EV applications [15]. Therefore, the integration theory is focused on the propulsion system using a round-rotor PMSM. In fact, the proposed approach is simply extendable to any other ac propulsion machine.

The general mathematical model of a three-phase PMSM [46] is utilized based on two assumptions that: the magneto-motive forces (MMF) of stator windings are sinusoidally distributed in the air gap; and hysteresis effects and the eddy current are neglected. Park's transformation is utilized to convert the stationary-frame quantities to rotating-frame quantities, which simplifies the analyses of three-phase electrical model [47]. Figure 2.3(a) presents a conceptual cross-sectional view of a 3-phase, 4-pole PMSM along with two reference frames (a-b-c frame and d-q frame). In this model, $\theta_r$ is the rotor angle between a-axis and q-axis in radians; $\omega=d\theta_r/dt$ is the angular velocity of rotation in rad/sec; $P_l$ is the number of pole pairs; and $\theta_e = P_l\theta_r$ is the electrical angle between a-axis and q-axis. The corresponding three-phase electrical model is illustrated in Figure 2.3(b). $i_a$, $i_b$ and $i_c$ are instantaneous phase currents; $v_a$, $v_b$ and $v_c$ are the instantaneous phase voltages; $R_s$ is the machine-winding resistance; $L_{aa}$, $L_{bb}$ and $L_{cc}$ denote the a-axis, b-axis and c-axis self-inductances of machine windings; and $L_{ab}$, $L_{ac}$ and $L_{bc}$ denote mutual inductances describing the coupling effects among the machine windings. In a stationary condition, the initial electrical angle, $\theta_e$, is assumed to be $\pi/2$, and the d-axis is aligned with the a-axis.

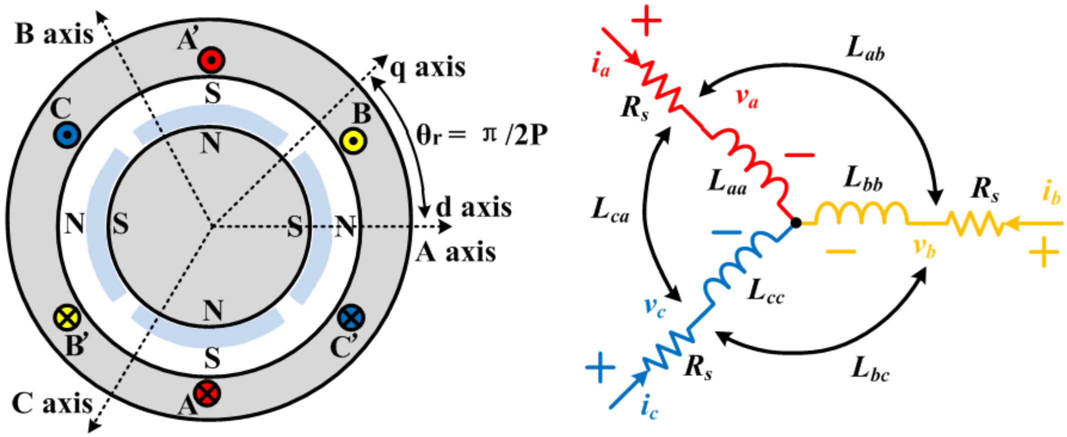

(a) (b)

Figure 2.3. (a) Cross section of a PMSM; (b) simplified electrical model of a PMSM.

Based on the d-q equivalent circuit model of a PMSM, the three-phase self and mutual inductances can be derived with respect to the d-axis and q-axis equivalent inductances, $L_d$ and $L_q$ [48], in Eq. (2.1) – Eq. (2.6).

$$\begin{cases} L_{aa} = L_s + L_x \cos(2\theta_e) & (2.1) \\ L_{bb} = L_s + L_x \cos(2\theta_e + \frac{2\pi}{3}) & (2.2) \\ L_{cc} = L_s + L_x \cos(2\theta_e - \frac{2\pi}{3}) & (2.3) \\ L_{ab} = -M_s + L_x \cos(2\theta_e - \frac{2\pi}{3}) & (2.4) \\ L_{bc} = -M_s + L_x \cos(2\theta_e) & (2.5) \\ L_{ac} = -M_s + L_x \cos(2\theta_e + \frac{2\pi}{3}) & (2.6) \end{cases}$$

where, the average inductance $L_s$ is equal to $1/2(L_q+L_d)$; the inductance fluctuation $L_x$ is equal to $1/2(L_q-L_d)$; the average mutual inductance $M_s$ is equal to $-(L_{ab}+L_{bc}+L_{ac})/3$; and the electrical angle between a-axis and q-axis $\theta_e$ is equal to $P\theta_r$.

In the model of the propulsion machine, the electrical dynamic equations in terms of instantaneous phase voltages $v_a$, $v_b$ and $v_c$ are derived as,

$$\begin{cases} v_a = R_s i_a + \dfrac{\partial \lambda_a}{\partial t} & (2.7) \\ v_b = R_s i_b + \dfrac{\partial \lambda_b}{\partial t} & (2.8) \\ v_c = R_s i_c + \dfrac{\partial \lambda_c}{\partial t} & (2.9) \end{cases}$$

where, $\lambda_a$, $\lambda_b$, and $\lambda_c$ are stator flux linkages, subject to Eq. (2.10) – Eq. (2.12).

$$\begin{cases} \lambda_a = L_{aa} i_a + L_{ab} i_b + L_{ac} i_c + \lambda_{ma} & (2.10) \\ \lambda_b = L_{ab} i_a + L_{bb} i_b + L_{bc} i_c + \lambda_{mb} & (2.11) \\ \lambda_c = L_{ac} i_a + L_{bc} i_b + L_{cc} i_c + \lambda_{mc} & (2.12) \end{cases}$$

where, $\lambda_{ma}$, $\lambda_{mb}$, and $\lambda_{mc}$ are the flux linkages of rotor permanent magnets.

According to Kirchhoff's Current Law (KCL), the instantaneous phase currents are subject to Eq. (2.13).

$$i_a + i_b + i_c = 0 \tag{2.13}$$

Hence, substituting Eq. (2.1) - (2.6) and Eq. (2.13) into Eq. (2.7) - (2.12), the instantaneous phase voltages $v_a$, $v_b$ and $v_c$ can be derived as Eq. (2.14) - (2.16).

$$\begin{cases} v_a = R_s i_a + L_1 \dfrac{\partial i_a}{\partial t} & (2.14) \\ v_b = R_s i_b + L_2 \dfrac{\partial i_b}{\partial t} + L_3 \dfrac{\partial i_c}{\partial t} & (2.15) \\ v_c = R_s i_c + L_2 \dfrac{\partial i_c}{\partial t} + L_3 \dfrac{\partial i_b}{\partial t} & (2.16) \end{cases}$$

where, $L_1$, $L_2$ and $L_3$ are equivalent inductances in terms of $L_d$, $L_q$ and $M_s$,

$$\begin{cases} L_1 = \frac{5}{4}L_d - \frac{1}{4}L_q + M_s & (2.17) \\ L_2 = \frac{1}{2}L_d + \frac{1}{2}L_q + M_s & (2.18) \\ L_3 = \frac{3}{4}L_d - \frac{3}{4}L_q & (2.19) \end{cases}$$

Therefore, the mutual effect exists between the machine windings of phase-B and phase-C; however, it has no influence on the machine winding of phase-A. The phase voltages are subject to Eq. (2.20).

$$v_a + v_b + v_c = 0 \tag{2.20}$$

For round-rotor PMSMs, the d-axis equivalent inductance $L_d$ is theoretically equal to the q-axis equivalent inductance $L_q$. In this case, $L_1$ and $L_2$ are equal to $L_{aa}+M_s$, and $L_3$ is equal to 0. Thus, Eq. (2.21) - (2.23) can be obtained based on Eq. (2.14) - (2.16).

$$\begin{cases} v_a = R_s i_a + (L_{aa} + M_s)\frac{\partial i_a}{\partial t} & (2.21) \\ v_b = R_s i_b + (L_{aa} + M_s)\frac{\partial i_b}{\partial t} & (2.22) \\ v_c = R_s i_c + (L_{aa} + M_s)\frac{\partial i_c}{\partial t} & (2.23) \end{cases}$$

Equations (2.21)-(2.23) indicate that in a stationary condition the machine winding of each phase serves as a discrete inductor with the equal inductance as $L_{aa}+M_s$. The phase currents are functions of multiple independent variables to give which, partial derivatives are used to derive the equations.

## 2.2 Charging Operation Using Propulsion Machine

In charging mode, the switching operation is similar to that of a two-channel interleaved boost with two discrete inductors or one inversely coupled inductor [26]. The interleaved bridges ($S_3$/$S_4$ and $S_5$/$S_6$) operate with 180-degree temporal phase shift. However, in comparison to conventional interleaved boost converters, the proposed converter has 120-degree spatial out-of-phase distributed machine windings ($L_a$, $L_b$, $L_c$), which result in different steady-state equivalent inductances in different switching states. During one switching period, there are four switching states (I)-(IV), as shown in Figure 2.4.

CCM operation is selected for the inductor currents. For high power-level applications, CCM operation is more suitable for the converter considering the current stresses of the components. In many EVs (such as Prius Hybrid, Camry hybrid, Fusion hybrid and Nissan Leaf EV), a bidirectional DC-DC converter is designed between the three-phase inverter and the battery to regulate the DC-link voltage of inverter when the battery voltage is lower than its rated voltage due to low SoC (state of charge) [8], [49] - [51]. In charging mode, this optional bidirectional DC-DC converter serves as a buck converter to step down the DC-link voltage of the inverter when the battery voltage is lower than the peak input AC voltage.

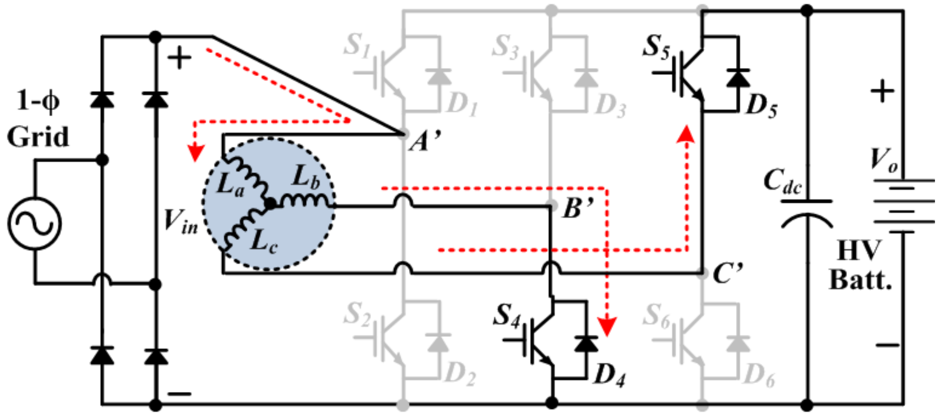

(I)

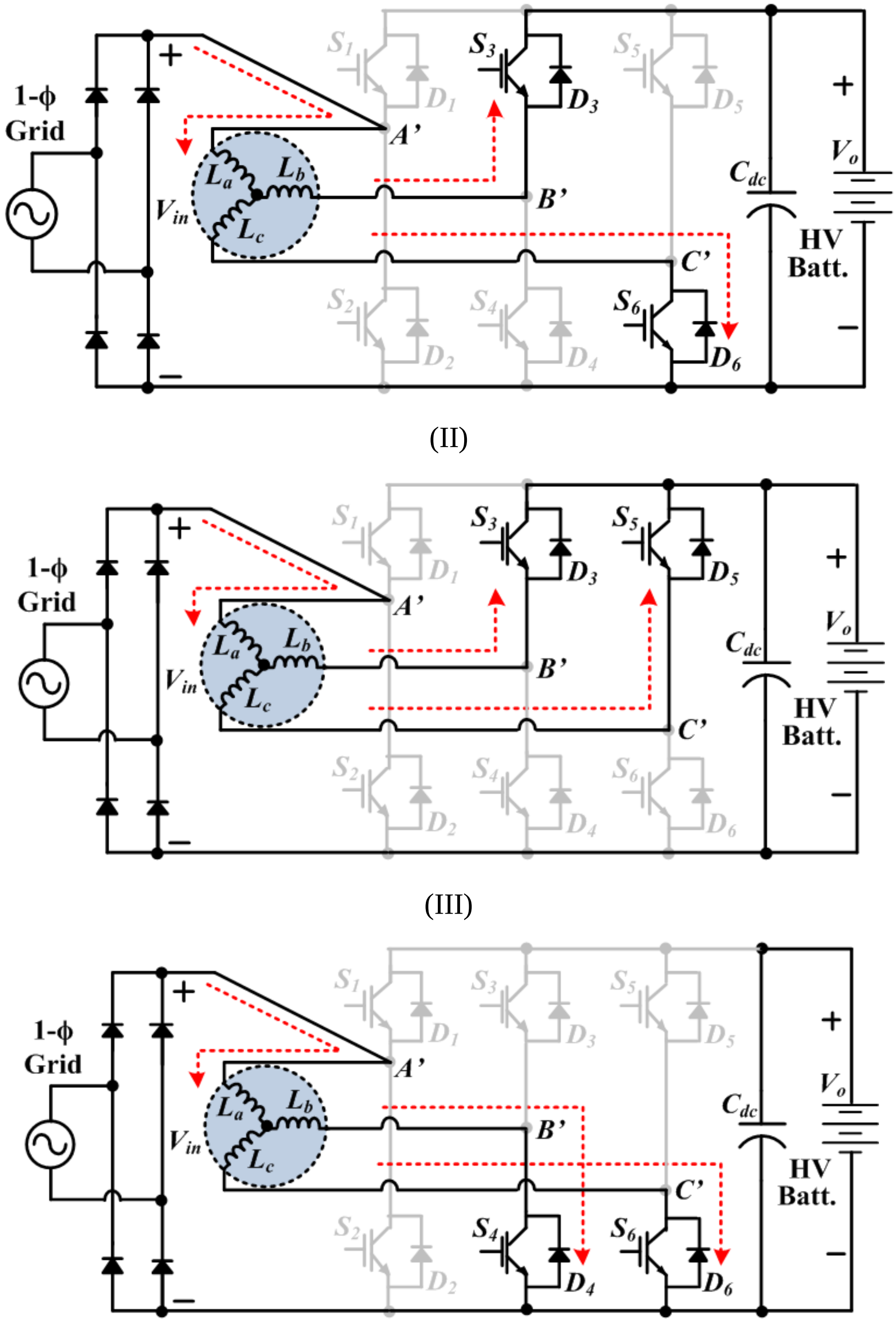

(II)

(III)

(IV)

Figure 2.4. Switching states (I)~(IV) in the charging mode.

### 2.2.1 Switching States

Based on the switching duty cycle ($D$), the steady-state operation is categorized into two cases: *(i)* $0<D<0.5$, in which $V_o<2V_{in}<2V_o$; and *(ii)* $0.5<D<1$, where $V_o>2V_{in}$. When $0<D<0.5$, the circuit operation has a periodical switching sequence of (I)-(III)-(II)-(III)-(I). Machine-winding currents and switches corresponding to different switching states are illustrated in Figure 2.5.

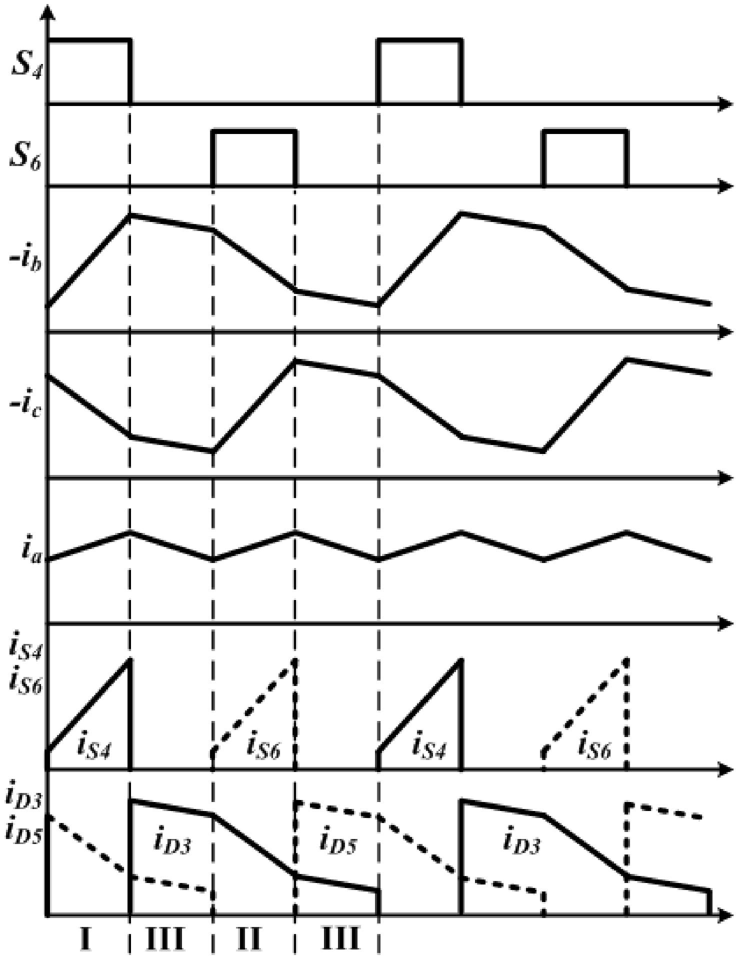

Figure 2.5. Current waveforms of the integrated charger with PMSM (round rotor) during charging 0<D<0.5.

When 0.5<*D*<1, the switching sequence changes to (I)-(IV)-(II)-(IV)-(I). Machine-winding currents and switches corresponding to different switching states are illustrated in Figure 2.6.

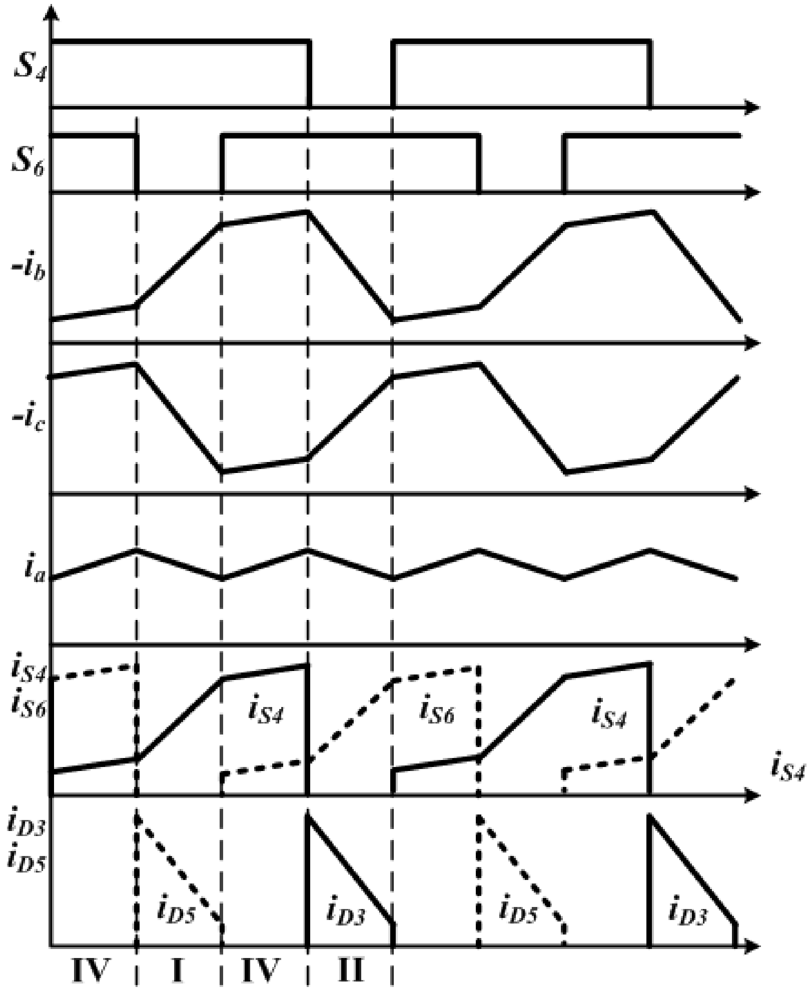

Figure 2.6. Current waveforms of the integrated charger with PMSM (round rotor) during charging 0.5<D<1.

In State I, the switch, $S_4$, is turned on; and the diode of the second channel, $D_5$, conducts the inductor current.

$$\begin{cases} v_a - v_b = V_{in} & (2.24) \\ v_a - v_c = V_{in} - V_o & (2.25) \end{cases}$$

where, $V_a$, $V_b$ and $V_c$ are the voltages at the phase terminals A, B and C of the machine; $V_{ac}$ and $V_o$ are the input and output voltages of the interleaved boost converter. Using Eq. (2.20), Eq. (2.24) and Eq. (2.25), the phase voltages in State I can be derived in Eq. (2.26) – Eq. (2.28).

$$\begin{cases} v_a{}^I = \dfrac{2V_{in} - V_o}{3} & (2.26) \\ v_b{}^I = -\dfrac{V_{in} + V_o}{3} & (2.27) \\ v_c{}^I = -\dfrac{V_{in} - 2V_o}{3} & (2.28) \end{cases}$$

According to Eq. (2.21) - (2.23), the machine-winding currents can be represented as Eq. (2.29) - Eq. (2.31), ignoring the machine-winding resistance ($R_s=0$).

$$\begin{cases} \dfrac{\partial i_a{}^I}{\partial t} = \dfrac{2V_{in} - V_o}{3(L_{aa} + M_s)} & (2.29) \\ -\dfrac{\partial i_b{}^I}{\partial t} = \dfrac{V_{in} + V_o}{3(L_{aa} + M_s)} & (2.30) \\ -\dfrac{\partial i_c{}^I}{\partial t} = \dfrac{V_{in} - 2V_o}{3(L_{aa} + M_s)} & (2.31) \end{cases}$$

Hence, in a round-rotor PMSM, the equivalent machine-winding inductance is three times the sum of self-inductance and mutual-inductance. For $0<D<0.5$, ($V_o<2V_{in}<2V_o$), $i_a$ and $-i_b$ increase linearly, and $-i_c$ decreases linearly. For $0.5<D<1$ ($2V_{in}<V_o$), $i_a$ and $-i_c$ decrease linearly, and $-i_b$ increases linearly.

In State II, the switch $S_6$, is turned on; and the diode, $D_3$, conducts the inductor current. In this state: $v_a^{II}=v_a^{I}$, $v_b^{II}=v_c^{I}$, $v_c^{II}=v_b^{I}$. For a round-rotor PMSM, the machine-winding currents can be expressed as,

$$\begin{cases} \dfrac{\partial i_a{}^{II}}{\partial t} = \dfrac{2V_{in} - V_o}{3(L_{aa} + M_s)} & (2.32) \\ -\dfrac{\partial i_b{}^{II}}{\partial t} = \dfrac{V_{in} - 2V_o}{3(L_{aa} + M_s)} & (2.33) \\ -\dfrac{\partial i_c{}^{II}}{\partial t} = \dfrac{V_{in} + V_o}{3(L_{aa} + M_s)} & (2.34) \end{cases}$$

State III only exists when $0<D<0.5$. It occurs between State I and State II. In this state, both transistors of two legs, $S_4$ and $S_6$, are turned off; and diodes of two legs, $D_3$ and $D_5$, conduct currents.

$$\begin{cases} v_a - v_b = V_{in} - V_o & (2.35) \\ v_a - v_c = V_{in} - V_o & (2.36) \end{cases}$$

yielding,

$$\begin{cases} v_a^{III} = \dfrac{2(V_{in} - V_o)}{3} & (2.37) \\ v_b^{III} = v_c^{III} = -\dfrac{V_{in} - V_o}{3} & (2.38) \end{cases}$$

For a round-rotor PMSM, $i_a$, $-i_b$ and $-i_c$ decrease linearly due to their equivalent discrete inductor. In this state, the slope of $i_a$ is twice the slopes of $-i_b$ and $-i_c$.

$$\begin{cases} \dfrac{\partial i_a^{III}}{\partial t} = \dfrac{2(V_{in} - V_o)}{3(L_{aa} + M_s)} & (2.39) \\ -\dfrac{\partial i_b^{III}}{\partial t} = -\dfrac{\partial i_c^{III}}{\partial t} = \dfrac{V_{in} - V_o}{3(L_{aa} + M_s)} & (2.40) \end{cases}$$

State IV only exists when *0.5<D<1*. It happens right between Mode I and Mode II. In this state, both switches, $S_4$ and $S_6$, are turned on; diodes, $D_3$ and $D_5$, are reverse biased. The same voltage, $V_{ac}$, appears across the stator windings.

$$\begin{cases} v_a - v_b = V_{in} & (2.41) \\ v_a - v_c = V_{in} & (2.42) \end{cases}$$

Thus, the phase voltages can be derived as,

$$\begin{cases} v_a^{IV} = \dfrac{2V_{in}}{3} & (2.43) \\ v_b^{IV} = v_c^{IV} = -\dfrac{V_{in}}{3} & (2.44) \end{cases}$$

In the particular case of a round rotor, the phase currents can be written as,

$$\begin{cases} \dfrac{\partial i_a^{IV}}{\partial t} = \dfrac{2V_{in}}{3(L_{aa}+M_s)} & (2.45) \\ -\dfrac{\partial i_b^{IV}}{\partial t} = -\dfrac{\partial i_c^{IV}}{\partial t} = \dfrac{V_{in}}{3(L_{aa}+M_s} & (2.46) \end{cases}$$

### 2.2.2 Steady State Analyses

Since the rectified input current $|i_{in}|$ is equal to $i_a$, based on Eq. (2.29) and Eq. (2.39), the input current ripple $|\Delta i_{in}|$ for *0<D<0.5* can be derived as,

$$|\Delta i_{in}| = \frac{2V_{in} - V_o}{3(L_{aa}+M_s)} DT = -\frac{2(V_{in} - V_o)}{3(L_{aa}+M_s)}(0.5-D)T \qquad (2.47)$$

For *0.5<D<1*, the input current ripple can be found from Eq. (2.29) and Eq. (2.45),

$$\left|\Delta i_{in}\right| = -\frac{2V_{in} - V_o}{3(L_{aa}+M_s)}(1-D)T = \frac{2V_{in}}{3(L_{aa}+M_s)}(D-0.5)T \tag{2.48}$$

Therefore, the steady-state output-to-input voltage gain $A_v$ can be derived as,

$$A_v = \frac{V_o}{V_{in}} = \frac{1}{1-D} \tag{2.49}$$

The output-to-input voltage gain is the same as that of a conventional interleaved boost converter. The input current ripple can be written as,

$$\left|\Delta i_{in}\right| = \begin{cases} \dfrac{D(1-2D)}{1-D}\dfrac{V_{in}}{3(L_{aa}+M_s)f_s}, 0 < D < 0.5 & (2.50) \\ (2D-1)\dfrac{V_{in}}{3(L_{aa}+M_s)f_s}, 0.5 < D < 1 & (2.51) \end{cases}$$

Seen from Eq. (2.50) and Eq. (2.51), the input current ripple is suppressed by the equivalent inductance equal to the sum of self-inductance and mutual inductance of machine windings.

On the other hand, the current ripples of phase-B and phase-C currents are the same due to the symmetric operation condition of two interleaved channels. The current ripples can be quantified in Eq. (2.52).

$$\left|\Delta i_{b,c}\right| = \begin{cases} \dfrac{D(2-D)}{1-D}\dfrac{V_{in}}{3(L_{aa}+M_s)f_s}, 0 < D < 0.5 & (2.52) \\ (2-D)\dfrac{V_{in}}{3(L_{aa}+M_s)f_s}, 0.5 < D < 1 & (2.53) \end{cases}$$

In steady state, the input power is equal to the output power with an equivalent load resistance, $R_L$. Thus, the RMS value of the input current is derived as,

$$I_{in} = \frac{V_o^2}{R_L V_{in}} = \frac{V_{in}}{(1-D)^2 R_L} \tag{2.54}$$

Thus, the maximum value and minimum value of rectified input current can be calculated based on the average input current $I_{in}$ and the input current ripple $|\Delta i_{in}|$, for $0<D<0.5$, as

$$\begin{cases} I_{in,\max} = I_{in} + \dfrac{1}{2}\left|\Delta i_{in}\right| = [\dfrac{1}{(1-D)^2 R_L} + \dfrac{D}{1-D}\dfrac{1-2D}{6(L_{aa}+M_s)f_s}]V_{in} & (2.55) \\ I_{in,\min} = I_{in} - \dfrac{1}{2}\left|\Delta i_{in}\right| = [\dfrac{1}{(1-D)^2 R_L} - \dfrac{D}{1-D}\dfrac{1-2D}{6(L_{aa}+M_s)f_s}]V_{in} & (2.56) \end{cases}$$

For $0.5<D<1$, the maximum value and minimum value are expressed as,

$$\begin{cases} I_{in,\max} = I_{in} + \dfrac{1}{2}\left|\Delta i_{a}\right| = [\dfrac{1}{(1-D)^2 R_L} + \dfrac{2D-1}{6(L_{aa}+M_s)f_s}]V_{in} & (2.57) \\ I_{in,\min} = I_{in} - \dfrac{1}{2}\left|\Delta i_{a}\right| = [\dfrac{1}{(1-D)^2 R_L} - \dfrac{2D-1}{6(L_{aa}+M_s)f_s}]V_{in} & (2.58) \end{cases}$$

For comparison, the maximum and minimum input currents of the traditional single-channel boost converter are shown in Eq. (2.59) - Eq. (2.60).

$$\begin{cases} I_{in,max} = I_{in} + \dfrac{1}{2}(\Delta I_{in}) = \left[\dfrac{1}{(1-D)^2 R_L} + \dfrac{D}{Lf_s}\right] V_{in} & (2.59) \\ I_{in,min} = I_{in} - \dfrac{1}{2}(\Delta I_{in}) = \left[\dfrac{1}{(1-D)^2 R_L} - \dfrac{D}{Lf_s}\right] V_{in} & (2.60) \end{cases}$$

The effectiveness of ripple cancellation can be represented as the normalized current ripple, $\gamma(D)$, expressed as a function of duty cycle in Eq. (2.61) – Eq. (2.62).

$$\gamma(D) = \frac{\left|\Delta i_{in}\right|}{\left|\Delta i_{b,c}\right|} = \begin{cases} \dfrac{1-2D}{2-D}, 0 < D \le 0.5 & (2.61) \\ \dfrac{2D-1}{2-D}, 0.5 < D < 1 & (2.62) \end{cases}$$

The current cancellation effect of two channels can reduce the input current ripple. As shown in Figure 2.7. For the conventional interleaved boost converter, the normalized current ripple, $\gamma(D)$, in terms of duty cycle is represented as,

$$\gamma(D) = \frac{|\Delta i_{in}|}{|\Delta i_L|} = \begin{cases} \frac{1-2D}{1-D}, 0 < D \leq 0.5 & (2.63) \\ \frac{2D-1}{D}, 0.5 < D < 1 & (2.64) \end{cases}$$

The normalized input current ripple of the conventional single-channel boost converter is 1 since the input current ripple is the same as the inductor current ripple. In comparison to a conventional interleaved boost converter, the proposed converter has smaller normalized current ripple (or higher effective ripple cancellation) in the entire range of duty cycle. The full cancellation of the input current ripple occurs at *D=0.5*.

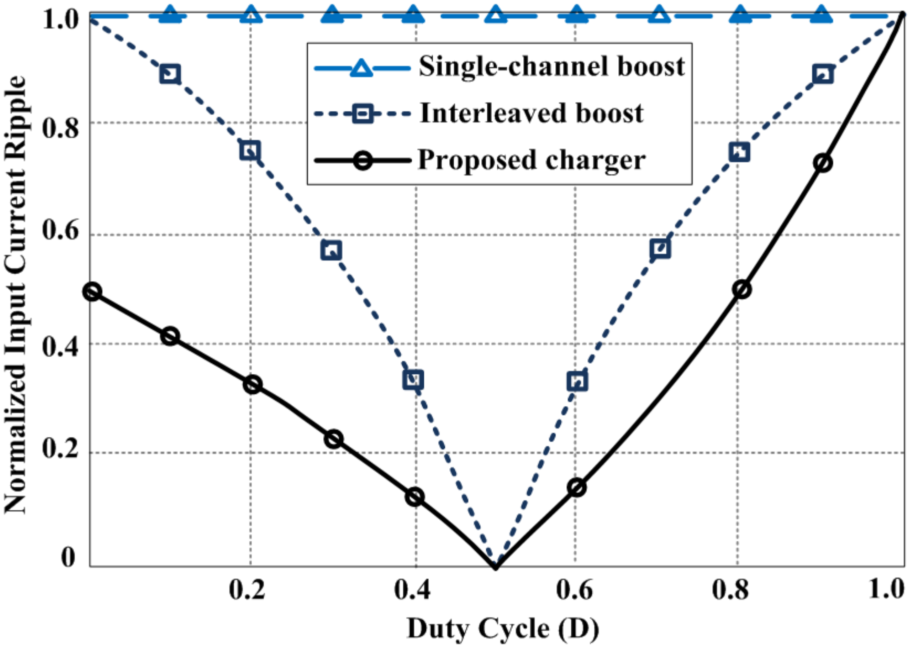

Figure 2.7. Effectiveness of the input current ripple cancellation for a boost converter, a conventional interleaved boost converter, and the proposed integrated propulsion machine charger.

### 2.2.3 Control Strategy

The control strategy of the integrated charger is developed to satisfy two requirements: the unity PF and less than 5% THD. The controller is composed of two closed loops: *(i)* the input current inner loop to shape the sinusoidal input line current; *(ii)* the output voltage/current outer loop to regulate the output voltage/current, as shown in Figure 2.8. The inner loop shapes the steady-state phase-B and phase-C currents ($I_b$ and $I_c$) through a phase locked loop (PLL) to follow the trajectory of the line voltage. The outer loop regulates the magnitude of the phase currents corresponding to output voltage/current. The PWM block is implemented by using DSP TMS320F28335 from Texas Instrument with the internal ePWM modules, which compares the signal from the PI controller with the produced triangle waveforms to generate two PWM signals. These two PWM signals are sent to switches S4 and S6 with 180-degree phase shift. The pulse widths of the PWM signals are determined by the duty cycles.

Due to the symmetry of the two-channel interleaved converter, the steady-state currents in phase-B and phase-C windings are split equally ($I_b=I_c=1/2|I_{in}|$), even though their instantaneous values might not be equal.

For a battery load, there are two charging modes: the constant current (CC) charging and constant voltage (CV) charging. The CC and CV charging are enabled by the controller of the proposed integrated charger. To achieve the CC mode charging, the reference battery charging current is sent to the outer loop controller, which regulates the output charging current. To achieve the CV mode charging, the reference battery voltage is sent to the outer loop controller, which regulates the battery voltage."

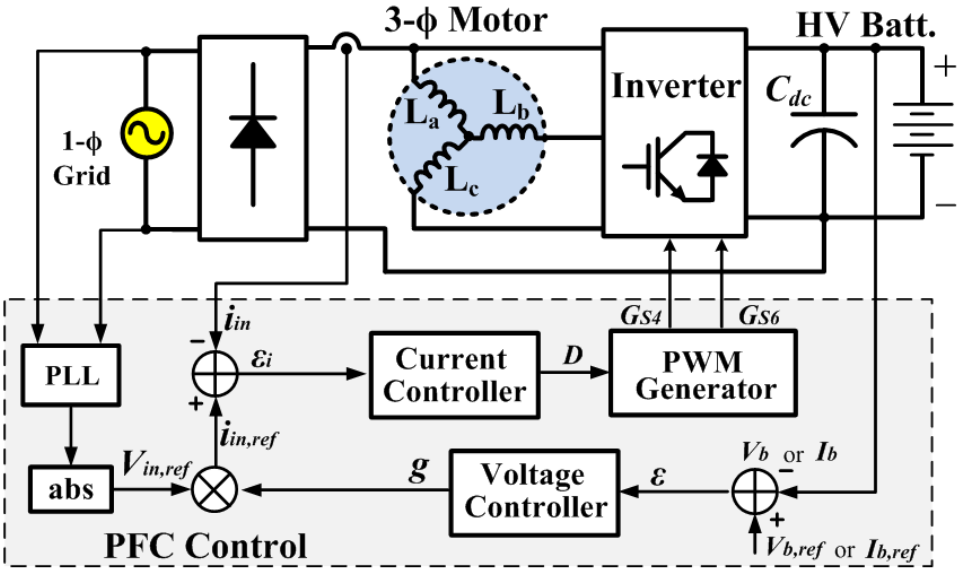

Figure 2.8. Schematic of the closed-loop control for the integrated charger.

### 2.2.4 Electromagnetic Effect of the Propulsion Machine

In battery charging mode, given the phase-B and phase-C currents flowing directions, the vector-sum of the stator magnetic flux due to phase-B and phase-C currents would be in the direction of the A-axis, according to the right-hand rule, which is aligned with phase-a magnetic flux. Therefore, the overall vector-sum of the three-phase stator magnetic flux is in the direction of the A-axis. As a result, the rotor is stationary with an electrical angle ($\theta_e$) equal to $\pi/2$ due to the electromagnetic force in the direction of a-axis. Figure 2.3 illustrates the rotor condition of a 3-phase, 2 pole-pairs ($P=2$) PMSM during charging, where the rotor angle ($\theta_r$) is equal to the angle between the d-axis and the q-axis ($\pi/2P$). The theoretical analysis is applicable for the machine with any number of pole-pairs. Here, a machine with 2 pole-pairs is utilized as shown in Figure 2.3.

Based on the Park transformation [16], the equivalent inductor currents in d-axis ($i_d$) and q-axis ($i_q$) can be expressed in terms of machine-winding currents ($i_a$, $i_b$, $i_c$) and electrical angle ($\theta_e$),

$$\begin{cases} i_d = \frac{2}{3}[i_a \sin\theta_e + i_b \sin(\theta_e - \frac{2\pi}{3}) + i_c \sin(\theta_e + \frac{2\pi}{3})] & (2.65) \\ i_q = \frac{2}{3}[i_a \cos\theta_e + i_b \cos(\theta_e - \frac{2\pi}{3}) + i_c \cos(\theta_e + \frac{2\pi}{3})] & (2.66) \end{cases}$$

The produced electromagnetic torque $T_e$ can be represented as,

$$T_e = \frac{3}{2}[\lambda_m i_a \cos\theta_e + \frac{1}{2}(L_q - L_d) i_a^2 \sin(2\theta_e)] \tag{2.67}$$

The initial electrical angle is set to be $\pi/2$ before the charging mode begins. During the charging mode, the current in phase B has the same phase angle as the current in phase C. The current in phase A is the sum of the currents in phase B and phase C machine windings. The electromagnetic torque, generated by the magnetic flux of the permanent magnets and the machine-winding currents, will force the rotor to be locked in alignment with A-axis.

## 2.3 Experimental Results

To verify the proposed theory, a 3-kW prototype based on a propulsion system is developed. The circuit board is shown in Figure 2.9. A 220-$V_{rms}$, 3-phase round-rotor PMSM is utilized as coupled inductors during charging. The propulsion system utilizes a three-phase inverter module with six IGBTs. The Chroma 63212 DC electronic load is utilized to test the circuit. The CC mode and CV mode of this electronic load can emulate the CC-CV charging process very well. Thus, the electronic load can be used to validate the feasibility of the proposed integration scheme.

Although the propulsion machine and the inverter are designed from the perspective of machine driving, the parameters are naturally applicable to battery charging. The self-inductance of each PMSM machine winding is 1.2mH, and the mutual-inductance between two machine windings is 0.5mH. These inductance values are typical values of the PMSM, widely applied in EVs. For an interleaved boost converter operating at the switching frequency of 15kHz, the inductance values allow the converter to operate in CCM operation.

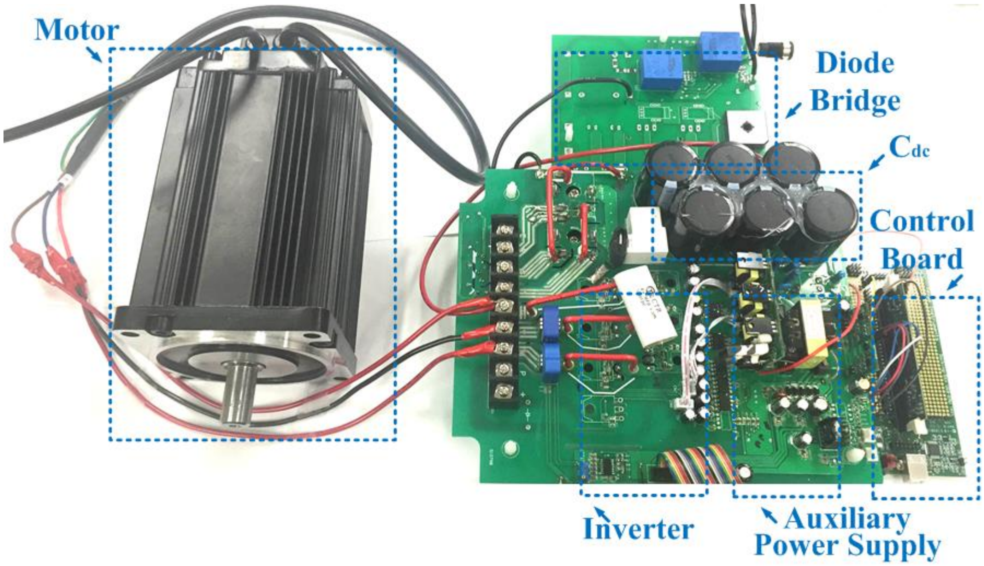

Figure 2.9. Proposed single-phase integrated onboard charger using PMSM.

As for the capacitor $C_{dc}$, the capacitance, 3.3mF, is selected based on the voltage ripple requirement for the propulsion mode. The proposed integrated charger utilizes the DC-link capacitor of the propulsion system without any add-on large capacitor. The DC-Link capacitor is designed based on the requirement of the voltage ripple in the propulsion mode. Generally, a large capacitance is selected for the DC-link capacitor. Thus, the capacitance of the DC-link capacitor can fully meet the requirement of 2nd harmonic oscillation during integrated charging mode. Therefore, it is not expected to influence the battery health and lifetime. This capacitance is large enough to balance the instantaneous power difference when energy is transferred from the DC side to the AC side within a voltage ripple limit on the DC-link capacitor. In battery charging mode, the energy is transferred in the opposite direction, and the voltage ripple can meet the same requirement as set in the propulsion mode. Thus, capacitor $C_{dc}$ can be directly used in the charging mode. The component parameters of the single-phase integrated charger are listed in Table 2.1.

Table 2.1

Component parameters of the single-phase integrated charger

| Device | Part # | Value | # of device |
|---|---|---:|---:|
| PMSM | AKM62M | 3.6kW/220V,rms/ 3-phase | 1 |
| Diode bridge rectifier | GBPC3506W | 35A/420V,rms | 1 |
| IGBT in inverter | FGL60N100 | NA | 6 |
| DC capacitor | LGW2W561 | 3.3mF | 6 |
| PFC controller | TMS320F28335 | NA | 1 |
| Current sensor | LTS25-NP | NA | 3 |
| Voltage sensor | LV20-P | NA | 2 |

The output voltage is regulated from 340 V to 420 V, based on the rated voltage of EV battery. The IGBT-based inverter is used to construct the interleaved boost charger with the switching frequency of 15kHz during charging. The switching frequency is selected based on the specifications of the IGBT in the inverter. The overall performance of the prototype is presented in Table 2.2.

Table 2.2
Performance of the single-phase integrated charger prototype

| Parameters | Symbol | Value | Unit |
|---|---:|---:|---:|
| Input ac voltage | $V_{in,rms}$ | 90~240 | V |
| Input ac current | $I_{in,rms}$ | 13.6 | A |
| Input frequency | $f_{ac}$ | 60 | Hz |
| Switching frequency | $f_s$ | 15 | kHz |
| Output dc voltage | $V_o$ | 340~420 | V |
| Equivalent resistive load | $R_L$ | 58.8 | Ω |
| Maximum output power | $P_o$ | 3 | kW |
| Power factor | $PF$ | 0.98 | |
| Input current total harmonic distortion | $THD$ | 3.96 | % |
| Maximum efficiency | $E_{ff}$ | 93.1 | % |

Figure 2.10 shows the waveforms of the input line voltage, phase-B current and phase-C current when the input current is 10A and the output power is 2kW. The rectified input current is evenly shared between the phase-B and the phase-C machine windings. Figure 2.11 shows waveforms of phase-B current, phase-C current and switch gating signals when the duty cycle is higher than 0.5. The waveforms validate the theoretical analyses of each switching state. The current ripples in phase-B and phase-C machine windings have frequency the same as the switching frequency. Due to the large inertia of the rotor, the high frequency ripples cause no vibrating around A-axis. Furthermore, the electromagnetic torque exerted on torque in one switching

period is zero because the current ripples in phase-B and phase-C windings are the same with 180 degree phase-shift. The experimental results have also proved that there is no rotor vibration around A-axis in battery charging mode. In Figure 2.10 and Figure 2.11, there is a small amount of unbalanced current between the phase-B and phase-C machine-winding currents. In the test, the unbalanced current amount is less than 0.8A, resulting in very limited uneven thermal dissipation between the two interleaved channels. This small unbalanced current does not affect the feasibility of the proposed integrated charger, and current balancing techniques can be applied to reduce the unbalancing currents [52], [53].

Figure 2.12 shows the waveforms of the input line current, input line voltage and output voltage at full load. The input voltage is $240V_{,rms}$. The output voltage is regulated at 420V. The efficiency reaches 93.1% at 3kW output power.

Figure 2.13 illustrates the efficiency curves for $120V_{rms}$ and $240V_{rms}$ input voltages at different loading conditions. The efficiencies are calculated by measuring the input current, the input voltage, output current and output voltage at different power levels for $V_{in}$=$120V_{,rms}$ and $V_{in}$=$240V_{,rms}$. The efficiency curves are obtained based on the calculated efficiencies. By measuring the RMS values of the input voltage, input current, output current, and output voltage for each component in the circuit, the power losses of each component can be measured.

Figure 2.14 shows the loss breakdown of the proposed integrated charger with input voltage $V_{in}$ = $240V_{,rms}$, output voltage $V_o$ = 420V and output power $P_o$ = 3kW.

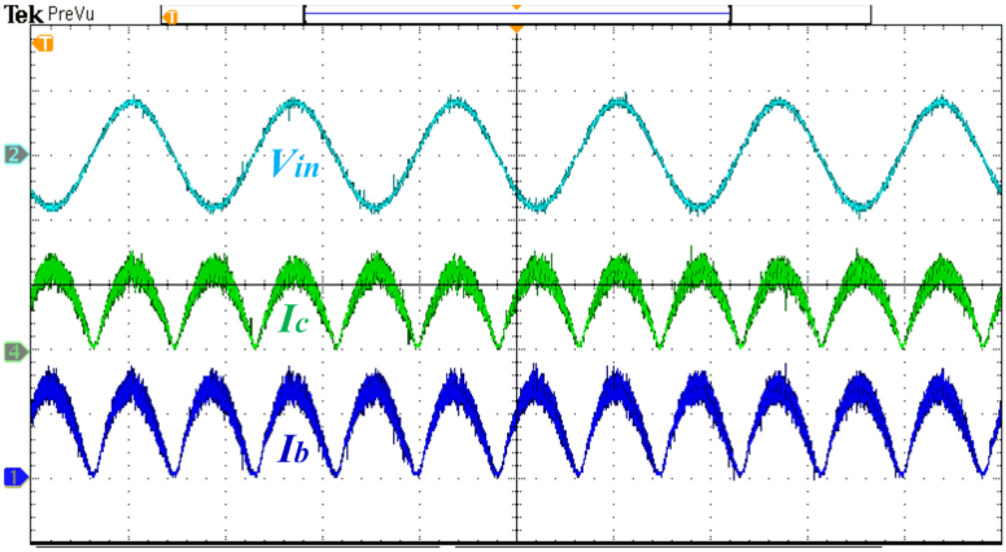

Figure 2.10. Experimental waveforms of input voltage ($V_{in}$), phase-B current ($I_b$) and phase-C current ($I_c$) of the proposed integrated charger. Y-axis (from top to bottom): Ch2 = $V_{in}$ 250 V/div; Ch4 = $I_c$ 5A/div; Ch1 = $I_b$ 5A/div; X-axis: time 10 ms/div.

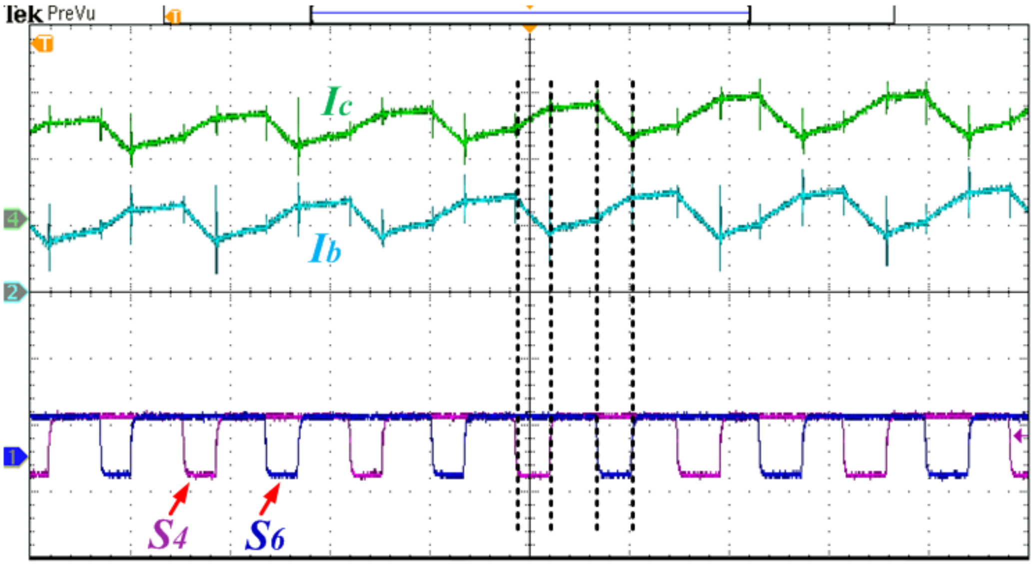

Figure 2.11. Experimental waveforms of phase-B current ($I_b$), phase-C current ($I_c$), gate voltage of S4 ($V_{S4,gate}$) and gate voltage of S6 ($V_{S6,gate}$) at $D$>0.5. Y-axis (from top to bottom): Ch4 = $I_c$ 2A/div; Ch2 = $I_b$ 2A/div; Ch3 = $V_{S4,gate}$ 25V/div; Ch1 = $V_{S6,gate}$ 25V/div, X-axis: time 40 µs/div.

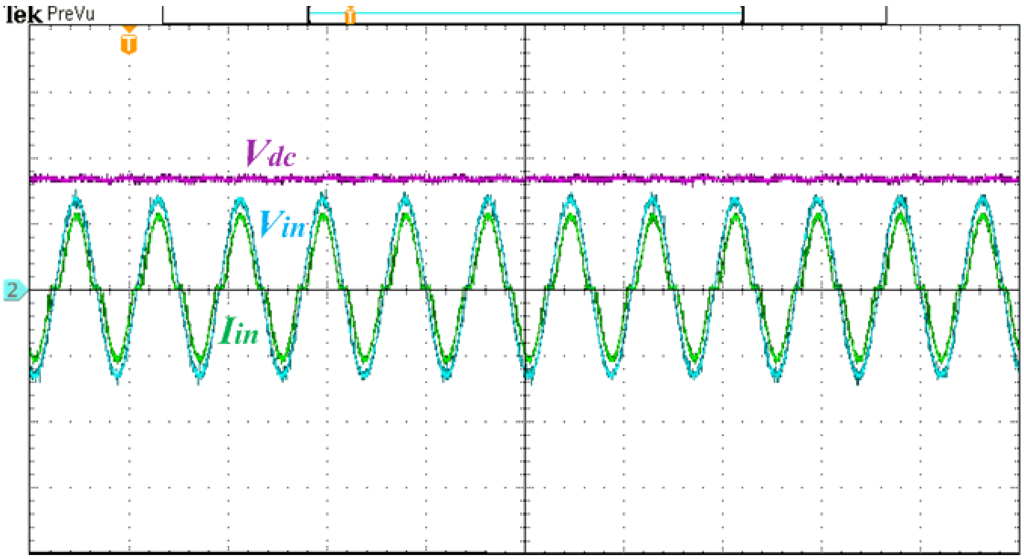

Figure 2.12. Experimental waveforms of the input current ($I_{in}$), input voltage ($V_{in}$), and output voltage ($V_{dc}$) at $V_{in,rms}$ = 240 V, $I_{in,rms}$ = 13.6 V, $V_{dc}$ = 420 V, $P_o$=3kW; Y-axis (from top to bottom): Ch3 = $V_{dc}$ 250 V/div; Ch2 = $V_{in}$ 250 V/div; Ch4 = $I_{in}$ 20 A/div; X-axis: time 20 ms/div.

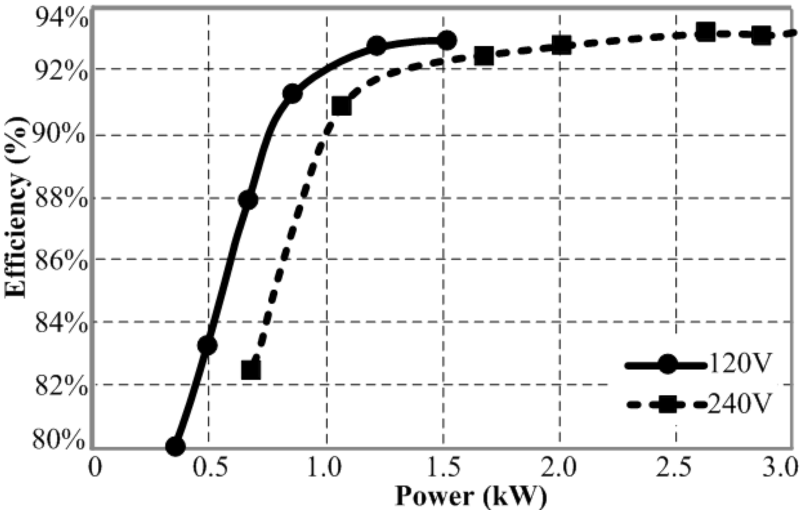

Figure 2.13. Conversion efficiency of the integrated charger prototype at different input voltage ($V_{in}$ = 120Vrms and $V_{in}$ = 240Vrms) and different output powers ($P_o$ = 600W ~ 3kW).

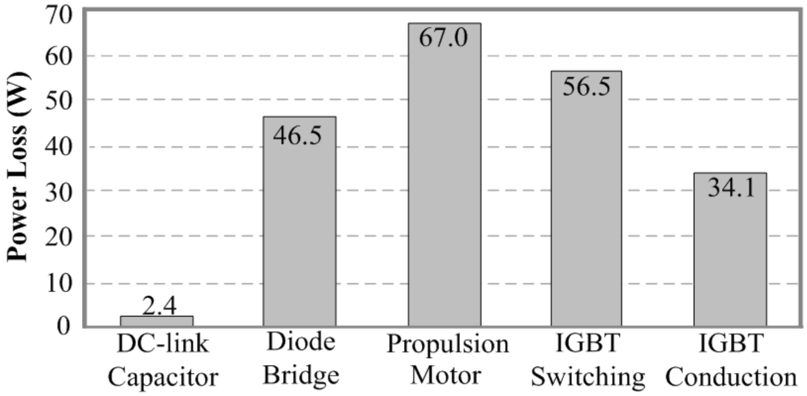

Figure 2.14. Loss breakdown at input voltage ($V_{in}$ = 240V,rms), output voltage ($V_o$ = 420V) and output power ($P_o$ = 3kW).

Figure 2.15 shows the waveforms during the transient process from 30% load to 70% load. The output voltage is kept as 400V during the transient process. The experimental results show that the control strategy perfectly regulates the output voltage during the load transient.

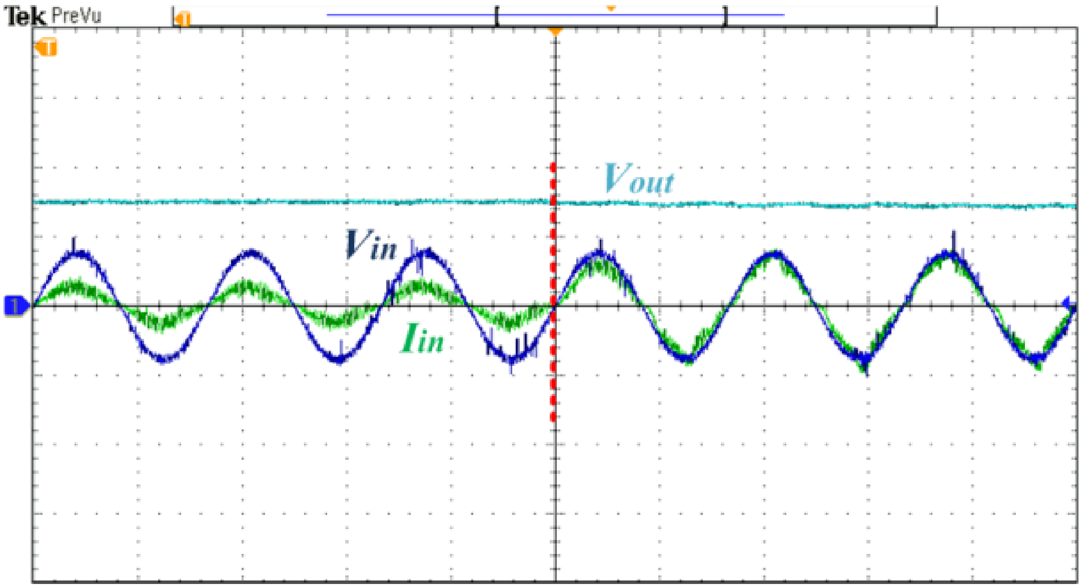

Figure 2.15. Experimental waveforms of the transient process (30% load to 70% load), including the input current ($I_{in}$), input voltage ($V_{in}$), and output voltage ($V_{dc}$) at $V_{in,rms}$ = 240 V, $I_{in,rms}$ = 4.3 V - $I_{in,rms}$ = 8.5 V, $V_{dc}$ = 400 V; Y-axis (from top to bottom): Ch2 = $V_{in}$ 500 V/div; Ch3 = $V_{dc}$ 250 V/div; Ch4 = $I_{in}$ 20 A/div; X-axis: time 10 ms/div.

Due to the power loss on the propulsion machine, the efficiency is slightly lower than the other single-phase battery chargers. Instead of utilizing the propulsion machine, the traditional single-phase chargers use optimally designed inductors, which cause less power loss. Table 2.3 shows the comparison between the proposed integrated charger with other conventional single-phase battery chargers, i.e. the two-stage battery charger with single-channel boost PFC converter and the two-stage battery charger with interleaved boost PFC converter. In terms of cost, the integrated charger costs much less than other battery chargers since only a diode-bridge is required for the proposed integrated charger.

Based on the analysis of the input current ripples and Figure 2.6, the proposed integrated charger has the minimum input current ripple in comparison to the other traditional battery chargers. Furthermore, the inductances of the propulsion machines are relatively higher than the inductances of the traditional battery chargers [34], resulting even less input current ripple. The comparison with the traditional battery chargers is presented in Table 2.3.

Table 2.3
Comparison to other single-phase battery chargers

| | Proposed Integrated Charger | Charger with single-channel boost PFC [3] | Charger with interleaved boost PFC [3] |
|---|---|---|---|
| Components | Diode Bridge | Two stage system (PFC+LLC) | Two stage system (PFC+LLC) |
| Size | Very Small | Large | Large |
| Efficiency | 93.1% | 94.5% | 95.0% |
| Cost | Very low | Medium | High |

Figure 2.16 compares the harmonics between the proposed integrated charger and the EN61000-3-2 Class D Limits (A) based on the experimental results at full load. It shows that the THD of the proposed integrated charger is compliant with the EN61000-3-2 standard. Figure 2.16 also shows the comparison between harmonics orders of the proposed integrated charger with those of the bridgeless boost PFC converter and the interleaved bridgeless boost PFC converter based on the data from literature [34].

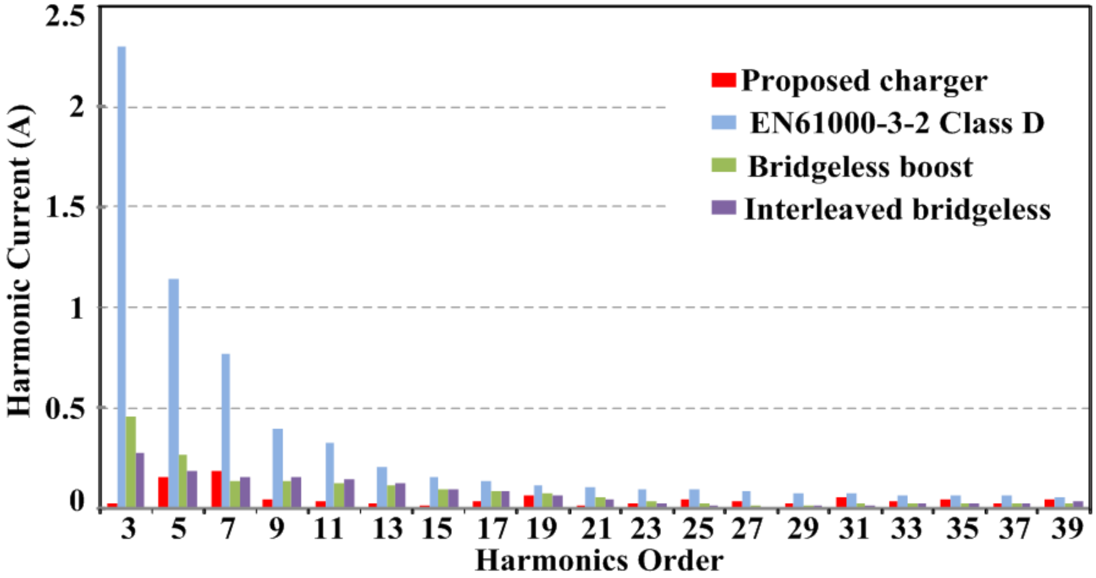

Figure 2.16. Harmonics orders at full load, compared against the EN61000-3-2 standard, the bridgeless boost PFC converter, and the interleaved bridgeless boost PFC converter.

As for the startup process of the converter, different startup strategies provide different transient behaviors. The reference value for the controller gradually increases at a slow rate during the startup process to limit the transient input current. Figure 2.17 shows the transient waveforms at the time of startup.

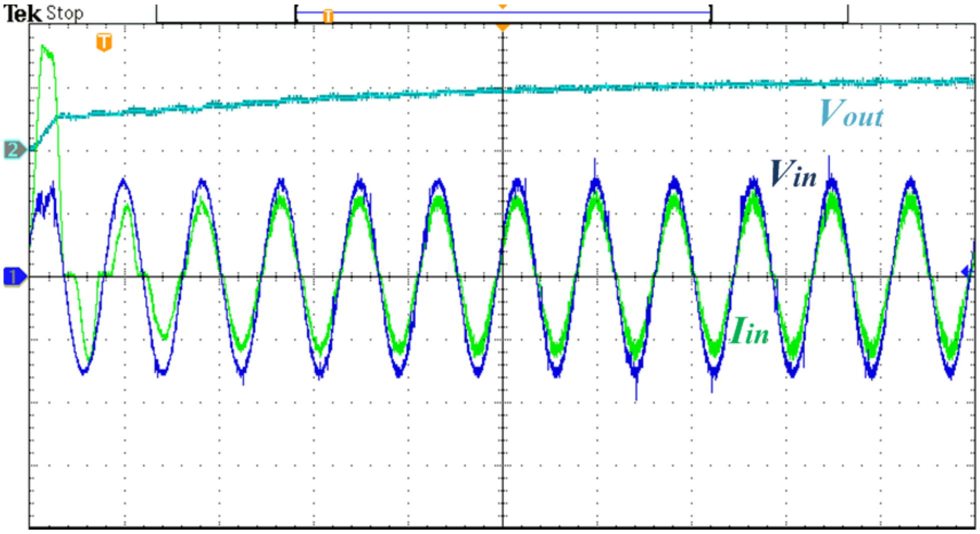

Figure 2.17. Experimental waveforms of the startup process, including the input current ($I_{in}$), input voltage ($V_{in}$), and output voltage ($V_{dc}$); Ch2 = $V_{in}$ 250 V/div; Ch3 = $V_{dc}$ 500 V/div; Ch4 = $I_{in}$ 20 A/div; X-axis: time 20 ms/div.

## 2.4 Summary

In this chapter, a single-phase integrated onboard charger using the propulsion system of an EV is proposed. With only one add-on passive diode bridge, the charging topology utilizes the propulsion machine and the inverter to form a two-channel interleaved boost converter, capable of PFC and battery current/voltage regulation. The steady-state analyses of PMSM model and the switching states are presented. Equivalent inductance and ripple cancellation effectiveness of the integrated charger is higher than conventional interleaved boost converters. Electromagnetic analyses indicate the stationary condition of rotor during steady-state charging. A 3kW prototype using a 3-phase round-rotor PMSM is built and tested to verify the proposed integrated scheme. A nearly unity PF and 3.96% THD of input current are acquired at full load with 93.1% efficiency.

# Chapter 3: Three-Phase Integrated Charger with Six-Switch Interface

The structures of the single-phase integrated charging system and the three-phase integrated charging system are shown in Figure 3.1.

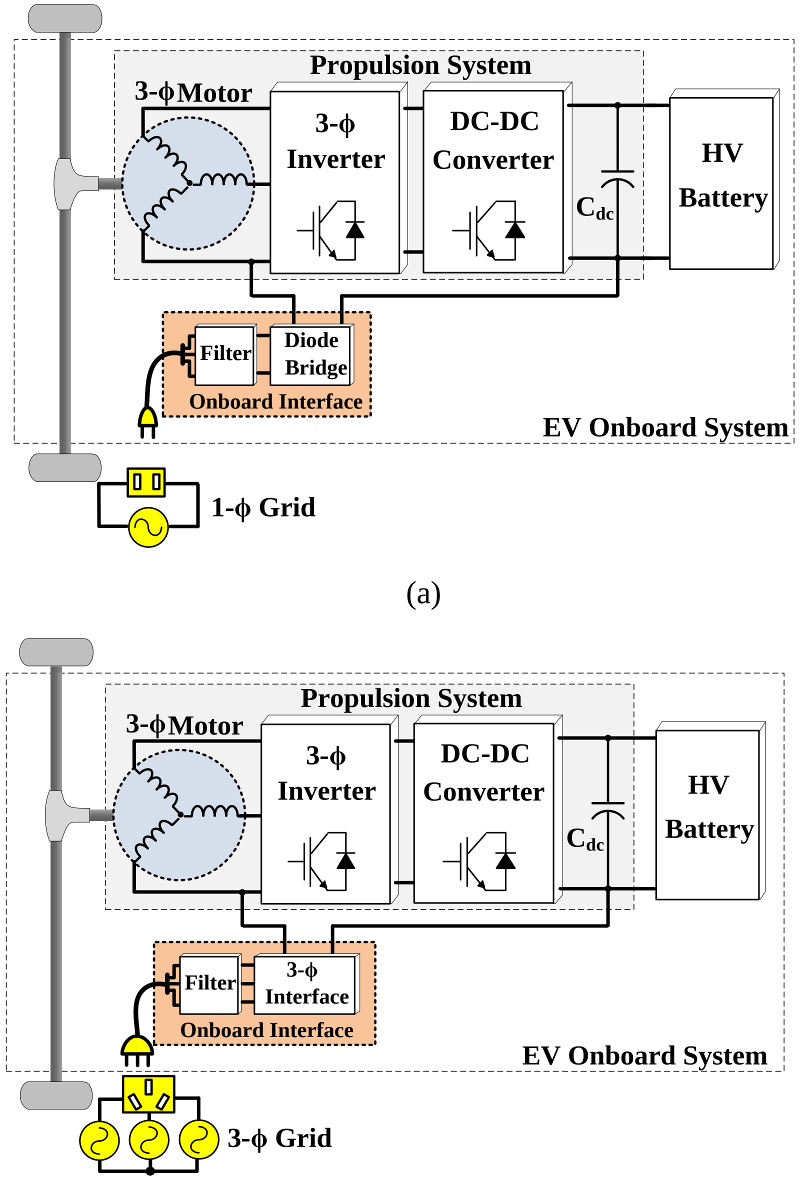

(a)

(b)

Figure 3.1. Schematics of the single-phase integrated charger (a) and the three-phase integrated charger (b).

In comparison to the single-phase integrated charger, three-phase integrated charger can achieve battery charging with much higher power level. The interface of the single-phase integrated charger is a diode bridge, while the interface for the three-phase integrated charger is a buck-type three-phase circuit, mainly composed of semiconductors.

## 3.2 Topology of Three-Phase Integrated Charger

The integrated charger in this chapter consists of a three-phase six-switch interface and the propulsion system of an EV. The Proposed three-phase six-switch interface is shown in Figure 3.2. There are six switches and six diodes in the interface. At the DC side, no diode is needed to connect between the p and n points.

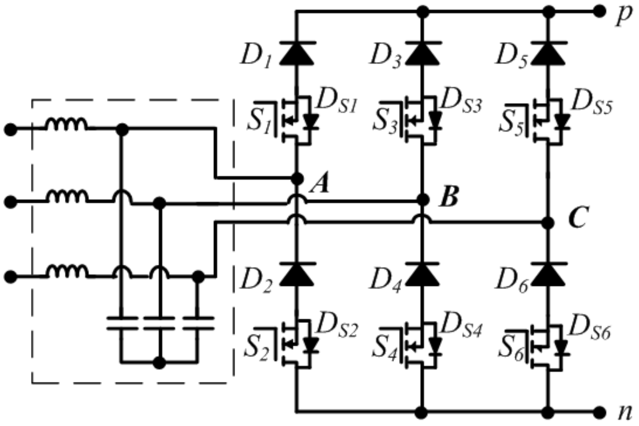

Figure 3.2. Proposed three-phase six-switch interface for three-phase integrated charger.

The proposed topology of the three-phase integrated onboard charger with six-switch interface is shown in Figure 3.3. The positive terminal of the interface is connected to one of the propulsion machine's phase-terminals (phase-A used in Figure 3.3), while the negative terminal of the interface is connected to the negative terminal of the inverter’s DC-link. The integration scheme is applicable to all traditional three-phase AC machine propulsion system, where access to machine phase terminals (A, B, C) is available. In addition, the converter is operated in continuous current mode (CCM).

According to the analysis in Chapter 2.1, in stationary condition ($\theta_e=\pi/2$), each phase serves as a discrete inductor with the equivalent inductances $L_{ph}$, which is expressed as, $L_{aa} + M_s$. Therefore, in stationary condition ($\theta_e=\pi/2$), the mutual effect appears between phase-B and phase-C; however, it has no influence on phase a. The equivalent inductance of the machine-windings is derived in Eq. (3.1).

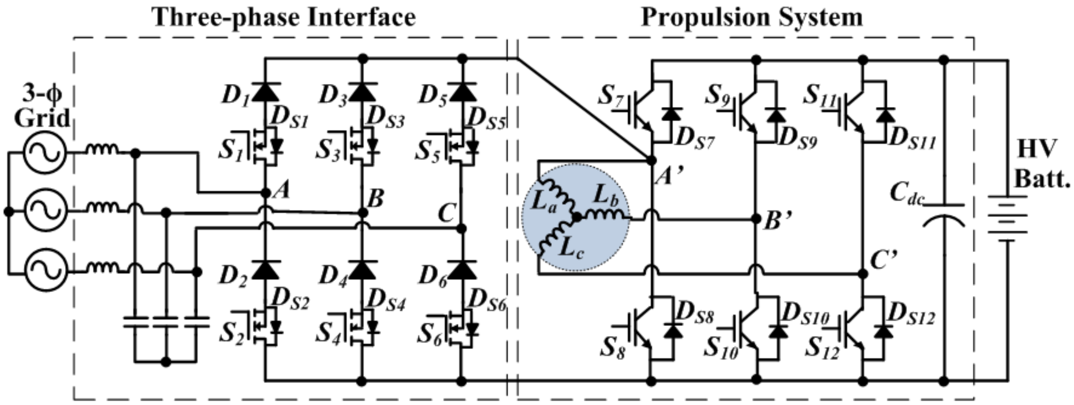

Figure 3.3. Proposed topology power electronics interfaces for a plug-in electric vehicle.

$$L_m = \frac{3}{2}(L_{aa} + M_s) \tag{3.1}$$

Therefore, the equivalent inductance of the machine can be derived base on the self-inductance and the mutual inductance. The total torque on the rotor can be analyzed according to Eq. (2.67). Given the flowing directions of the currents $i_b$ and $i_c$ during charging, the vector of the sum stator magnetic flux would be in the direction of A-axis. As a result, the rotor is stationary with an electrical angle ($\theta_e$) equal to $\pi/2$

because the electromagnetic force is in the direction of A-axis. The force generated by the magnetic flux of the permanent magnets and the stator phase currents enforce the electrical angle to be locked at *π/2*, where the rotor is aligned with a-axis. Therefore, there is no movement of the rotor during charging.

## 3.3 Operation Principles of Three-Phase Charging

In each gird period, there are 12 sectors with 30 degrees phase intervals. In each sector, two largest line-to-line mains voltages are selected to form the output voltage. The time intervals of the line-to-line voltages are calculated based on the modulation ratio and the input phase voltages. The division of 12 sectors in a grid period is shown in Figure 3.3 [58].

### 3.3.1 Modulation Scheme

The voltage steps in a switching period of sector I are shown in Figure 3.4.

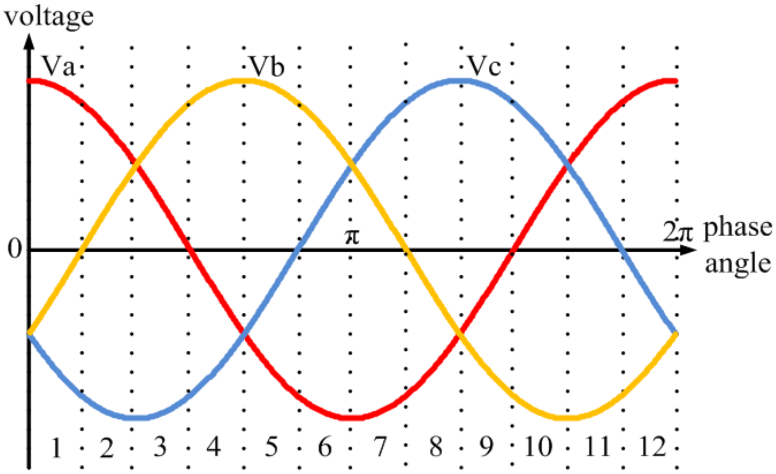

Figure 3.4. Division of 12 sectors in a gird period.

Switching-loss optimized modulation scheme is utilized to obtain the minimum and stair-shaped voltage steps during transition of operation modes, resulting in the minimum switching loss.

The same duty ratio is sent to both the switches in a bridge legs. The conduction of the upper switch or lower switch is determined by the input voltage. The duty ratios for bridge legs are calculated as,

$$\delta_i = M \frac{|v_i|}{V_{Npk}} \tag{3.2}$$

where, $M$ is the modulation ratio, ranging from 0 to 1; $v_i$ is the input phase voltage; $\delta_i$ is the corresponding phase duty ratio. Table 3.1 provides the selected line-to-line mains voltages and the effective duty ratios for each sector [58].

Table 3.1
Applied line-to-line voltages and its corresponding intervals for each sector

| Sector | Voltage (interval) | |
|---|---|---|
| 1,7 | $V_{AC}$ $(\delta c)$ | $V_{AB}$ $(\delta b)$ |
| 2,8 | $V_{AC}$ $(\delta a)$ | $V_{BC}$ $(\delta b)$ |
| 3,9 | $V_{BC}$ $(\delta b)$ | $V_{AC}$ $(\delta a)$ |
| 4,10 | $V_{BC}$ $(\delta c)$ | $V_{BA}$ $(\delta a)$ |
| 5,11 | $V_{BA}$ $(\delta a)$ | $V_{BC}$ $(\delta c)$ |
| 6,12 | $V_{BA}$ $(\delta b)$ | $V_{CA}$ $(\delta c)$ |

### 3.3.2 Operation Modes

For each sector, there are 6 operation modes. Due to the symmetry of the 12 sectors, the sector I from 0-30 degree is discussed here as an example. As it can be seen from Figure 3.4, the input mains phase voltages have relation as $V_a>0>V_b>V_c$ in the sector I. The line-to-line voltages $V_{AC}$ and $V_{AB}$ are utilized to form the output voltage. The switching actions for each bridge leg are shown in Figure 3.5. The corresponding six operation modes of the circuit are shown in Figure 3.6. All the switches have the same switching frequency due to the EMI consideration.

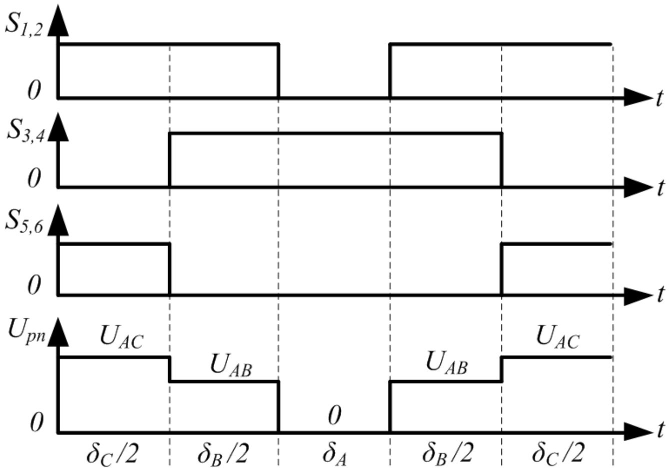

Figure 3.5. Switching actions and voltage steps during a switching period in Sector I.

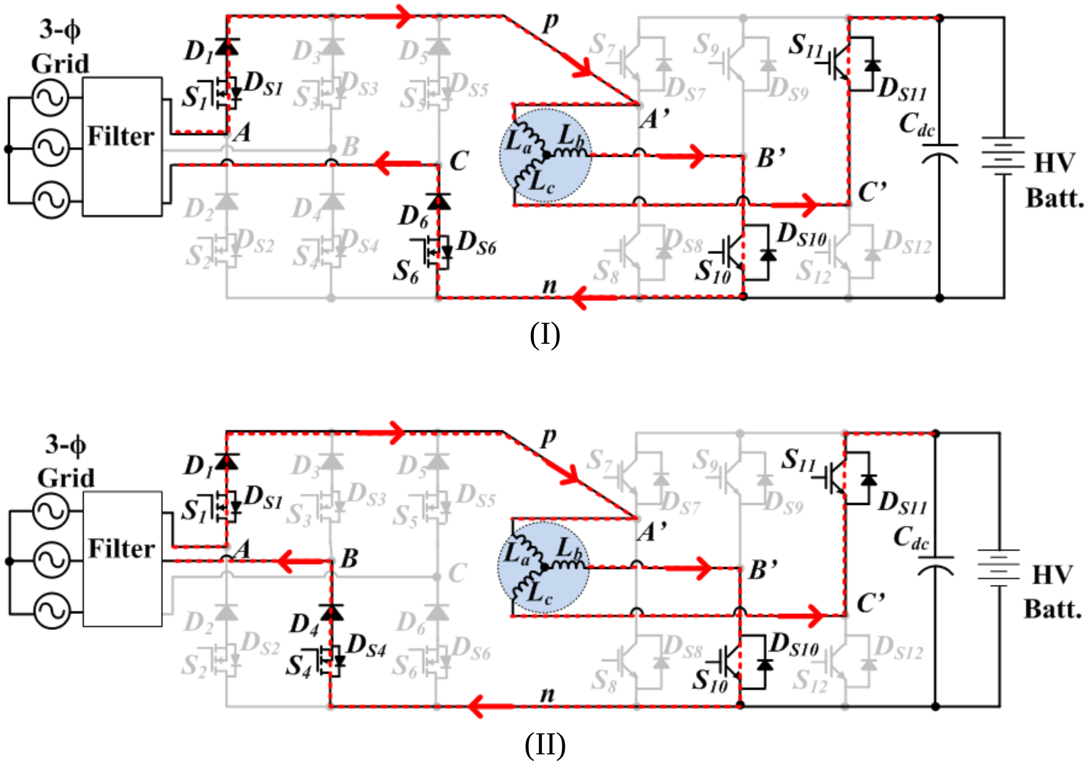

(I)

(II)

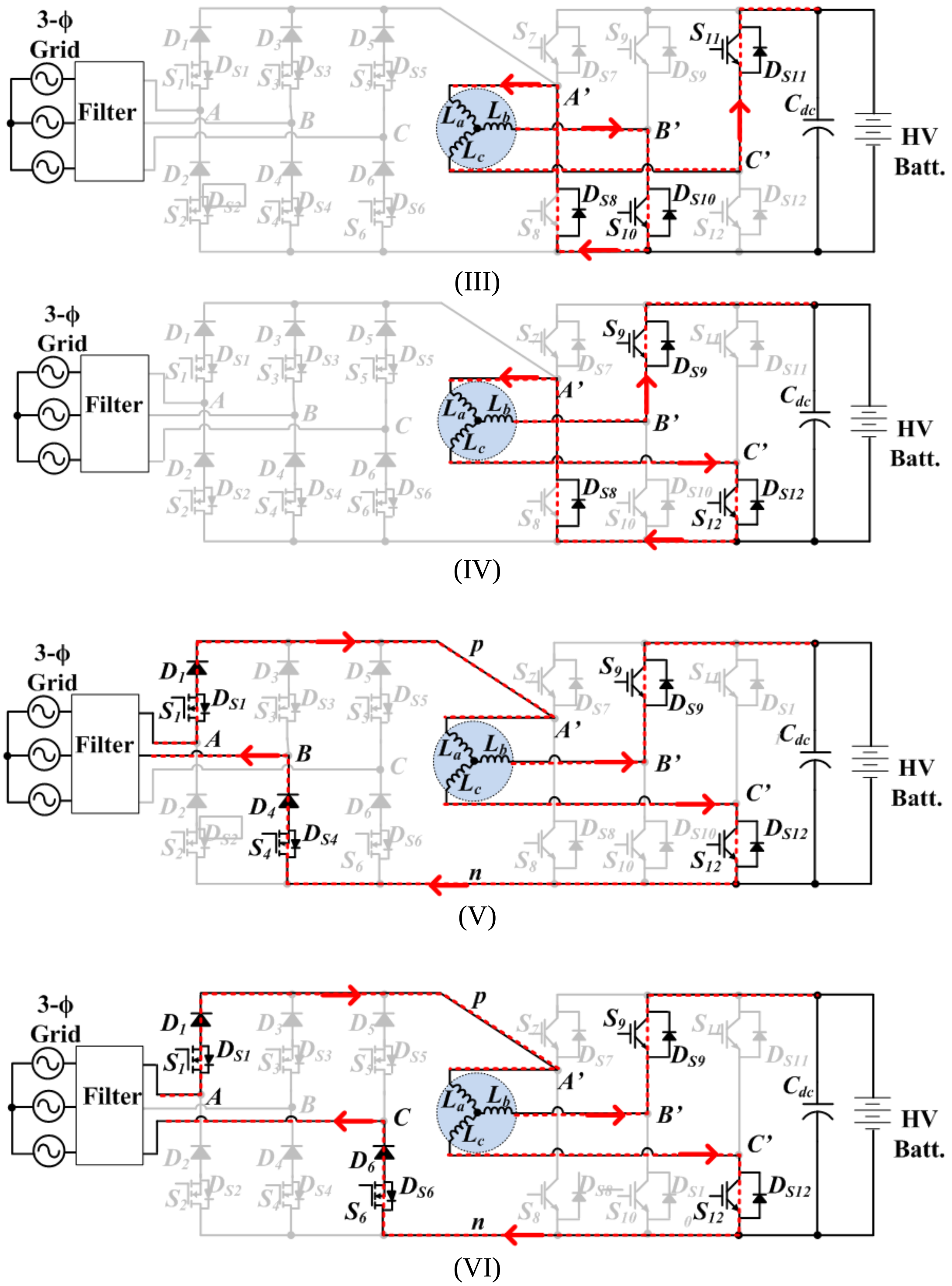

(III)

(IV)

(V)

(VI)

Figure 3.6. Operation modes of the proposed integrated charger.

In mode I, switches $S_1$ and $S_6$ are turned on. The voltage $V_{pn}$ is equal to the voltage $V_{AC}$. The switches $S_{10}$ and $S_{11}$ are turned on. The voltage over $L_a$ and $L_b$ is

$V_{AC}$, while the voltage over $L_a$ and $L_c$ is $V_o$- $V_{AC}$. Thus, the current variations of the inductor currents $i_{La}$ and the $i_{Lb}$ are expressed as,

$$\frac{di_{Lb}}{dt} = \frac{V_{AC}}{2L_{ph}} \tag{3.3}$$

$$\frac{di_{Lc}}{dt} = -\frac{V_o - V_{AC}}{2L_{ph}} \tag{3.4}$$

In mode II, switches S$_1$ and S$_4$ are turned on. The voltage $V_{pn}$ is equal to the voltage $V_{AB}$. The switches S$_{10}$ and switch S$_{11}$ are turned on. The voltage over the $L_a$ and $L_b$ is $V_{AB}$, while the voltage over $L_a$ and $L_c$ is $V_o$- $V_{AB}$. Thus, the current variations of the inductor currents $i_{La}$ and $i_{Lb}$ are expressed as,

$$\frac{di_{Lb}}{dt} = \frac{V_{AC}}{2L_{ph}} \tag{3.5}$$

$$\frac{di_{Lc}}{dt} = -\frac{V_o - V_{AB}}{2L_{ph}} \tag{3.6}$$

In mode III, all the switches in three-phase buck stage are turned off. The voltage $V_{pn}$ is equal to 0. The switches S$_{10}$ and S$_{11}$ are still on. The voltage over the $L_a$ and $L_b$ is 0, while the voltage over $L_a$ and $L_c$ is -$V_o$. $i_{Lb}$ circulates in a current loop though the inductors $L_b$ and $L_a$. The current $i_{La}$ flows thought the body diode D$_{S8}$. The current variations of the inductor currents $i_{La}$ and $i_{Lb}$ are expressed as,

$$\frac{di_{Lb}}{dt} = const. \tag{3.7}$$

$$\frac{di_{Lc}}{dt} = -\frac{V_o}{2L_{ph}} \tag{3.8}$$

In mode IV, all the switches in three-phase buck stage are turned off. The voltage $V_{pn}$ is equal to 0. The switches S$_9$ and S$_{12}$ are still on. The voltage over $L_a$ and $L_b$ is -

$V_o$, while the voltage over $L_a$ and $L_c$ is 0. $i_{Lc}$ circulates in a current loop though the inductors $L_c$ and $L_a$. The current $i_{La}$ flows thought the body diode $D_{S8}$. The current variations of the inductor currents $i_{La}$ and $i_{Lb}$ are expressed as,

$$\frac{di_{Lb}}{dt} = -\frac{V_o}{2L_{ph}} \tag{3.9}$$

$$\frac{di_{Lc}}{dt} = const. \tag{3.10}$$

In mode V, the switches $S_1$ and $S_4$ are turned on. The voltage $V_{pn}$ is equal to the voltage $V_{AB}$. The switches $S_9$ and $S_{12}$ are turned on. The voltage over $L_a$ and $L_b$ is $V_o - V_{AB}$, while the voltage over $L_a$ and $L_c$ is $V_{AB}$. Thus, the current variations of the inductor currents $i_{La}$ and $i_{Lb}$ can be expressed as,

$$\frac{di_{Lb}}{dt} = -\frac{V_o - V_{AB}}{2L_{ph}} \tag{3.11}$$

$$\frac{di_{Lc}}{dt} = \frac{V_{AB}}{2L_{ph}} \tag{3.12}$$

In mode VI, the switches $S_1$ and $S_6$ are turned on. The voltage $V_{pn}$ is equal to the voltage $V_{AC}$. The switches $S_9$ and $S_{12}$ are turned on. The voltage over $L_a$ and $L_b$ is $V_o$ - $V_{AC}$, while the voltage over $L_a$ and $L_c$ is Vac. Thus, the current variations of the inductor current $i_{La}$ and the inductor current $i_{Lb}$ are expressed as,

$$\frac{di_{Lb}}{dt} = -\frac{V_o - V_{AC}}{2L_{ph}} \tag{3.13}$$

$$\frac{di_{Lc}}{dt} = \frac{V_{AC}}{2L_{ph}} \tag{3.14}$$

### 3.3.3 Inductor Current Ripple

The inductor current $i_{La}$ is the sum of inductor current $i_{Lb}$ and $i_{Lc}$. The inductor current $i_{La}$ is directly applied to form the mains current. Thus, the ripple of the inductor current can directly affect the mains currents. Due to the symmetry of the sectors in terms of the voltage $V_{pn}$, the ripple of the inductor current $i_{La}$ can be calculated based on one sector. The sector I is applied to calculate the ripple of the inductor current $i_{La}$ based on the operation modes. It is expressed as,

$$\Delta i_{La} = \frac{MT}{2L_{ph}V_{Npk}}\left(-V_o V_a + 2{V_c}^2\right) + \frac{V_o|D_2 - 0.5|T}{2L_{ph}} \tag{3.15}$$

where, $T$ is the switching period; $D_2$ is the duty ratio of the interleaved boost stage.

The input phase voltages $V_a$ and $V_c$ are subject to,

$$V_a = V_{Npk}cos(\theta), 0 < \theta < \frac{1}{6}\pi \tag{3.16}$$

$$V_c = V_{Npk}cos\left(\theta - \frac{2}{3}\pi\right), 0 < \theta < \frac{1}{6}\pi \tag{3.17}$$

Based on Eq. (3.15), the inductor current ripple $\Delta i_{La}$ is a function of the duty ratio $D_2$. When $D_2$ is equal to 0.5, this ripple is the minimum with the other parameters as constants. The interleaved boost stage needs to be controlled to ensure the minimum inductor current ripple in order to minimize the size of the input filter and the EMI filter. Thus, the duty ratio of the interleaved boost stage is fixed at 0.5.

### 3.4 Modeling of Three-Phase Charging System

In order to analyze the stability of the system, the equivalent model is derived for the proposed integrated charger system.

### 3.4.1 Equivalent Circuit

In each sector, the three-phase interface shows similar dynamic performance as a buck-type DC-DC converter equipped with an input filter under a variable input voltage. The three-phase interface can be modeled as an equivalent buck converter. Although the waveforms of the two interleaved channels have 180 degree phase shift, the average current of the two interleaved channels are the same. Thus, the interleaved boost stage can be modeled as a conventional boost converter with an equivalent inductance $L_m$.

The entire integrated charger system has a similar dynamic behavior to a non-inverting buck-boost converter. The equivalent circuit of the system is shown in Figure 3.7. For simplicity, only a single stage input filter is considered without damping resistor.

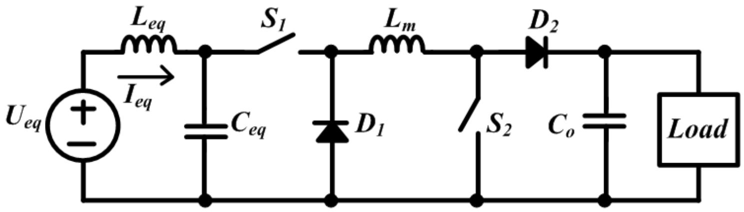

Figure 3.7. Equivalent circuit of the proposed integrated charger.

The buck-type rectifier is a current source converter. The modulation ratio of the three-phase interface is defined based on the input current and the inductor current,

$$M = \frac{I_{Npk}}{I_L} \tag{3.18}$$

where, $I_{Npk}$ is the peak value of the input current; and $I_L$ is the inductor current.

Considering input power is equal to the output power,

$$\frac{3}{2}U_{Npk}I_{Npk} = D_2{}'I_LU_o \tag{3.19}$$

where, $U_{Npk}$ is the peak value of the input voltage; $D_2{}'$ is equal to 1-$D_2$; $I_L$ is the inductor current; and $U_o$ is the output voltage. Thus, the modulation ratio can be derived as,

$$M = \frac{D_2{}'U_o}{\frac{3}{2}U_{Npk}} \tag{3.20}$$

where, $U_{Npk}$ is the peak value of the input voltage.

According to Eq. (3.18), the input mains current is directly formed by regulating the inductor current. Thus, the input current of the equivalent circuit is equal to the mains currents of the three-phase interface because the modulation of the equivalent buck switch $S_1$ in Figure 3.6 provides the same input current as the mains current.

$$i_{eq} = I_{Npk} \tag{3.21}$$

Assuming the components are ideal and there is no power loss, the equivalent circuit is constructed assuming equality of input and output power and energy conservation principle. Assuming that the input power of the equivalent circuit is the same as the input power of the three-phase buck interface, the equivalent voltage can be derived as,

$$u_{eq} = \frac{3}{2}U_{Npk} \tag{3.22}$$

For the input filter, the energy stored in the equivalent filter inductor and the equivalent filter capacitor should be the same as the energy stored in the three phase filter.

$$E_{f,C} = \frac{1}{2}C_{f,N}\left(u_A{}^2 + u_B{}^2 + u_C{}^2\right) = \frac{3}{4}C_{f,N}U_{Npk}{}^2 \quad (3.23)$$

$$E_{f,C} = \frac{1}{2}C_{eq}u_{eq}{}^2 \quad (3.24)$$

Combing Eq. (3.22) and Eq. (3.24), the equivalent capacitance can be derived as,

$$C_{eq} = \frac{2}{3}C_{f,N} \quad (3.25)$$

Similarly, by using the principle of energy conservation, the equivalent inductance can be derived as,

$$L_{eq} = \frac{3}{2}L_{f,N} \quad (3.26)$$

According to Eq. (3.25) and Eq. (3.26), the resonant frequency of the equivalent input filter would be same as the resonant frequency of the three phase input filter.

### 3.4.2 Small Signal Model

Based on the equivalent models, the small-signal equivalent model of the circuit can be obtained, as shown in Figure 3.8.

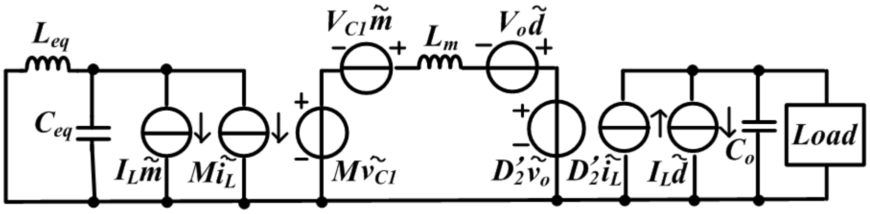

Figure 3.8. Small-signal model of the equivalent circuit.

According to the small signal model, the open-loop transfer function of inductor current to modulation ratio is derived as,

$$G_{mi} = \frac{\tilde{i}_L}{\tilde{m}} = \frac{U_{C1}}{sL} \cdot \frac{L_{eq}C_{eq}s^2 - \frac{L_{eq}MI_o}{U_{C1}D_2{}'}s + 1}{L_{eq}C_{eq}s^2 + \frac{L_{eq}}{L}M^2 + 1} \tag{3.27}$$

For the output voltage, the open-loop transfer function of the output voltage to modulation ratio is derived as,

$$G_{ui} = \frac{\widetilde{U_o}}{\tilde{m}} = \frac{U_{C1}D_2{}'}{sL} \cdot \frac{L_{eq}C_{eq}s^2 - \frac{L_{eq}MI_o}{U_{C1}D_2{}'}s + 1}{C_oL_{eq}C_{eq}s^3 + \frac{L_{eq}C_{eq}I_o}{U_o}s^2 + \left(\frac{C_oL_{eq}}{L}M^2 + C_o\right)s + \frac{L_{eq}I_oM^2}{U_oL} + \frac{I_o}{U_o}} \tag{3.28}$$

### 3.4.3 Control Strategy

The controller is composed of two closed loops: the input inner current loop to regulate the inductor current; and the output voltage outer loop to regulate the output voltage. The feed forward of the output voltage is introduced in the control loop to improve the dynamic performance during charging. The schematic of the control strategy is shown in Figure 3.9.

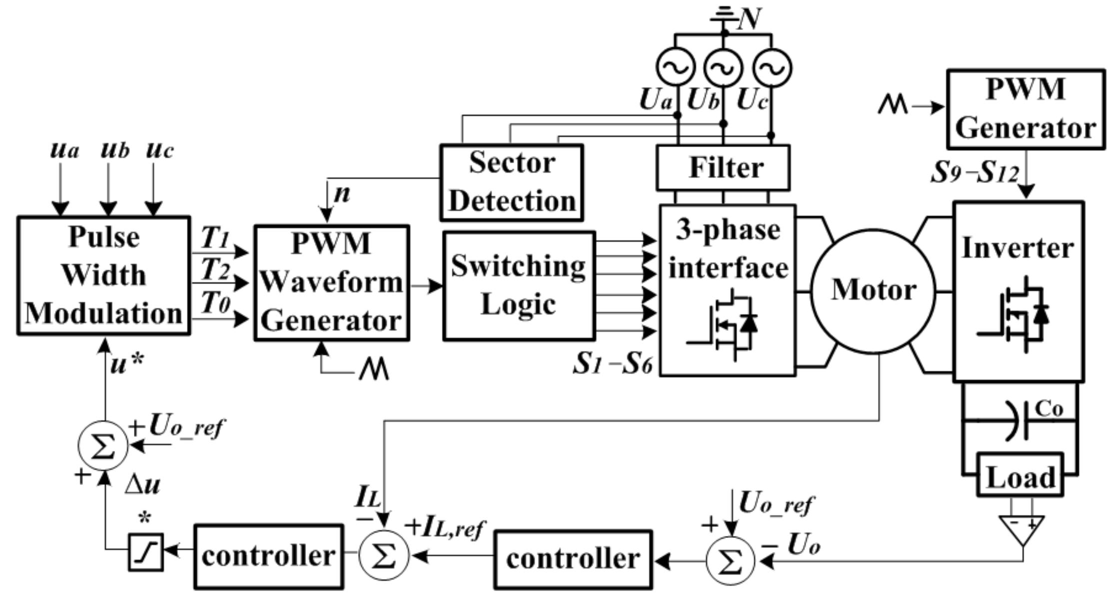

Figure 3.9. Control strategy of the proposed integrated charger.

For the inner current loop, the schematic of the current closed loop is shown in Figure 3.10.

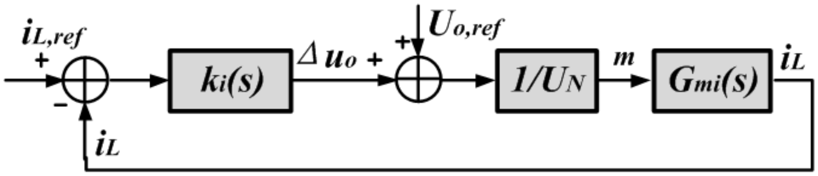

Figure 3.10. Schematic of the inner current close loop.

The PI controllers are applied in both the inner current loop and the output voltage loop. The transfer function of the PI compensator is expressed as,

$$G_c = k_p + \frac{k_i}{s} \tag{3.29}$$

where, $k_p$ and $k_i$ are the coefficients of the compensator. The closed loop bode plots of the inner current loop are shown in Figure 3.11.

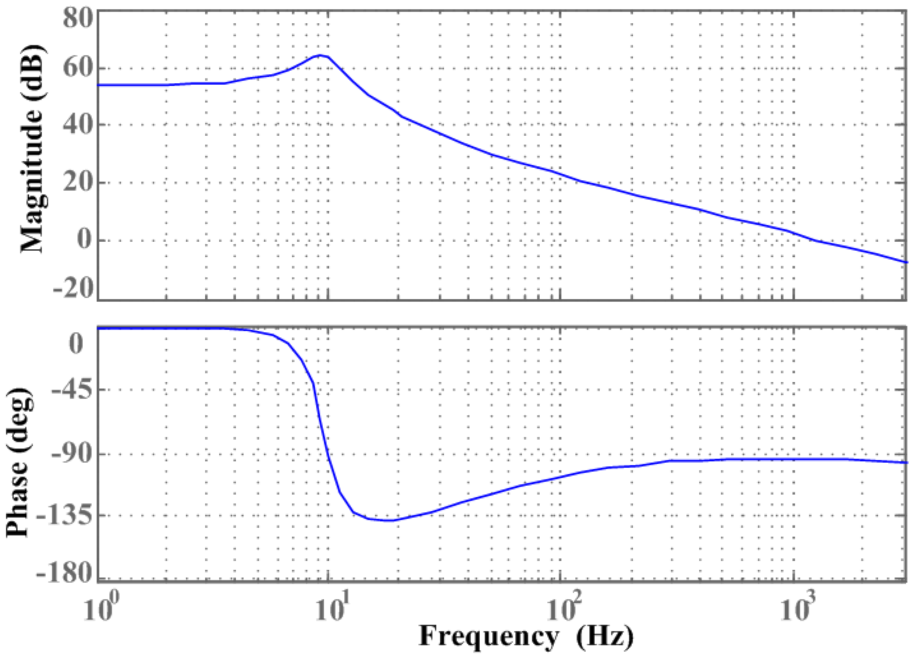

Figure 3.11. Bode plot of the inner current control.

The bandwidth is set at 1.3 kHz. The phase margin is larger than 50 degrees, which is sufficient for stability of the system. The $k_p$ is designed to be 0.05, while the $k_i$ is selected to be 10.

For the outer voltage loop, the bandwidth is much smaller than the bandwidth of the inner current loop. The inner current loop can be considered as a gain for designing the outer voltage loop. The bandwidth is set as 5Hz. For the PI voltage controller, the $k_p$ is selected as $2 \times 10^{-7}$ and $k_i$ as $1 \times 10^{-5}$. The phase margin is larger than 50 degree, which is enough to ensure system stability. The bode plots of the outer voltage loop are shown in Figure 3.12.

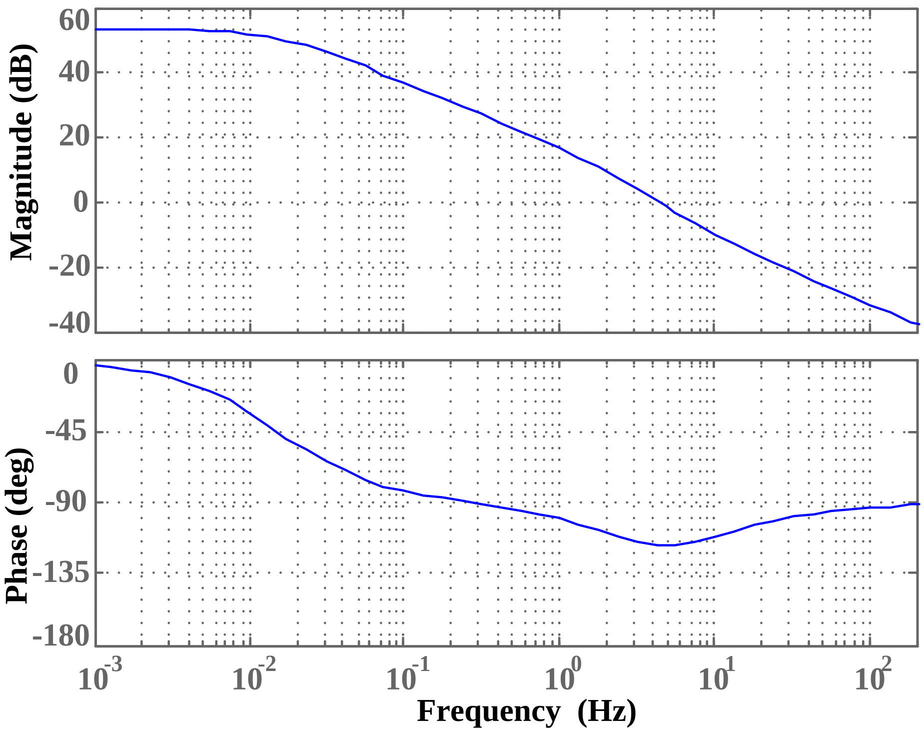

Figure 3.12. Bode plot of the outer voltage control.

### 3.4.4 Influence of the Machine Inductance

The equivalent machine inductance $L_m$ of the commonly used machine in EVs ranges from 1mH to 200mH [20]. In order to analyze the influence of the $L_m$ on the system, the bode plots of the inner current loop and the outer voltage loop are given with different $L_m$ values, as shown in Figure 3.13 and Figure 3.14.

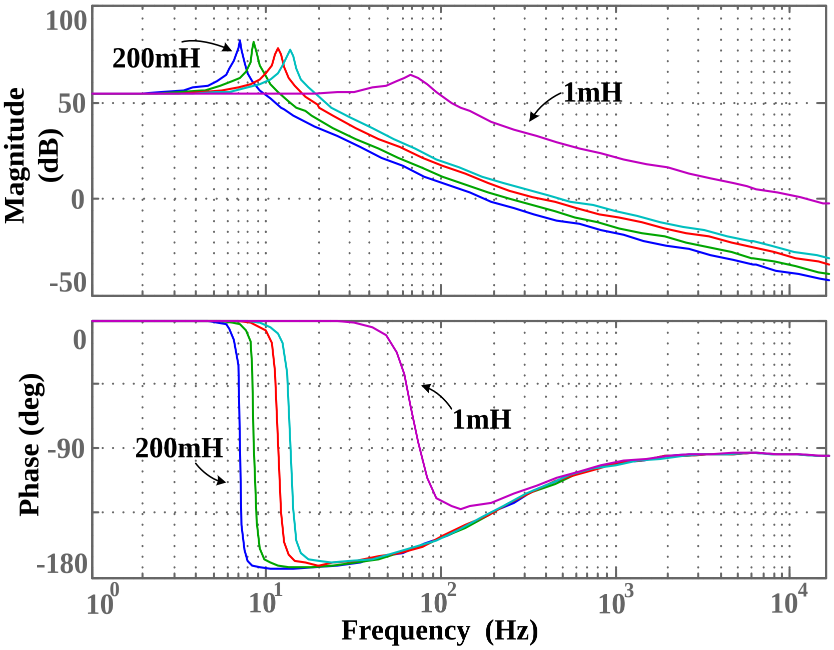

Figure 3.13. Bode plot of the inner current loop with different $L_m$ values.

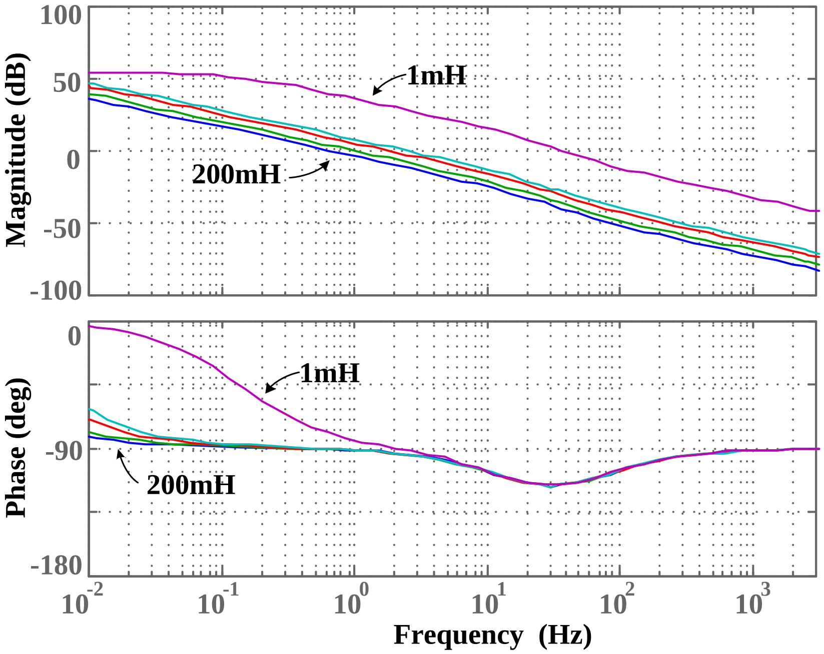

Figure 3.14. Bode plot of the outer voltage loop with different $L_m$ values.

Figure 3.13 and Figure 3.14 show that the bandwidths of the control loops decrease with increasing the machine inductance. In order to further analyze the influence of $L_m$ on the system, the root locus of the control-to-inductor-current transfer function and the control-to-output-voltage transfer function are plotted with $L_m$ varying from 1mH to 22mH. Figure 3.15 shows the variation of dominant pole of the transfer functions under $L_m$ variation for the inner current loop.

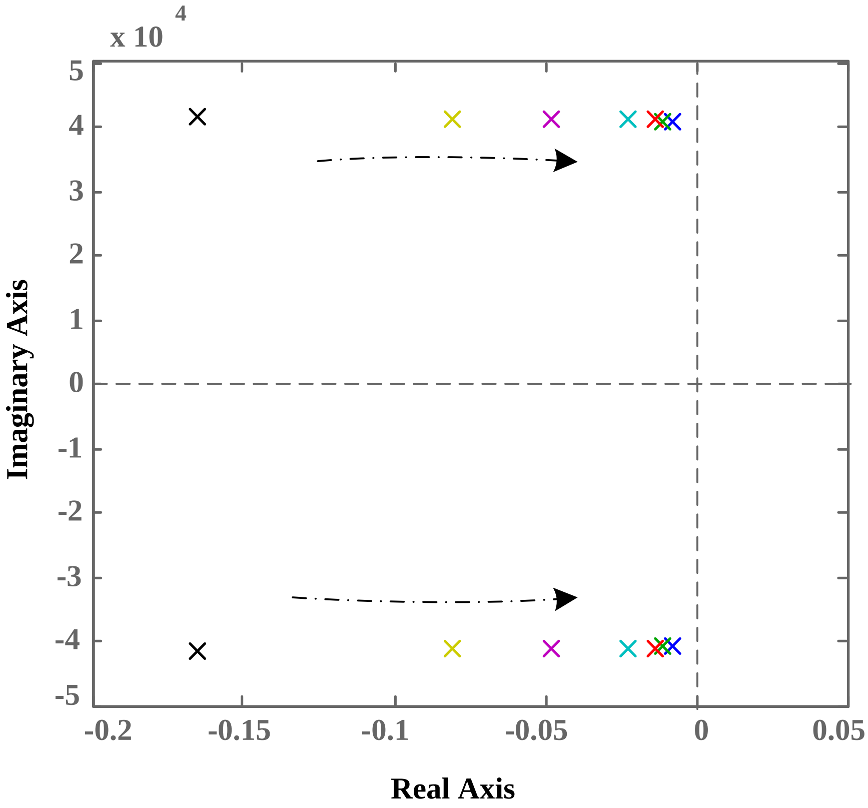

Figure 3.15. Root locus of the inner current loop with different $L_m$ values.

Figure 3.16 shows the variation of dominant pole of the transfer functions under $L_m$ variation for the outer voltage loop.

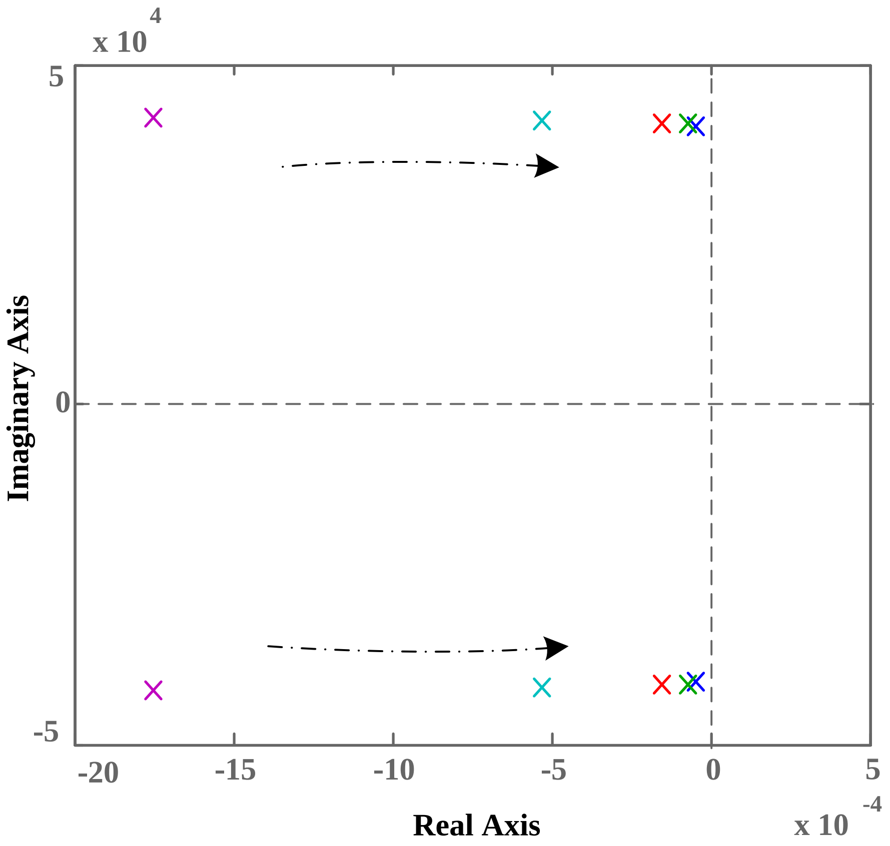

Figure 3.16. Root locus of the outer voltage loop with different $L_m$ values.

According to Figure 3.16, the dominant poles move towards the imaginary axis when $L_m$ increases. The shift of poles increases the system setting time and response time, which is consistent with the results of bode plot. The dominant poles are always on the left hand plane, ensuring the system stability.

The machine inductance does not affect the stability of the system. Bandwidths of control loops are slightly influenced when different propulsion systems are connected. The proposed topology is applicable to majority of machine drive systems with different propulsion machines.

### 3.5 Experimental Results

To verify the proposed theory, a 3.3-kW add-on interface was designed and developed, which was utilized as the test bed in conjunction with a 3.6-kW propulsion system, as shown in Figure 3.17. The 3-phase round-rotor PMSM is utilized as a three-winding coupled inductor in charging mode. Each phase winding has 1.2-mH self-inductance and 0.5-mH mutual-inductance between each two phase windings. The propulsion system utilizes a 3.6-kW three-phase inverter module with six IGBTs.

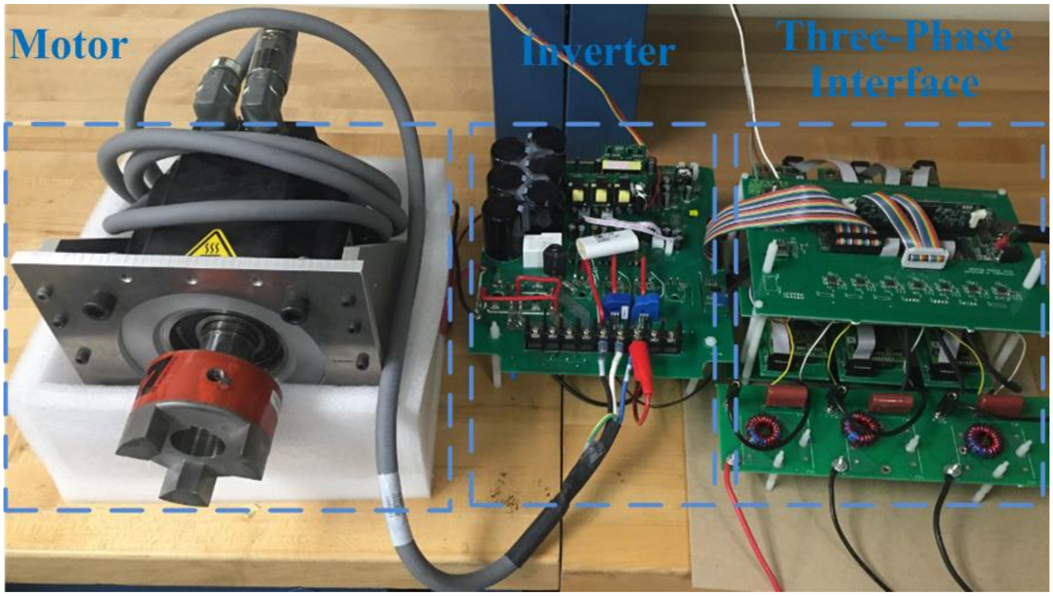

Figure 3.17. Test bed for the proposed three-phase integrated onboard charger.

A 60-Hz AC power source is utilized to emulate the single-phase grid interface. An electronic load is used to emulate the battery in experimental test. The output voltage is regulated from 280 V to 420 V, based on the rated voltage of EV battery packs. The switching frequency of the inverter and the three-phase interface are both set at 20 kHz. The overall performance of the test bed is presented in Table 3.2.

Table 3.2

Performance of the three-phase integrated charger

| Parameters | Symbol | Value | Unit |
|---|---:|---:|---:|
| Input ac voltage | $v_{ac,rms}$ | 120 | V |
| Input frequency | $f_{ac}$ | 60 | Hz |
| Switching frequency | $f_s$ | 20 | kHz |
| Output dc voltage | $V_o$ | 280~420 | V |
| Maximum output power | $P_o$ | 3.3 | kW |
| Power factor | $PF$ | 0.99 | |
| Total harmonic distortion | $THD$ | 4.77 | % |
| Maximum efficiency | $E_{ff}$ | 92.6 | % |

Figure 3.18 shows the waveforms of the input phase current ($i_a$), input phase voltages ($V_a$ and $V_b$) and output voltage at $V_o$=291$V$. The input voltage is 120$V_{,rms}$. Figure 3.19 shows the waveforms of the input phase current ($i_a$), input phase voltages ($V_a$ and $V_b$) and output voltage at $V_o$=400$V$. The input voltage is 120$V_{,rms}$. The efficiency curve at different loading conditions is illustrated in Figure 3.20. The maximum efficiency is 92.6%.

The gating signals have voltages levels of +15V during the on-state and -10V during the off-state.

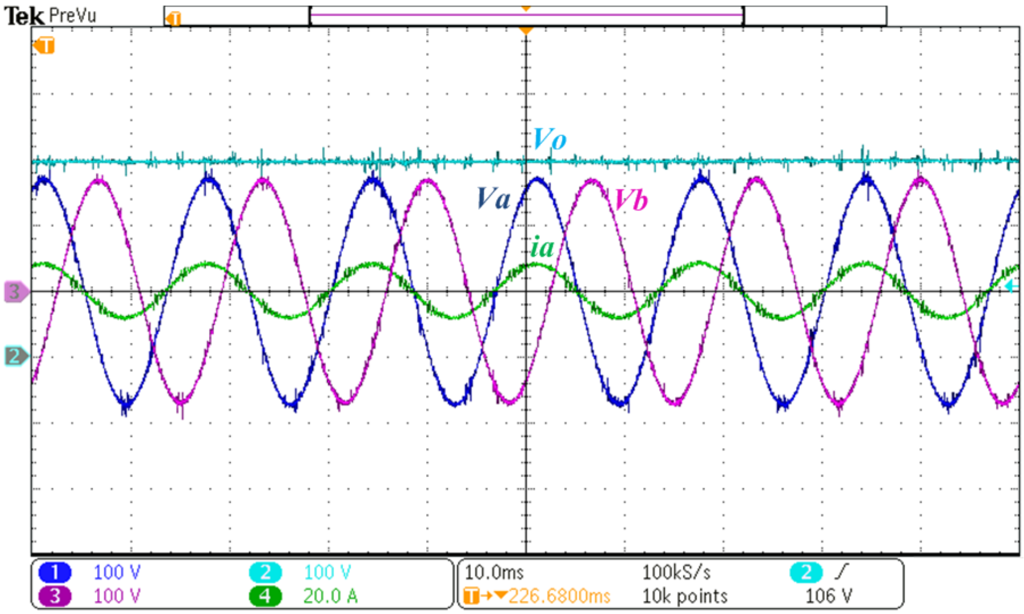

Figure 3.18. Experimental waveforms at $V_{in}$=120V,rms, $V_o$=291V, including input phase-A current ($i_a$), input phase-A voltage ($V_a$), input phase-B voltage ($V_c$), and output voltage ($V_o$).

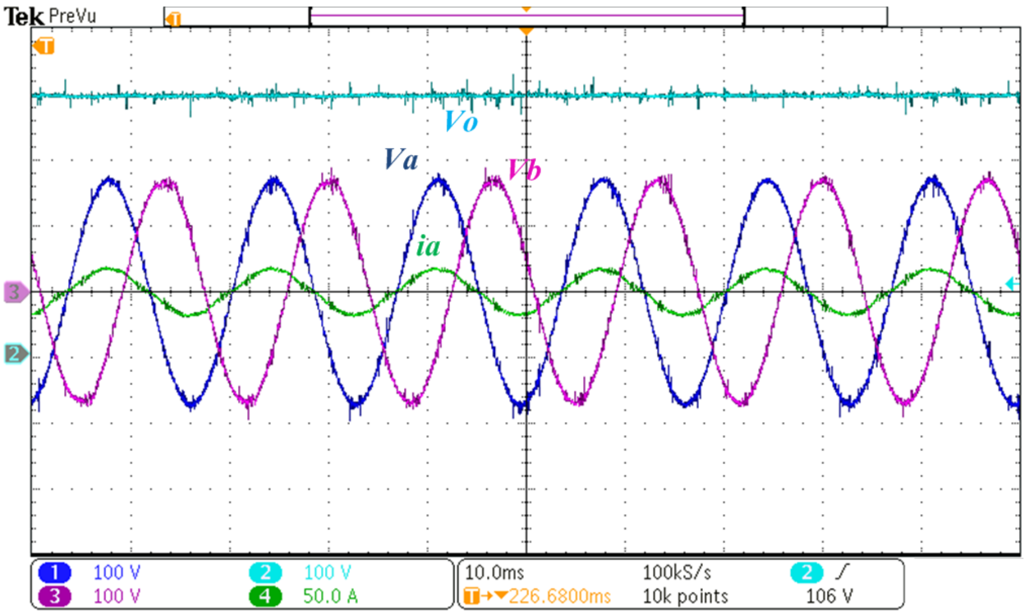

Figure 3.19. Experimental waveforms at $V_{in}$=120V,rms, $V_o$=400V, including input phase-A current ($i_a$), input phase-A voltage ($V_a$), input phase-B voltage ($V_c$), and output voltage ($V_o$).

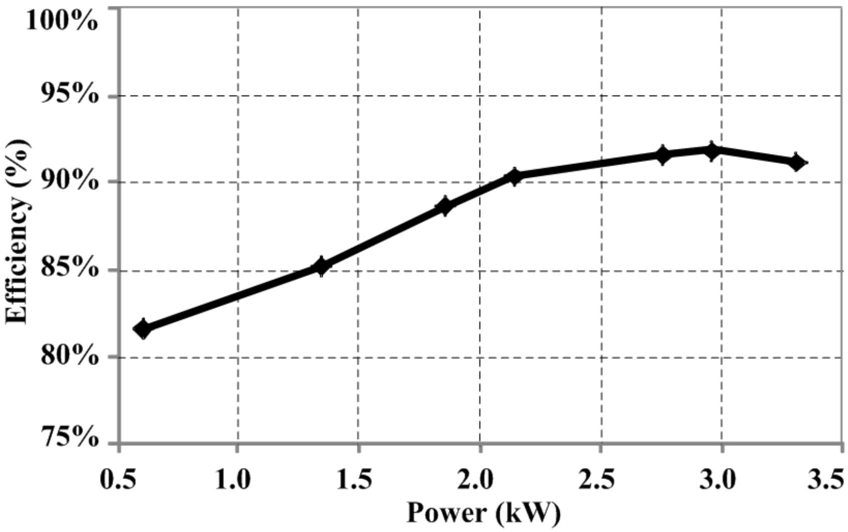

Figure 3.20. Efficiency curve of the proposed three-phase integrated onboard charger.

## 3.6 Summary

In this chapter, a three-phase integrated onboard battery charger using the propulsion system of an EV is proposed and designed. By connecting a three-phase six-switch interface to the propulsion system, the charging topology utilizes an AC propulsion machine and its inverter as a two-channel interleaved boost converter for PFC. The charger switching states are presented for steady-state analyses. The influence of machine inductance on the stability of the system is analyzed by using the bode plot and root locus plots. The proposed integrated architecture is verified through a 3.3-kW proof-of-concept test bed and a 3-phase round-rotor PMSM. A nearly unity PF and 4.77% THD is acquired at 3.3 kW charging with 92.6% efficiency.

# Chapter 4: Three-Phase Integrated Charger with Three-Switch Interface

To further reduce the size and weight of the three-phase integrated charger, an integrated three-phase onboard charger with a three-switch interface is proposed. The proposed integrated charger consists of a three-phase three-switch interface and the propulsion system of an EV. The proposed three-switch interface is developed based on the traditional three-phase three-switch AC-DC buck converter [59].

The three-phase interface is only composed of power semiconductors without bulky DC-link inductor and capacitor (except the small size input filter), significantly reducing the size and weight of the three-phase interface. The small size of the three-phase interface facilitates its onboard installment on EVs. At the DC side of the interface, no diode is needed to connect between the two terminals. Moreover, there are only three switches in the three-phase interface, which simplify the size of gate drive circuit and cooling requirements, further reducing the system size. The proposed three-phase interface is shown in Figure 4.1.

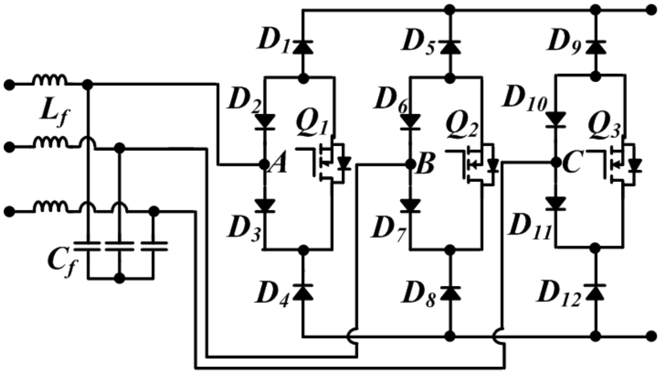

Figure 4.1. Proposed three-phase three-switch interface for three-phase integrated charger.

As for the control strategy, either the input current or the DC-link current can be regulated in a three-phase buck-type rectifier [60]. However, the DC-link current control slows down the system and deteriorates the dynamic performance of the input current, while the input current control ignores the current ripple of the DC-link inductor, resulting in higher input current ripple and lower THD. Compared with traditional three-phase buck-type converters, the proposed two-stage buck-boost integrated charger has two control variables, the duty cycle of the inverter and the modulation index of the three-phase interface.

Thus, a cascaded control strategy is designed and implemented. The first cascaded control regulates the machine-winding currents and the output voltage of the drive system stage, while the second cascaded control modulates the input filter inductor current and the input filter capacitor voltage of the three-phase interface. Thus, the input current, machine-winding currents and the battery voltage can be regulated simultaneously, reducing the machine-winding current ripple and improving the input current dynamics at the same time.

## 4.1 Basic Operational Principle

Figure 4.2 shows the topology of the charger with the three-phase interface stage and the drive system stage. The voltage between the p and n points is the intermediate voltage, $V_{pn}$.

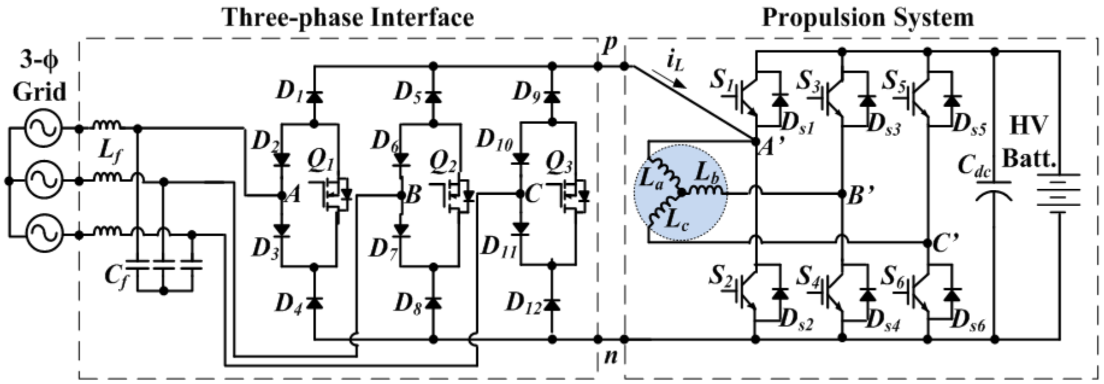

Figure 4.2. Proposed topology of the three-phase integrated charger with three-switch interface.

For the three-phase interface, the modulation index is defined as,

$$M = \frac{I_{Npk}}{I_L} \tag{4.1}$$

where, $I_{Npk}$ is the peak value of the input phase current, and $I_L$ is the output current of the three-phase interface.

In steady state, the duty cycle of the interleaved boost stage, *D*, and the modulation index of the three-phase rectifier stage, *M*, are subject to the Eq. (4.2),

$$\frac{M}{1-D} = \frac{V_o}{V_{Npk}} \tag{4.2}$$

where, $V_{Npk}$ is the peak voltage of the input phase voltage, and $V_o$ is the battery voltage. The phase modulation index can be calculated as,

$$\delta_i = M\frac{v_i}{V_{Npk}} \tag{4.3}$$

where, $v_i$ is the input phase voltage; $\delta_i$ is the phase modulation index. (*i* indicates phase A, phase B or phase C.)

For the three-phase interface, one grid period is divided into 12 sectors with each sector having 30 degrees [47]. As shown in Figure 4.3, the three-phase voltage vector is indicated as an arrow, which rotating in anti-clockwise direction.

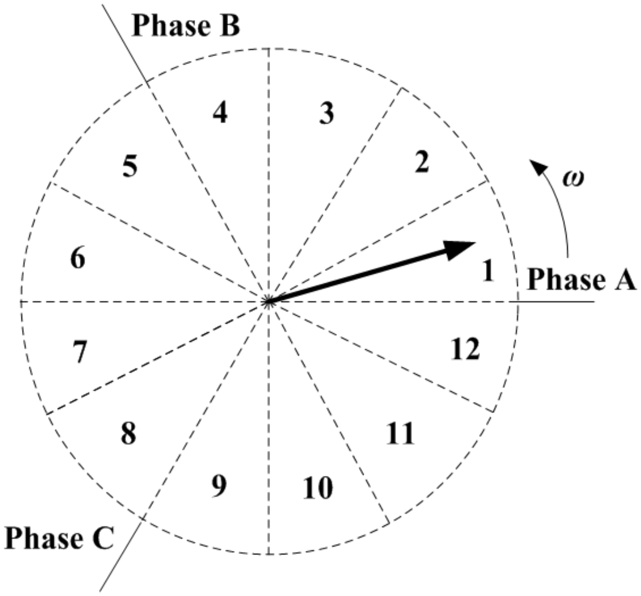

Figure 4.3. Division of 12 sectors during a gird period.

In each sector, two highest line-to-line voltages are selected to form the intermediate voltage, $V_{pn}$. Table 3.1 shows the line-to-line voltages and corresponding intervals for each sector [61]. For example, in Sector 1, the line-to-line voltages $V_{AC}$ and $V_{AB}$ are selected. The switching sequences of the switches Q1 - Q3 are shown in Figure 4.4. The symmetric switching sequence is selected to minimize the switching loss [59].

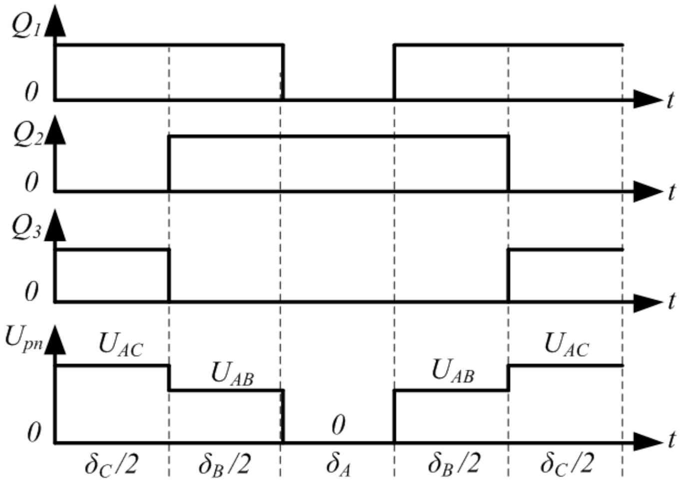

Figure 4.4. Switching actions and voltage steps during a switching period in Sector I.

For the drive system stage, the switches S1 and S2 of the inverter are kept off all the time. The switches S3 – S6 construct two power channels of an interleaved boost converter, which operate with 180 degree phase shift. The operational modes for Sector 1 are shown in Figure 4.5.

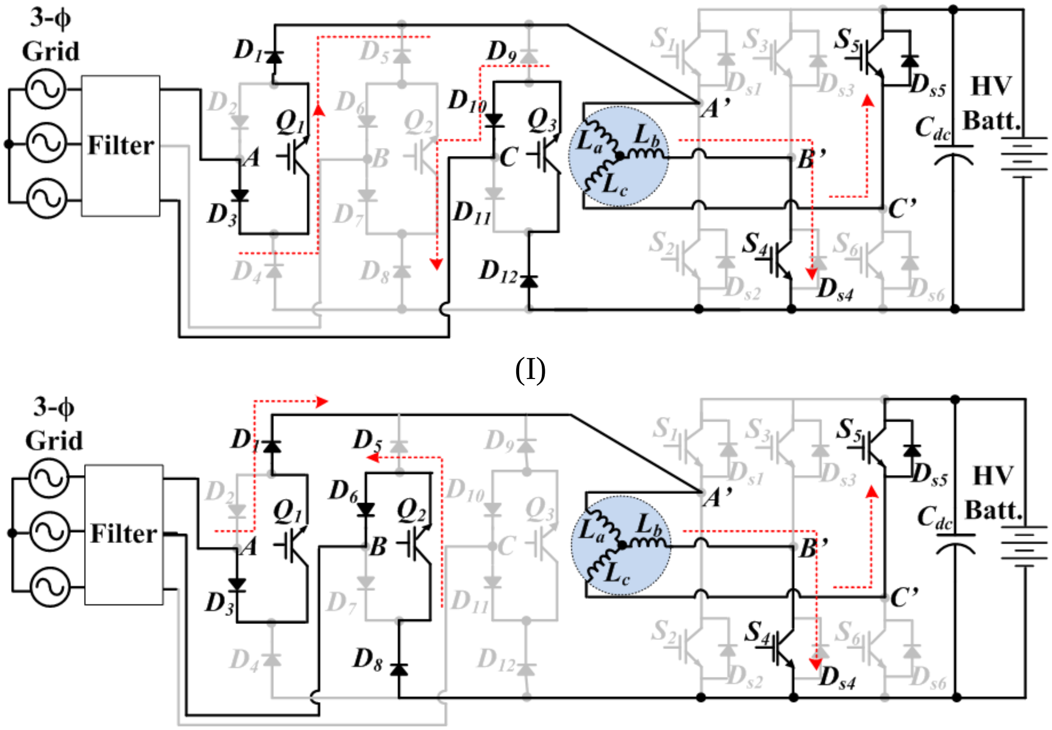

(I)

(II)

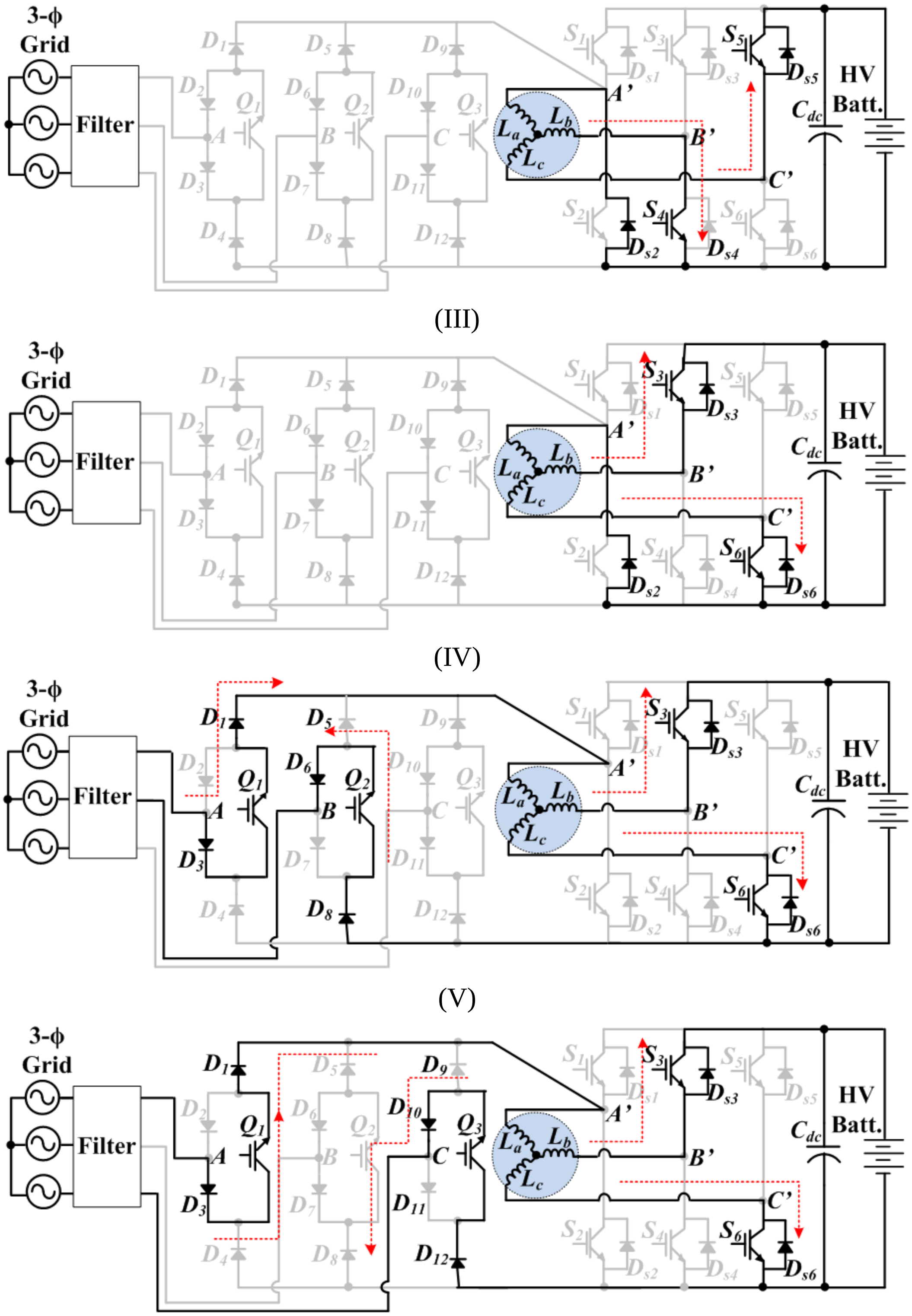

(III)

(IV)

(V)

(VI)

Figure 4.5. Operational modes of the circuit in Sector 1.

The current flowing directions are marked in Figure 4.5. In mode III and mode IV, the three switches in the three-phase interface are all off. The machine-winding current $i_L$ flows through the body diode $D_{S2}$.

In mode I, switches, $Q_1$ and $Q_3$, in the interface stage are turned on with the voltage over p and n points, $V_{pn}$, equal to line-to-line voltage, $V_{AC}$. In the propulsion system stage, switches, $S_4$ and $S_5$, are turned on. The voltage over machine-winding inductors, $L_a$ and $L_b$, is equal to $V_{AC}$, while the voltage over machine-winding inductors, $L_a$ and $L_c$, is equal to $V_o$ - $V_{AC}$. Thus, the slopes of machine-winding currents, $i_b$ and $i_c$, are derived as Eq. (4.4) and Eq. (4.5).

$$\frac{di_b}{dt} = -\frac{V_{AC}}{2L_{ph}} \tag{4.4}$$

$$\frac{di_c}{dt} = \frac{V_o - V_{AC}}{2L_{ph}} \tag{4.5}$$

In mode II, switches, $Q_1$ and $Q_2$, in the interface stage are turned on with the voltage between p and n points, $V_{pn}$, equal to the line-to-line voltage, $V_{AB}$. In the propulsion system stage, switches, $S_4$ and switch $S_5$, are turned on. The voltage over machine-winding inductors, $L_a$ and $L_b$, is equal to $V_{AB}$, while the voltage over machine-winding inductors, $L_a$ and $L_c$, is equal to $V_o$ - $V_{AB}$. Thus, the slopes of machine-winding currents, $i_b$ and $i_c$, are derived as Eq. (4.6) and Eq. (4.7).

$$\frac{di_b}{dt} = -\frac{V_{AC}}{2L_{ph}} \tag{4.6}$$

$$\frac{di_c}{dt} = \frac{V_o - V_{AB}}{2L_{ph}} \tag{4.7}$$

In mode III, all the switches in the interface stage, $Q_1$ - $Q_3$, are turned off, but the switches in the traction inverter, $S_4$ and $S_5$, are turned on. The voltage between p and n points, $V_{pn}$, equal to 0. The voltage over machine-winding inductors, $L_a$ and $L_b$, is equal to 0, while the voltage over machine-winding inductors, $L_a$ and $L_c$, is equal to -$V_o$. The machine-winding inductor current, $i_b$, circulates through a loop, which is formed by the machine-winding inductor $L_b$, the switch $S_4$, the body diode $D_{S2}$, and the machine-winding inductor $L_a$. The machine-winding inductor current, $i_c$, flows thought the switch $S_5$. The slopes of machine-winding currents, $i_b$ and $i_c$, are derived as Eq. (4.8) and Eq. (4.9).

$$\frac{di_b}{dt} = const. \tag{4.8}$$

$$\frac{di_c}{dt} = \frac{V_o}{2L_{ph}} \tag{4.9}$$

In mode IV, all the switches in the interface stage, $Q_1$ - $Q_3$, are turned off with the voltage between p and n points, $V_{pn}$, equal to 0. The switches $S_3$ and $S_6$ are turned on. Thus, the voltage over machine-winding inductors, $L_a$ and $L_c$, is equal to 0, and the voltage over machine-winding inductors, $L_a$ and $L_b$, is equal to -$V_o$. The machine-winding inductor current, $i_c$, circulates through a loop, which is formed by formed by the machine-winding inductor $L_c$, the switch $S_6$, the body diode $D_{S2}$, and the machine-winding inductor $L_a$. The machine-winding inductor current, $i_b$, flows thought the switch $S_3$. The slopes of machine-winding currents, $i_b$ and $i_c$, are derived as Eq. (4.10) and Eq. (4.11).

$$\frac{di_b}{dt} = \frac{V_o}{2L_{ph}} \tag{4.10}$$

$$\frac{di_c}{dt} = const. \tag{4.11}$$

In mode V, switches $Q_1$ and $Q_2$ in the interface stage are turned on with the voltage between p and n points, $V_{pn}$, equal to the line-to-line voltage, $V_{AB}$. In the propulsion system stage, switches, $S_3$ and $S_6$, are turned on. The voltage over machine-winding inductors, $L_a$ and $L_c$, is equal to $V_{AB}$, and the voltage over machine-winding inductors, $L_a$ and $L_b$, is equal to $V_o$ - $V_{AB}$. The slopes of machine-winding currents, $i_b$ and $i_c$, are derived as Eq. (4.12) and Eq. (4.13).

$$\frac{di_b}{dt} = \frac{V_o - V_{AB}}{2L_{ph}} \tag{4.12}$$

$$\frac{di_c}{dt} = -\frac{V_{AB}}{2L_{ph}} \tag{4.13}$$

In mode VI, switches $Q_1$ and $Q_3$ in the interface stage are turned on with the voltage between p and n points, $V_{pn}$, equal to the line-to-line voltage, $V_{AC}$. In the propulsion system stage, switches, $S_3$ and $S_6$, are turned on. The voltage over machine-winding inductors, $L_a$ and $L_c$, is equal to $V_{AC}$, and the voltage over machine-winding inductors, $L_a$ and $L_b$, is equal to $V_o$ - $V_{AC}$. The slopes of machine-winding currents, $i_b$ and $i_c$, are derived as Eq. (4.14) and Eq. (4.15).

$$\frac{di_b}{dt} = \frac{V_o - V_{AC}}{2L_{ph}} \tag{4.14}$$

$$\frac{di_c}{dt} = -\frac{V_{AC}}{2L_{ph}} \tag{4.15}$$

The phase-A machine-winding current, $i_a$, is the sum of the phase-B machine-winding current, $i_b$, and phase-C machine-winding current, $i_c$. Based on the analysis of operation modes, the current ripple of the phase-A machine winding, $\Delta i_a$, can be derived as Eq. (4.16).

$$\Delta i_a = \frac{MT}{2L_{ph}V_{Npk}}\left(-V_o v_{na} + 2{v_{nc}}^2\right) + \frac{V_o|D-0.5|T}{2L_{ph}} \tag{4.16}$$

where, $T$ is the switching period.

Table 4.1 lists the switching states and related voltages for each mode.

Table 4.1
Switching states and related voltages for each mode

| | Mode I | Mode II | Mode III |
|---|---|---|---|
| Three-phase interface stage | Q1 on Q3 on<br>Q2 off | Q1 on Q2 on<br>Q3 off | Q1 off Q2 off<br>Q3 off |
| Vpn | $V_{AC}$ | $V_{AB}$ | 0 |
| Drive system stage | S4 on S5 on<br>S3 off S6 off | S4 on S5 on<br>S3 off S6 off | S4 on S5 on<br>S3 off S6 off |
| Voltage over La & Lb<br>Voltage over La & Lc | $V_{AC}$<br>$V_o$- $V_{AC}$ | $V_{AB}$<br>$V_o$- $V_{AB}$ | 0<br>-$V_o$ |
| | Mode IV | Mode V | Mode VI |
| Three-phase interface stage | Q1 off Q2 off<br>Q3 off | Q1 on Q1 off<br>Q3 off Q3 off | Q2 off Q1 on<br>Q3 off |
| Vpn | 0 | $V_{AB}$ | $V_{AC}$ |
| Drive system stage | S3 on S6 on<br>S4 off S5 off | S3 on S3 on<br>S4 off S4 off | S6 on S3 on<br>S5 off S4 off |
| Voltage over La & Lb<br>Voltage over La & Lc | -$V_o$<br>0 | $V_o$- $V_{AB}$<br>$V_{AB}$ | $V_o$- $V_{AC}$<br>$V_{AC}$ |

In charging mode, the current flow into the phase-A machine winding and is evenly distributed between the other two machine windings. Based on the machine-winding currents, the sum of the stator magnetic flux is in the direction of a-axis. Thus, the electromagnetic force is aligned with the a-axis, and the rotor is stationary with the electric angle as π/2 during battery charging mode. According to the Park transformation, the equivalent currents in d-axis ($i_d$) and q-axis ($i_q$) of the propulsion machine can be derived as Eq. (4.17) and Eq. (4.18), respectively, in terms of machine-winding currents ($i_a$, $i_b$, $i_c$) and electrical angle ($\theta_e$).

$$\begin{cases} i_d = \frac{2}{3}[i_a \sin\theta_e + i_b \sin(\theta_e - \frac{2\pi}{3}) + i_c \sin(\theta_e + \frac{2\pi}{3})] & (4.17) \\ i_q = \frac{2}{3}[i_a \cos\theta_e + i_b \cos(\theta_e - \frac{2\pi}{3}) + i_c \cos(\theta_e + \frac{2\pi}{3})] & (4.18) \end{cases}$$

The generated electromagnetic torque, $T_e$, can be derived as Eq. (4.19).

$$T_e = \frac{3}{2}[\lambda_m i_a \cos\theta_e + \frac{1}{2}(L_q - L_d) i_a^2 \sin(2\theta_e)] \tag{4.19}$$

According to Eq. (4.19), the electromagnetic torque is forced to be zero, and the electrical angle is equal to π/2 in charging mode.

## 4.2 Control Strategy of the Integrated Charger

In this system, both the duty cycle and the modulation index can be utilized to control the system. The duty cycle of the interleaved boost stage is set as constant 0.5, while the modulation index of the three-phase interface stage is utilized to regulate the input filter inductor current and the input filter capacitor voltage. The control strategy is shown in Figure 4.6.

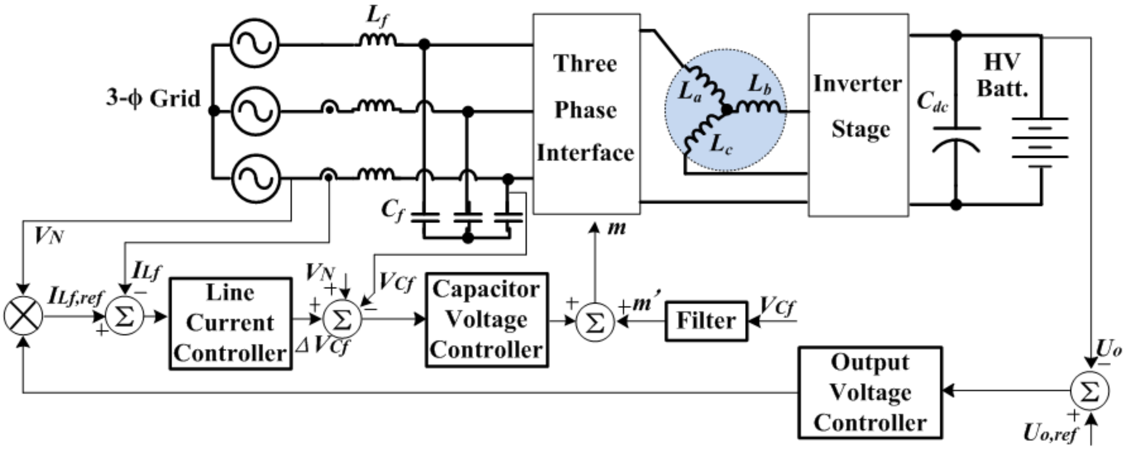

Figure 4.6. Control strategy of the integrated charger with three-switch interface.

There is an output voltage controller for the integrated charger. The cascaded control strategy is analyzed in detail in the following.

### 4.2.1 Control-Oriented Modeling

First, the small signal model of the circuit has to be built for the control strategy. The three-phase integrated charger can be considered as an equivalent buck-boost DC-DC converter circuit [62]. The equivalent circuit is the same as the circuit shown in Figure 3.6.

Based on the principle of energy conservation and power equality, the equivalent filter capacitance and equivalent filter inductance are quantified as Eq. (3.25) and Eq. (3.26). The equivalent input voltage is quantified as Eq. (3.22). The small signal model of the circuit is derived as Eq. (4.20) - (4.23).

$$\begin{cases} \dfrac{d\widetilde{i_{Lf}}}{dt} = -\dfrac{1}{L_{eq}}\widetilde{v_{Cf}} & (4.20) \\ \dfrac{d\widetilde{v_{Cf}}}{dt} = -\dfrac{M}{C_{eq}}\widetilde{\iota_L} - \dfrac{I_L}{C_{eq}}\widetilde{m} + \dfrac{1}{C_{eq}}\widetilde{i_{Lf}} & (4.21) \\ \dfrac{d\widetilde{\iota_L}}{dt} = \dfrac{M}{L_m}\widetilde{v_{Cf}} + \dfrac{V_{Cf}}{L}\widetilde{m} - \dfrac{D'}{L}\widetilde{v_o} + \dfrac{V_o}{L}\tilde{d} & (4.22) \\ \dfrac{d\widetilde{v_o}}{dt} = -\dfrac{I_L}{C_o}\tilde{d} + \dfrac{D'}{C_o}\widetilde{\iota_L} - \dfrac{1}{RC_o}\widetilde{v_o} & (4.23) \end{cases}$$

The small signal model of the circuit can be derived based on this model.

### 4.2.2 Design of Cascaded Control for Three-phase Interface

The multiloop cascaded control for three-phase interface is shown in Figure 4.7. The inner loop is used to control the input filter capacitor voltage. The intermediate loop is used to regulate the input filter inductor current. The outer loop is utilized to control the battery voltage.

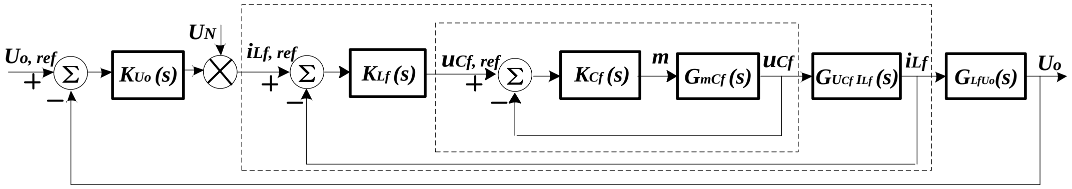

Figure 4.7. Multiloop cascaded control for three-phase interface.

For the inner capacitor voltage controller, the modulation index to input filter capacitor voltage transfer function, $G_{mv_{Cf}}(s)$, is derived based on the small signal model as Eq. (4.24).

$$G_{mv_{Cf}}(s) = \frac{\widetilde{v_{Cf}}}{\widetilde{m}} = \frac{-I_L LCs^3 - \left(MCU_{Neq} + \frac{I_L L}{R}\right)s^2 - \left[\frac{MU_{Neq}}{R} + I_L(1-D)^2\right]s}{LCC_{eq}s^4 + \frac{LC_{eq}}{R}s^3 + \left[(1-D)^2 C_{eq} + \frac{LC}{L_{eq}} + M^2 C\right]s^2 + \left(\frac{L}{RL_{eq}} + \frac{M^2}{R}\right)s + \frac{(1-D)^2}{L_{eq}}} \quad (4.24)$$

The controller of the capacitor voltage control, $K_{Cf}(s)$, is designed as a PI controller.

$$K_{Cf}(s) = k_{pCf} + \frac{k_{iCf}}{s} \tag{4.25}$$

where, the $k_{pCf}$ is selected as -0.3, and $k_{iCf}$ is selected as $-6000$.

Figure 4.8 shows the bode plot of the uncompensated and compensated system.

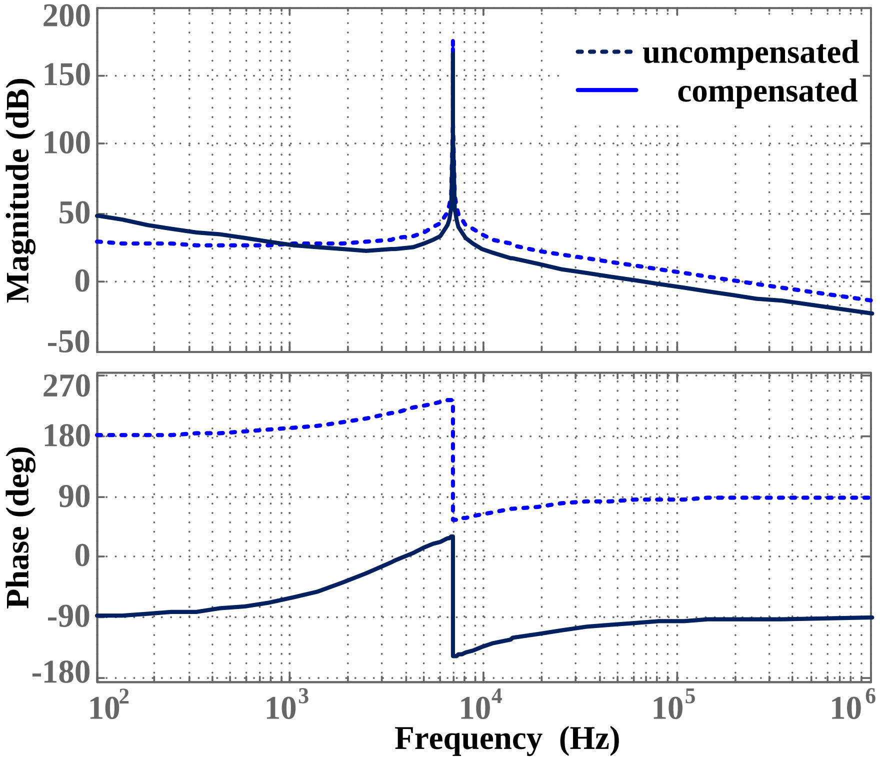

Figure 4.8. Bode plot of the input filter capacitor voltage control loop.

For the intermediate inductor current control, the transfer function of the modulation index to the input filter inductor current, $G_{v_{Cf}i_{Lf}}(s)$, is derived as Eq. (4.26).

$$G_{v_{Cf}i_{Lf}}(s) = \frac{\widetilde{i_{Lf}}}{\widetilde{v_{Cf}}} = \frac{-1}{sL_{eq}} \tag{4.26}$$

The dynamics of the input filter capacitor voltage control is taken into consideration when designing the controller of the input filter inductor current control.

The filter inductor current controller, $K_{Lf}(s)$, is design as a PID controller.

$$K_{Lf}(s) = k_{cm}\frac{\left(1+\frac{\omega_L}{s}\right)\left(1+\frac{s}{\omega_z}\right)}{\left(1+\frac{s}{\omega_{p1}}\right)\left(1+\frac{s}{\omega_{p2}}\right)} \tag{4.27}$$

where, the $k_{cm}$ is designed as -10, $\omega_L$ is selected as $10^5$, $\omega_{p1}$ is selected as $10^6$, $\omega_z$ is selected as $10^5$, and $\omega_{p2}$ is selected as $5 \times 10^6$.

Figure 4.9 shows the bode plot of the uncompensated control path and the compensated control path.

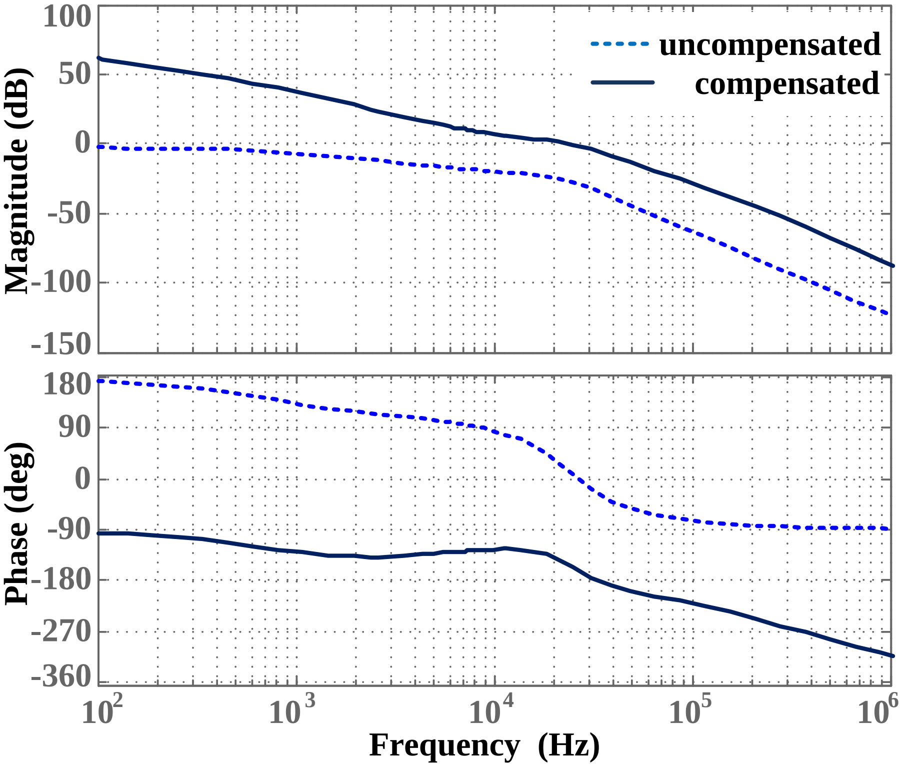

Figure 4.9. Bode plot of the input filter inductor current control loop.

For the output voltage control of the three-phase interface stage, the input filter inductor current to the output voltage transfer function, $G_{v_o i_{Lf}}(s)$, is derived as Eq. (4.28).

$$G_{v_o i_{Lf}}(s) = \frac{\widetilde{v_o}}{\widetilde{i_{Lf}}} = \frac{V_{Neq} L_{eq} C_{eq} s^2 - I_L M L_{eq} + V_{Neq}}{I_L L C s^2 + \left(M C V_{Neq} + \frac{I_L L}{R}\right) s + \left[\frac{M V_{Neq}}{R} + I_L (1-D)^2\right]} \tag{4.28}$$

The output voltage controller, $K_{v_o i_{Lf}}(s)$, is designed as a PI controller.

$$K_{v_o i_{Lf}}(s) = k_p + k_i \frac{1}{s} \tag{4.29}$$

where, $k_p$ is selected as 0.01, and $k_i$ is selected as 0.1.

Figure 4.10 shows the bode plot of the uncompensated control path and the compensated control path.

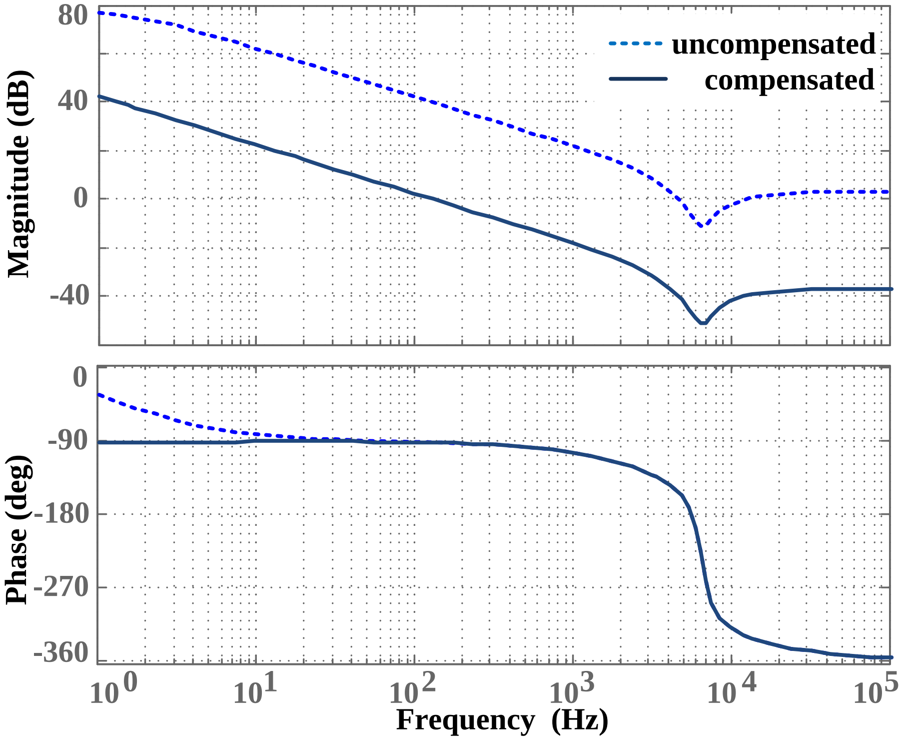

Figure 4.10. Bode plot of the input filter inductor current control loop.

## 4.4 Experimental Results

To verify the proposed integrated charger and the design of the control strategy, a 5kW proof-of-concept prototype is designed and developed at the Maryland Power Electronics Laboratory (MPEL).

The three-phase power grid is emulated by a three-phase 60-Hz AC power supply. Considering the variation of EV battery voltage during charging, the tested output voltage ranges from 295V to 410V. The overall performance of the prototype is presented in Table 4.2.

Table 4.2

Performance of prototype

| Parameters | Symbol | Value | Unit |
|---|---:|---:|---:|
| Input ac voltage | $v_{ac,rms}$ | 120 | V |
| Input frequency | $f_{ac}$ | 60 | Hz |
| Output dc voltage | $V_o$ | 295~410 | V |
| Maximum output power | $P_o$ | 5 | kW |
| Power factor | $PF$ | 0.99 | |
| Total harmonic distortion | $THD$ | 4.82 | % |
| Maximum efficiency | $E_{ff}$ | 93.2 | % |

Figure 4.11 shows the waveforms of the input current, input voltage, and the battery voltage at $V_o$=318$V$. The experimental results verify the feasibility of the proposed integrated charger. Due to the relatively high inductance of propulsion machine, the machine-winding current ripple is measured to be as low as 2A, which is only 10% of the peak current value, restricting the core loss from the propulsion

machine. Compared with the inductor current ripple of traditional battery chargers, the machine-winding current ripple of the proposed approach is much less.

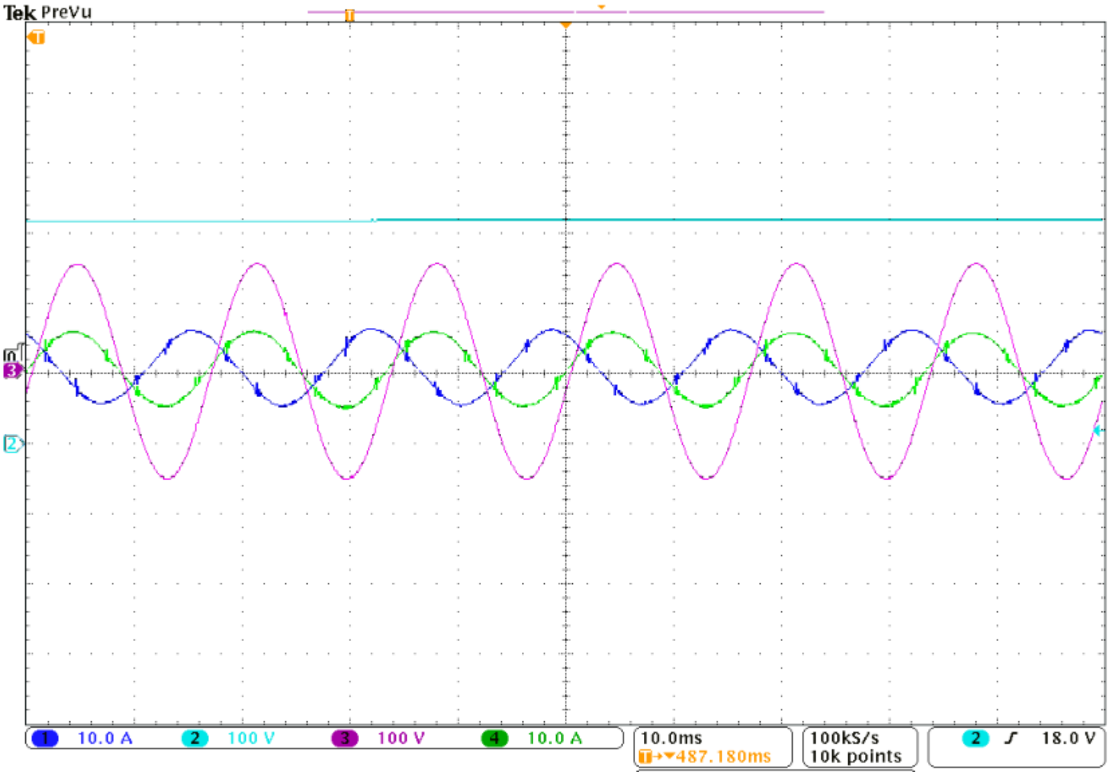

Figure 4.11. Waveforms of three-phase integrated onboard charger (CH1: input phase-B current, $I_{nb}$, 10A/div; CH2: output voltage, $V_o$, 100V/div; CH3: input phase-B voltage, $V_{nc}$, 100V/div; CH4: input phase-C current, $I_{nc}$, 10A/div) at $V_{in}$=120V,rms, $V_o$=318V.

Figure 4.12 shows the waveforms of the input current, input voltage, and the battery voltage at $V_o$=380$V$.

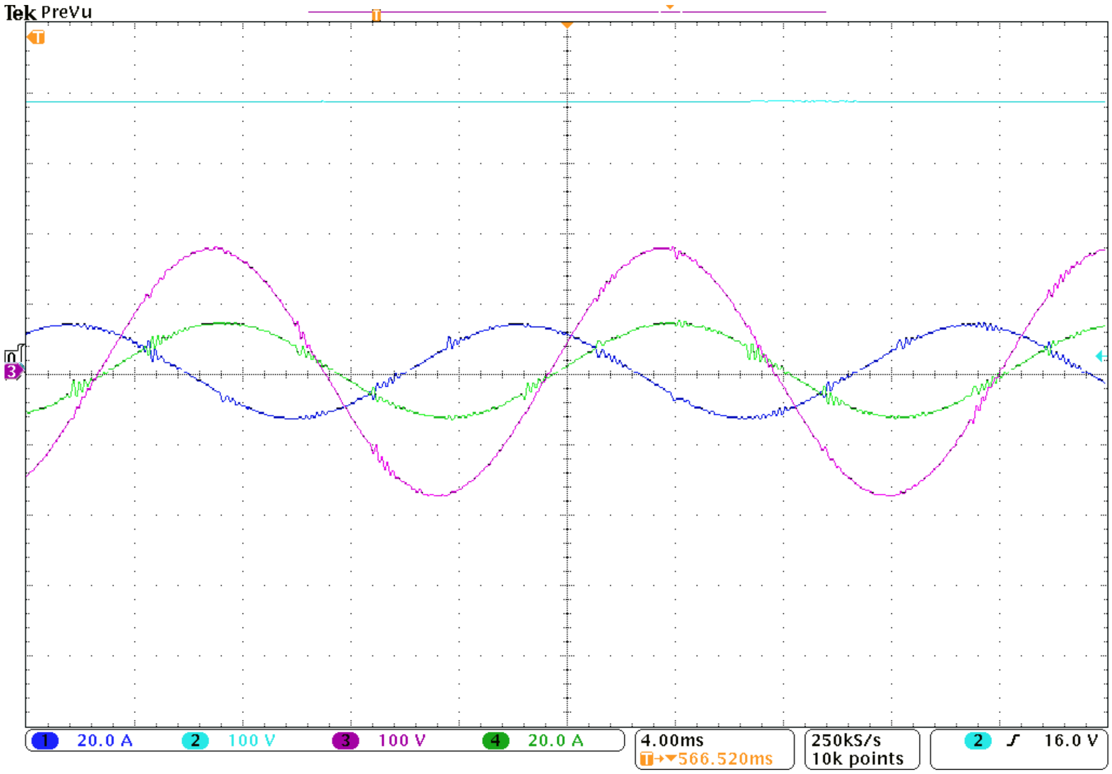

Figure 4.12. Waveforms of three-phase integrated onboard charger (CH1: input phase-B current, $I_{nb}$, 10A/div; CH2: output voltage, $V_o$, 100V/div; CH3: input phase-B voltage, $V_{nc}$, 100V/div; CH4: input phase-C current, $I_{nc}$, 10A/div) at $V_{in}$=120V,rms, $V_o$=380V.

Figure 4.13 shows the waveforms of the input current, input voltage, and the battery voltage at full power and $V_o$=410$V$.

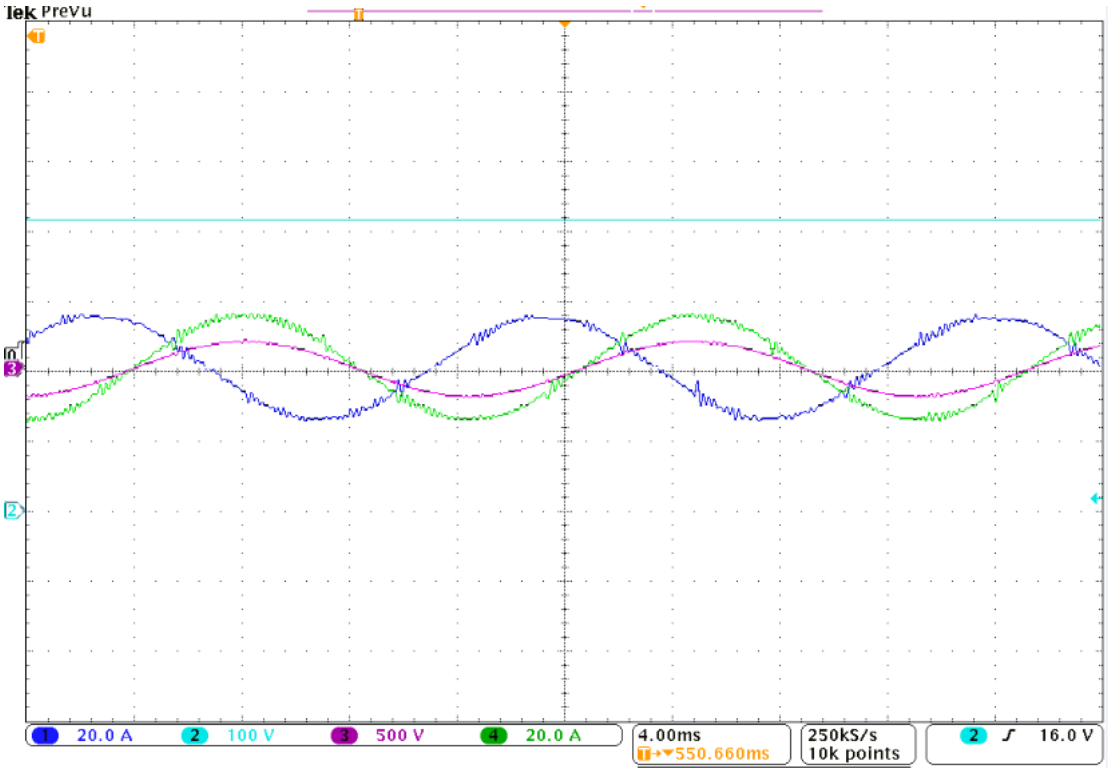

Figure 4.13. Waveforms of three-phase integrated onboard charger (CH1: input phase-A current, $I_{nc}$, 20A/div; CH2: output voltage, $V_o$, 100V/div; CH3: voltage phase-C voltage, $V_{nc}$, 500V/div; CH4: input phase-C current, $I_{nc}$, 20A/div) at $V_{in}$=120V,rms, $V_o$=415V.

It is shown that the input phase current is in phase with the corresponding input phase voltage. The experimental results verify the feasibility of the proposed integrated charger.

Figure 4.14 shows the waveforms of gating signals for the switches $S_4$ and $S_6$ in the propulsion system stage, the waveform of phase-B machine-winding current, and phase-C machine-winding current. The gating signal of the switch S4 has 180 degrees phase shift to the gating signal of the switch S6 in the propulsion system stage.

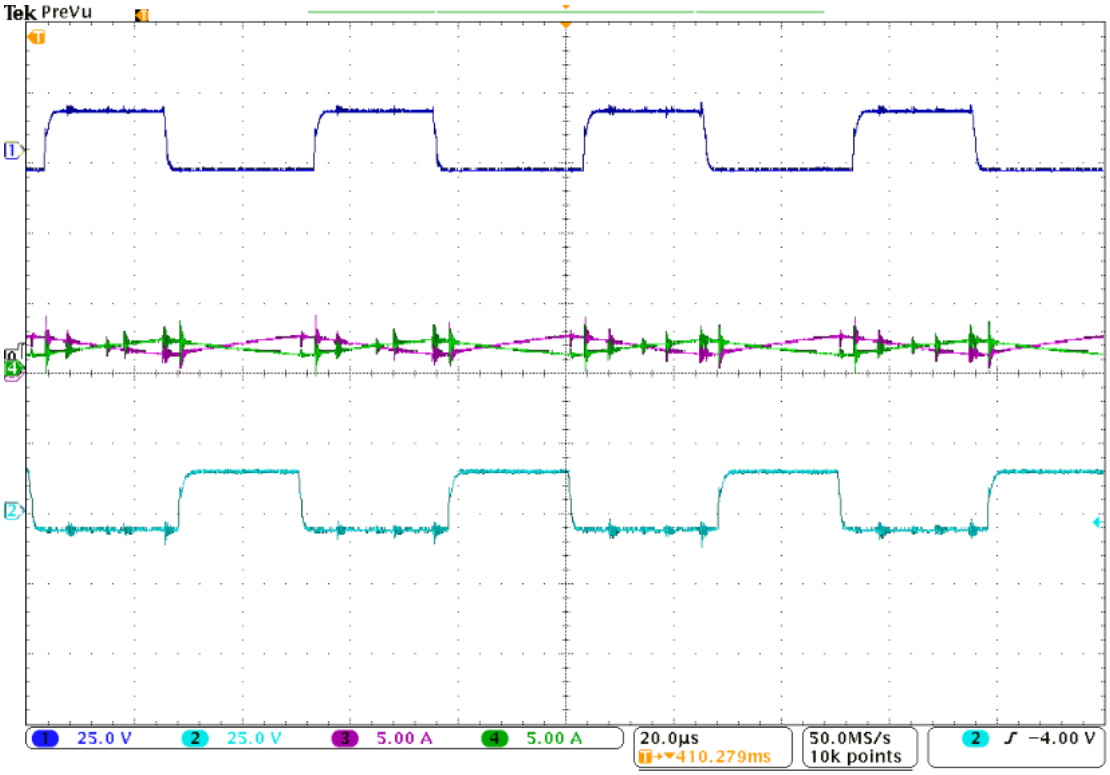

Figure 4.14. Switching waveforms (CH1: gating signal for switch $S_4$, $V_{GS4}$, 25V/div; CH2: gating signal for switch $S_6$, $V_{GS6}$, 25V/div; CH3: phase-C machine-winding current, $I_c$, 5A/div; CH4: phase-B machine-winding current, $I_b$, 5A/div).

Correspondingly, the phase-B machine-winding current has 180 degrees phase shift to the phase-C machine-winding current in the propulsion machine. The experimental results are consistent with the theoretical analysis of the operation modes in the propulsion system stage.

Figure 4.15 shows the waveforms of gating signals for the three switches in the interface stage and the waveform of phase-B input current. The voltage levels of the gating signals are +15V during the on-state and -10V during the off-state.

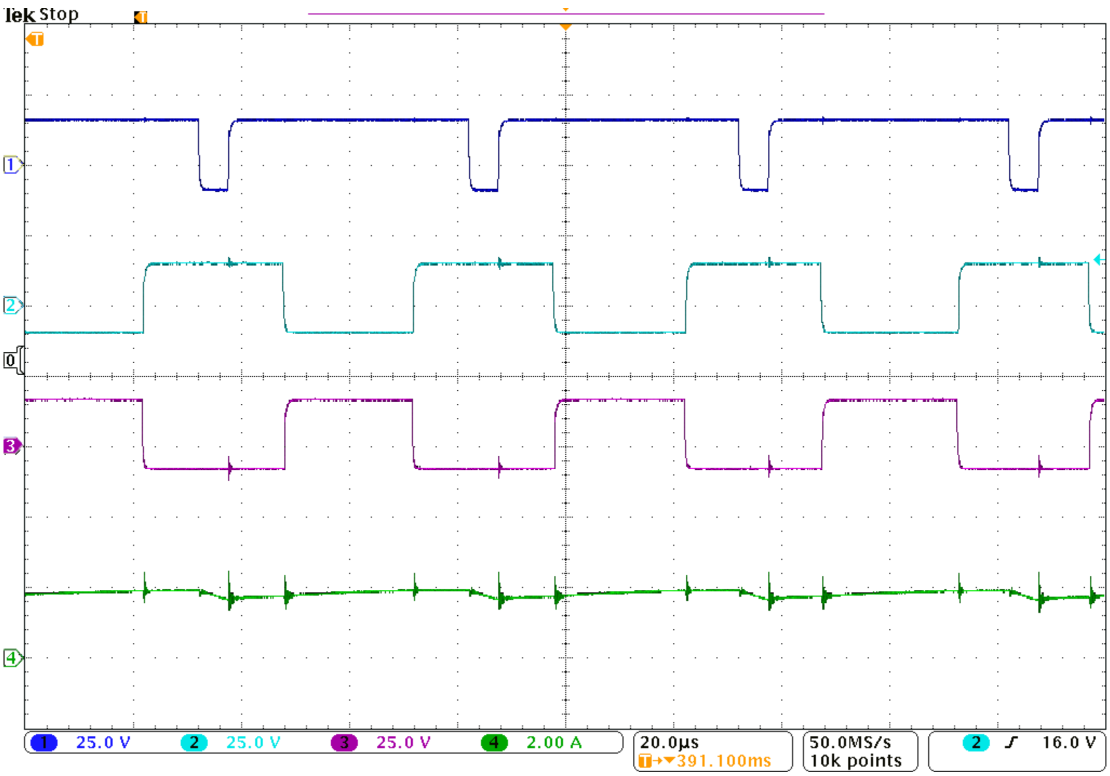

Figure 4.15. Switching waveforms (CH1: gating signal for switch $Q_1$, $V_{GQ1}$, 25V/div; CH2: gating signal for switch $Q_2$, $V_{GQ2}$, 25V/div; CH3: gating signal for switch $Q_3$, $V_{GQ3}$, 25V/div; CH4: input phase-B current, $I_{nb}$, 5A/div).

The experimental results are consistent with the theoretical analysis of the operation modes in the interface stage.

To verify the stability of the control system, Figure 4.16 is provided to show the transient process at rated voltage levels when the input currents changed from 7A to 3.5A then back to 7A at $V_{in}$=120$V_{,rms}$, $V_o$=410$V$. The output voltage is kept as 410V during the transient process. The experimental results show that the input phase current is in phase with the corresponding input phase voltage.

In Figure 4.16, the system took 15 millisecond and 16 millisecond to reach the steady state when the load changed from full load to half load and from half load to full load, respectively. The experimental results of load transient are consistent with the theoretical bandwidth of 350Hz as designed.

On the other hand, the input phase-B current stays sinusoidal during all the load transient process. It means that the bandwidth of input filter inductor currents is at least 10 times higher than 350Hz, which is consistent with the 4.5 kHz bandwidth of the input inductor current as designed.

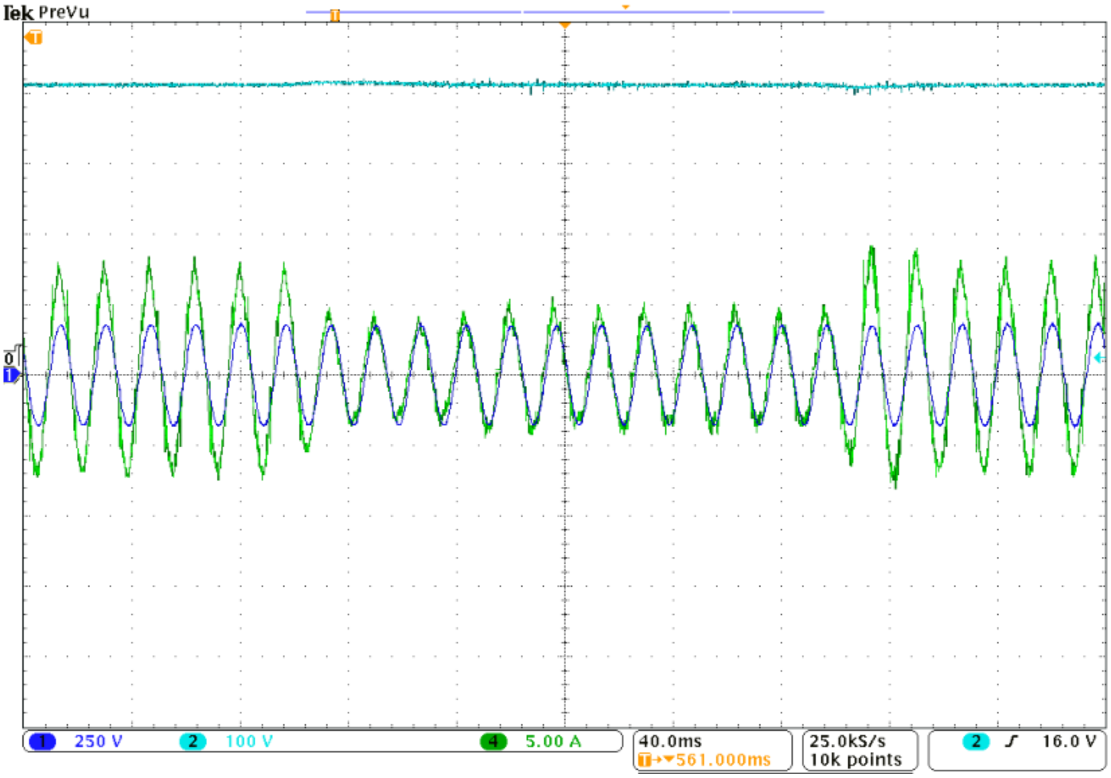

Figure 4.16. Transient waveforms (CH1: phase-B input voltage, $V_{nb}$, 250V/div; CH2: output voltage, $V_o$, 100V/div; CH4: input phase-B current, $I_{nb}$, 5A/div) at $V_{in}$=120$V_{,rms}$, $V_o$=410$V$.

The efficiency curve of the proposed integrated charger is shown in Figure 4.17. The peak efficiency is measured as 93.2%.

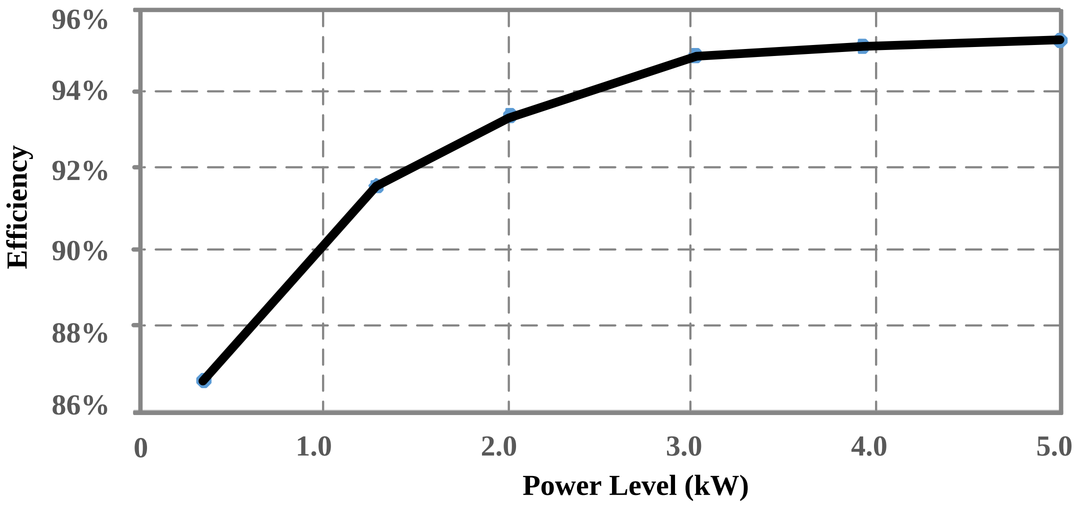

Figure 4.17. Efficiency curve of the proposed integrated charger.

The loss breakdown is provided for the circuit at input voltage ($V_{in}$ = 110V$_{,rms}$), output voltage ($V_o$ = 410V), and full load ($P_{out}$ = 5kW), as shown in Figure 4.18.

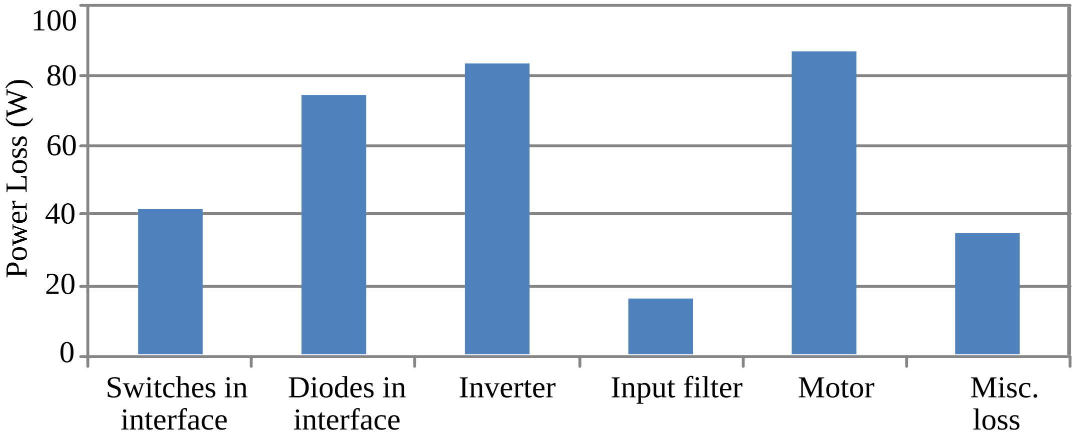

Figure 4.18. Loss breakdown at $V_{in}$ = 120V$_{,rms}$, $V_o$ = 410V, and $P_{out}$ = 5kW.

The miscellaneous power loss mainly contains the power loss caused by PCB traces, gate drives, etc. Due to the utilization of SiC semiconductors, the interface has less power loss than that of the inverter. The loss breakdown shows that majority of power loss is caused by the propulsion system, including the propulsion machine and the inverter.

## 4.5 Summary

In this chapter, a three-phase integrated onboard battery charger is introduced, investigated and designed for EVs. The integrated charger consists of a three-phase three-switch interface and the EV's propulsion system. The machine and the inverter serve as a two-channel interleaved boost converter. A dual cascaded control strategy is proposed and designed for the integrated charger. The proposed control strategy regulates the input current, the machine-winding current and the output voltage simultaneously. The small signal model is derived, and the design of controller is provided. A 5kW proof-of-concept prototype is built and tested. A 0.99 PF and 4.82% THD are obtained at 5kW with efficiency as 93.2%.

# Chapter 5: Conclusion and Future Work

## 5.1 Conclusions

This work for the first time proposed and successfully demonstrated practical propulsion-machine-integrated charging approaches for EVs.

A single-phase propulsion-machine-integrated charger was developed. The machine windings of the propulsion machine were utilized as PFC inductors in the charging mode. Thus, there were no bulky inductors in the interface. The components required for the battery charging were simplified as one diode bridge, significantly reducing the size of the charging system. The theoretical analysis and experiments were carried out to validate the functionality of the proposed approach. The PF was measured as 0.98, and the THD of the input currents was measured as 3.96%. A peak efficiency of 93.1% was obtained in test.

Then, two three-phase integrated solutions were introduced. In the first three-phase approach, a six-switch interface was proposed, developed and designed for three-phase integrated charging. The add-on device for the integrated charging is the three-phase interface, which mainly consists of semiconductors and EMI filters. Thus, the size of the interface is much smaller the three-phase offboard chargers, and onboard setting of the interface can be applied, greatly reducing the size and cost of three-phase battery charging. The feasibility of the proposed approach was verified by theoretical analysis and experimental results. A 3.3kW prototype was construct, achieving the PF as 0.98, the THD of the input current as 4.77%, and a peak efficiency of 92.6% in experiments. The power density of the interface is 31W/in$^3$.

The second three-phase integrated onboard charging approach aimed at further reducing the size of the system. The count of transistors is reduced to three, simplifying the gate driving circuit and the charging topology. The size of the interface can be further reduced, and the power density of the interface increases by 40%. The proposed topology was proved to be feasible by experimental results. A three-phase three-switch interface was proposed and designed. A 5kW prototype was built with the power density of the interface increased to 52W/in$^3$. The THD of input currents is 4.82%, and the PF is 0.99. The peak efficiency was measured as 93.2% at 5kW.

### 5.2 Future Work

Although multiple propulsion-machine-integrated charging approaches for EVs are thoroughly investigated and successfully demonstrated, the research of this topic is not exhaustive. There are several advancements that can be made to further enhance the performance of the integrated chargers. The following areas could benefit from further investigations.

#### 5.2.1 Novel Control Algorithms

One benefit of the integrated onboard charger is that both the switches in the interface and the switches in the inverter can be controlled to regulate the currents and voltages of the charger. There are two degrees of freedom available for the design of the charger control system. Therefore, the dynamic performance of the integrated charger can be enhanced compared to the traditional three-phase off-board chargers that usually have only one degree of freedom. A beneficial extension of this work would be to develop novel control strategies to improve the dynamic performance under transient operation. The switches in interface could be utilized to control the input voltage and input current, while the switches in inverter could be exploited to regulate the output voltage and the machine-winding currents. Due to the ability to ensure stability and robustness against various circuit parameters, the sliding mode control (SMC) could be a potential choice. In addition, multivariable optimization control could be applied to control the input parameters and output parameters simultaneously in transient processes. Developing novel control algorithms, improving the dynamic performance of the integrated chargers can further enhance the value of proposed system.

### 5.2.2 Wide-Band-Gap Devices for Improved Efficiency

To increase the power level of three-phase integrated onboard charger above 10kW, the insulated gate bipolar transistors (IGBTs) are preferred to build the power interface rather than the power MOSFETs due to the much lower on-state voltage drop and smaller chip sizes of IGBTs at the same current and voltage ratings. However, IGBTs suffer from tail-current effect during turn-off, resulting in relatively long turn-off time and limited switching speed. The drawbacks constrain the application of IGBT and the performance of IGBT-based integrated charger of high power levels.

The emerging wide-band-gap (WBG) power semiconductors provide a promising solution to further improve the performance of three-phase integrated chargers. Due to the high voltage and current ratings, the Silicon Carbide (SiC) switches have the adequate competency to be adopted for power devices. The critical breakdown strength of SiC material is approximately 10 times than that of traditional Si material. In addition, the thickness of drift layer in SiC transistors is one-tenth the thickness of the drift layer in comparable Si transistors. The SiC characteristics can lead to dramatic reductions in electrical resistance and switching loss in power devices. Moreover, SiC has three times higher band gap width and thermal conductivity than Si, which enables SiC transistors to operate at high temperatures reducing cooling requirements and improving power density of converter.

Thus, a significant avenue for future work is to perform a thorough evaluation for potential use of full SiC power modules or hybrid SiC power modules to improve the performance of three-phase integrated onboard chargers. Full SiC power modules use SiC material to fabricate the switching devices, which can be built with or without freewheeling diodes, thus increasing the switching frequency and efficiency at the same time.

Hybrid SiC power modules provide a cost-effective solution for industrial-scale applicability of the integrated chargers. The power modules combine IGBT switches with the SiC schottky free-wheeling diodes to leverage the low cost of traditional IGBT switches and the low power loss of SiC diodes. The combination could reduce the overall module switching losses by 30% with no change of gate drive circuits. Since the SiC chip area is relatively small, the replacement of traditional IGBTs modules by hybrid SiC modules causes moderate impact on the overall cost of the integrated chargers.

Therefore, the application of WBG power modules open up significant performance improvements for integrated chargers in the next-generation EVs and could greatly facilitate the advancement of integrated chargers towards industrial-scale applicability.

### 5.2.3 Impact on Lifetime of Propulsion Machine

Another focus of future work could be to comprehensively analyze the impact of integrated charging operation on the propulsion machine. In charging mode, the machine windings of a propulsion machine serve as coupled inductors. The propulsion machines are used both in propulsion mode and charging modes of EVs, resulting in prolonged operation period of propulsion machines. However, to our knowledge, the impact of integrated charging on propulsion machines is not thoroughly investigated by researchers before. Thus, development of methodology to evaluate the impact of integrated charging on propulsion machines would be a significant contribution to the advancement of the integrated charging techniques. Finite element analysis (FEA) could be conducted on the propulsion machine in charging mode in terms of current distribution, electromagnetic field distribution, temperature distribution, and strain distribution. Based on FEA results, a mathematical model for lifetime of propulsion machines could be derived to quantify the impact of integrated charging. It would be practically illustrative to conduct the analysis on commercial propulsion machines and estimate the impact on lifetime.

# Bibliography

[1] C. C. Chan, A. Bouscayrol, and K. Chen, “Electric, hybrid, and fuel-cell vehicles: Architectures and modeling,” IEEE Trans. Veh. Technol., vol. 59, no. 2, pp. 589-598, Feb. 2010.

[2] D. Gautam, F. Musavi, M. Edington, W. Eberle, and W. G. Dunford, “An automotive onboard 3.3 kW battery charger for PHEV application,” in *Proc. IEEE VPPC,* Chicago, IL, Sep. 2011, pp. 1-6.

[3] A. Khaligh and S. Dusmez, “Comprehensive topological analysis of conductive and inductive charging solutions for plug-in electric vehicles,” *IEEE Trans. Veh. Technol.*, vol. 61, no. 8, pp. 3475-3489, Oct. 2012.

[4] J. P. M. Figuerido, F. L. Tofili, and B. L. A. Silva, “A review of single-phase PFC topologies based on the boost converter,” in *Proc. IEEE Int. Conf. Ind. Appl.,* Sao Paulo, Brazil, Nov. 2010, pp. 1-6.

[5] D. C. Erb, O. C. Onar, and A. Khaligh, “Bi-directional charging topologies for plug-in hybrid electric vehicles,” *in Proc. IEEE APEC,* Feb. 2010, pp. 2066-2072.

[6] C. Shi, A. Khaligh and H. Wang,"Interleaved SEPIC Power Factor Preregulator Using Coupled Inductors In Discontinuous Conduction Mode With Wide Output Voltage", *IEEE Trans. on Ind. Appl.*, vol.52, no. 4, pp.3461 - 3471, Apr. 2016.

[7] B.K. Lee, J.P. Kim, S.G. Kim, and J.Y. Lee, “A PWM SRT DC/DC Converter for 6.6-kW EV Onboard Charger”, *IEEE Trans. Ind. Electron.,* vol. 63, no. 2, pp. 894-902, Feb. 2016.

[8] M. Yilmaz and P. T. Krein, “Review of charging power levels and infrastructure for plug-in electric and hybrid vehicles,” in *Proc. Int. IEEE Electric Vehicle Conf.*, Greenville, SC, Mar. 2012, pp. 1-8.

[9] T. Bohn, Plug-in Electric (PEV) Standards, Upcoming PEVs/Features, charging system overview, U.S Dept. of Energy, Clean Cities Coalition, Golden, CO. [Online]. Available: http://www1.eere.energy.gov/cleancities/

[10] S. A. Singh and S. S. Williamson, "Comprehensive review of PV/EV/grid integration power electronic converter topologies for DC charging applications," *2014 IEEE Transportation Electrification Conference and Expo (ITEC)*, Dearborn, MI, 2014, pp. 1-5.

[11] T. Bohn, “Plug-in Electric (PEV) Standards, Upcoming PEVs/Features, charging system overview”, U.S Dept. of Energy, Clean Cities Coalition, Golden, CO. [Online]. Available: http://www1.eere.energy.gov/cleancities/

[12] T. B. Soeiro, M. L. Heldwein, and J. W. Kolar, "Three-phase modular multilevel current source rectifiers for electric vehicle battery charging systems", *Brazilian Power Electronics Conference*, pp. 623 - 629, Oct. 2013.

[13] S. Haghbin, S. Lundmark, M. Alakula, and O. Carlson, “Grid-connected integrated battery chargers in vehicle applications: Review and new solution”, *IEEE Trans. on Ind. Electron*., vol. 60, no. 2, pp. 459-473, Feb. 2013.

[14] J. de Santiago, H. Bernhoff, B. Ekergård, S. Eriksson, S. Ferhatovic, R. Waters, and M. Leijon, “Electrical Machine Drivelines in Commercial All-Electric Vehicles: A Review,” IEEE Trans. Veh. Technol., vol. 61, no. 2, pp. 475-484, 2012.

[15] K. T. Chau, C. C. Chan, and C. Liu, “Overview of permanent-magnet brushless drives for electric and hybrid electric vehicles,” *IEEE Trans. Ind. Electro*., vol. 55, no. 6, pp. 2246-2257, Jun. 2008.

[16] J. G. W. West, “DC, induction, reluctance and PM machines for electric vehicles,” *Power Engineering J.*, vol. 8, no. 2, pp. 77-88, Apr. 1994.

[17] S.S. Williamson, A.K. Rathore, F. Musavi, “Industrial electronics for electric transportation: current state-of-the-art and future challenges”, *IEEE Trans. Ind. Electron*., vol. 62, no. 5, pp. 3021-3032, May 2015.

[18] H. Chang and C. Liaw, “An integrated driving/charging switched reluctance machine drive using three-phase power module,” *IEEE Trans. Ind. Electro*., vol. 58, no. 5, pp. 1763-1775, May 2011.

[19] G. Pellegrino, E. Armando, and P. Guglielmi, “An integral battery charger with power factor correction for electric scooter,” *IEEE Trans. on Power Electron*., vol. 25, no. 3, pp.751-759, Mar. 2010.

[20] G. Pellegrino, E. Armando and P. Guglielmi, "An integral battery charger with Power Factor Correction for electric scooter," *2009 IEEE International Electric Machines and Drives Conference*, Miami, FL, 2009, pp. 661-668.

[21] D. G. Woo, D. M. Joo, and B. K. Lee, “On the feasibility of integrated battery charger utilizing traction machine and inverter in plug-in hybrid electric vehicles,” *IEEE Trans. on Power Electron*., vol. 30, no. 12, pp.7270-7281, Dec. 2015.

[22] J. M. Slicker, “Pulse width modulation inverter with battery charger,” U.S. Patent 4 491 768, Jan. 1, 1985.

[23] Y. J. Lee and A. Emadi, "Integrated Bi-Directional AC/DC and DC/DC Converter for Plug-in Hybrid Electric Vehicle Conversion," *2007 IEEE Vehicle Power and Propulsion Conference*, Arlington, TX, 2007, pp. 215-222.

[24] L. De-Sousa and B. Bouchez, “Combined electric device for powering and charging,” Int. Patent WO 2010/057892 A1, May 27, 2010.

[25] I. Subotic, N. Bodo, E. Levi, M. Jones, and V. Levi, “Isolated chargers for EVs incorporating six-phase machines”, *IEEE Trans. Ind. Electron.*, vol. 63, no. 1, pp. 653-664, Jan. 2016.

[26] I. Subotic, N. Bodo, E. Levi, and M. Jones, “Onboard integrated battery charger for EVs using an asymmetrical nine-phase machine”, *IEEE Trans. Ind. Electron.*, vol. 62, no. 5, pp. 3285-3295, May 2015.

[27] S. Sul and S. Lee, “An integral battery charger for four-wheel drive electric vehicle,” *IEEE Trans. Ind. Appl.*, vol. 31, no. 5, pp. 1096-1099, Sep./Oct. 1995.

[28] T. H. Liu, Y. Chen, P. H. Yi, J. L. Chen, "Integrated Battery with Power Factor Correction for Electric-Propulsion Systems", *IET Electric Power Applications*, vol. 9, no. 3, 2015, pp. 229-238.

[29] S. Lacroix, E. Laboure, and M. Hilairet, “An integrated fast battery charger for electric vehicle,” in *Proc. IEEE VPPC*, Sep. 1-3, 2010, pp. 1-6.

[30] S. Q. Ali, D. Mascarella, G. Joos, T. Coulombe, and J. M. Cyr, “Three Phase High Power Integrated Battery Charger for Plugin Electric Vehicles”, in *Proc. of VPPC, IEEE,* Oct. 2015, pp. 1-6.

[31] S. D. Mohamed, A. A. Elserougi, and A. S. Abdel-Khalik, A. M. Massoud, S. Ahmed, "A Nine-Switch-Converter-Based Integrated Machine Drive and Battery Charger System for EVs Using Symmetrical Six-Phase Machines", *IEEE Trans. on Ind. Electron.*, vol. 63, no. 9 , pp. 5326 - 5335, Sept. 2016.

[32] Y. J. Lee, A. Khaligh, and A. Emadi, “Advanced integrated bidirectional ac/dc and dc/dc converter for plug-in hybrid electric vehicles,” *IEEE Trans. Veh. Technol.*, vol. 58, no. 8, pp. 3970-3980, Oct. 2009.

[33] H. Chen, X. Wang, and A. Khaligh, “A single stage integrated bidirectional ac/dc and dc/dc converter for plug-in hybrid electric vehicles,” in *Proc. IEEE VPPC,* Sep. 6-9, 2011, pp. 1-6.

[34] S. Dusmez and A. Khaligh, “A novel low cost integrated onboard charger topology for electric vehicles and plug-in hybrid electric vehicles,” in *Proc. APEC*, Feb. 5-8, 2012, pp. 2611-2616.

[35] I. Subotic, N. Bodo, and E. Levi, “Single-phase on-board integrated battery chargers for EVs based on multiphase machines,” *IEEE Trans. on Power Electron.*, vol. 31, no. 9, pp.6511-6523, Sept. 2016.

[36] C. Li, W. Huang, R. Cao, F. Bu, and C. Fan, “An integrated topology of charger and drive for electric buses,” *IEEE Trans. on Veh. Technol.*, vol. 65, no. 6, pp.4471-4479, Jun. 2016.

[37] B. Liu, Z. Wang, Y. Zhang, M. Cheng and L. Xu, "The dual-channel magnetically integrated chargers for plug-in electric vehicles," *2016 IEEE Energy Conversion Congress and Exposition (ECCE)*, Milwaukee, WI, 2016, pp. 1-7.

[38] I. Subotic, E. Levi, M. Jones and D. Graovac, "An integrated battery charger for EVs based on an asymmetrical six-phase machine," *IECON 2013 - 39th Annual Conference of the IEEE Industrial Electronics Society*, Vienna, 2013, pp. 7244-7249.

[39] S. Haghbin, S. Lundmark, M. Alakula, and O. Carlson, “An isolated high power integrated charger in electrified-vehicle applications,” *IEEE Trans. Veh. Technol.*, vol. 60, no. 9, pp. 4115–4126, Nov. 2011.

[40] X. Lu, K. L. V. Iyer, K. Mukherjee, and N. C. Kar, “Investigation of integrated charging and discharging incorporating interior permanent magnet machine with damper bars for electric vehicles,” *IEEE Trans. Energy Convers.*, vol. 31, no. 1, pp. 260–269, Mar. 2016.

[41] N. Bodo, E. Levi, I. Subotic, J. Espina, L. Empringham, and C. M. Johnson, “Efficiency evaluation of fully integrated on-board EV battery chargers with nine-phase machines,” *IEEE Trans. on Energy Conv.*, vol. 32, no. 1, pp. 257-266 , Jan. 2017.

[42] J. de Santiago, H. Bernhoff, B. Ekergård, S. Eriksson, S. Ferhatovic, R. Waters, and M. Leijon, “Electrical Machine Drivelines in Commercial All-Electric Vehicles: A Review,” IEEE Trans. Veh. Technol., vol. 61, no. 2, pp. 475-484, Feb. 2012.

[43] K. T. Chau, "Stator-Permanent Magnet Machine Drives," in *Electric Vehicle Machines and Drives: Design, Analysis and Application*, Wiley-IEEE Press, 2015.

[44] J. G. W. West, “DC, induction, reluctance and PM machines for electric vehicles,” *Power Engineering J.*, vol. 8, no. 2, pp. 77-88, Apr. 1994.

[45] I. Boldea, L. N. Tutelea, L. Parsa and D. Dorrell, "Automotive Electric Propulsion Systems With Reduced or No Permanent Magnets: An Overview," in *IEEE Trans. on Ind. Electron.*, vol. 61, no. 10, pp. 5696-5711, Oct. 2014.

[46] G. Su and L. Tang, “Current source inverter based traction drive for EV battery charging applications,” in *Proc. IEEE VPPC*, Sep. 6-9, 2011, pp. 1-6.

[47] A. Gaeta, G. Scelba, and A. Consoli, "Modeling and control of three-phase PMSMs under open-phase fault," *IEEE Trans. on Ind. Appl*., vol. 49, no.1, pp. 74-83, Jan. 2013.

[48] D. Y. Ohm, “Dynamic model of PM synchronous machines,” Drivetech, Inc., Blacksburg, Virginia, www.drivetechinc.com 16 (2000).

[49] W. Qian, H. Cha, F. Z. Peng, and L. M. Tolbert, “55-kW variable 3X DC-DC converter for plug-in hybrid electric vehicles,” *IEEE Trans. on Power Electron*., vol. 27, no. 4, pp. 1668-1678, Apr. 2012.

[50] H. Chen, X. Wang and A. Khaligh, "A single stage integrated bidirectional AC/DC and DC/DC converter for plug-in hybrid electric vehicles," *2011 IEEE Vehicle Power and Propulsion Conference*, Chicago, IL, 2011, pp. 1-6.

[51] D. W. Hermance, “2007 Toyota Camry Hybrid,” presented at the SAE International Hybrid Vehicle Technologies Symposium, San Diego, CA, Feb. 1–2, 2006.

[52] H. C. Chen, C. Y. Lu, and L. M. Huang, "Decoupled Current-Balancing Control With Single-Sensor Sampling-Current Strategy For Two-Phase Interleaved Boost-Type Converters", *IEEE Trans. Ind. Electron*., vol. 63, no. 3,pp. 1507 - 1518, Mar. 2016.

[53] Y. K. Luo, Y. P. Su, Y. P. Huang, Y. H. Lee, K. H. Chen, and W.C. Hsu, "Time-Multiplexing Current Balance Interleaved Current-Mode Boost DC-DC Converter for Alleviating the Effects of Right-half-plane Zero", *IEEE Trans. on Power Electron*., vol.27, no. 9, pp. 4098 - 4112, Sept. 2012.

[54] C. Shi, H. Wang, S. Dusmez, and A. Khaligh, "A SiC-Based High-Efficiency Isolated Onboard PEV Charger With Ultrawide DC-Link Voltage Range," *IEEE Trans. on Ind. Applic.*, vol. 53, no. 1, pp. 501 - 511, Jan. 2017.

[55] F. Lacressonniere and B. Cassoret, “Converter used as a battery charger and a machine speed controller in an industrial truck,” in *Proc. Eur. Conf. Power Electro. Appl.*, 2005, pp. 7–P.7.

[56] B. Briane, and S. Loudot, “Rapid reversible charging device for an electric vehicle,” Patent US 20110254494 A1, 2011.

[57] S. Loudot, B. Briane, O. Ploix, and A. Villeneuve, “Fast charging device for an electric vehicle,” Patent US 20120286740 A1, 2012.

[58] A. Stupar, T. Friedli, J. Minibock, and J. W. Kolar, “Towards a 99% efficient three-phase buck-type PFC rectifier for 400-V DC distribution systems”, *IEEE Trans. on Power Electron*., vol. 27, no. 4, pp. 1732-1744, Apr. 2012.

[59] T. Nussbaumer, and J. W. Kolar, “Comparison of 3-phase wide output voltage range PWM rectifiers,” *IEEE Trans. on Ind. Electro*.,vol. 54, no. (6), pp. 3422-3425, Dec. 2007.

[60] T. Nussbaumer, and J. W. Kolar, “Comparative evaluation of control techniques for a three-phase three-switch buck-type AC-to-DC PWM converter system,” In Proc. of the 3rd IEEE Nordic Workshop on Power and Industrial Electronics, pp. 12-14, Aug. 2002.

[61] L. Schrittwieser, J. W. Kolar and T. B. Soeiro, "99% Efficient three-phase buck-type SiC MOSFET PFC rectifier minimizing life cycle cost in DC data centers," in *CPSS Transactions on Power Electronics and Applications*, vol. 2, no. 1, pp. 47-58, 2017.

[62] T. Nussbaumer, G. Gong, M. L. Heldwein, and J. W. Kolar, “Modeling and robust control of a three-phase buck+ boost PWM rectifier (VRX-4),” *IEEE Transactions on Ind*. Appl., vol. 44, no. 2, pp.650-62, Mar. 2008.

[63] C. Shi, A. Khaligh, and H. Wang, "Interleaved SEPIC Power Factor Preregulator Using Coupled Inductors In Discontinuous Conduction Mode With Wide Output Voltage," *IEEE Trans. on Ind. Applic.*, vol. 52, no. 4, pp. 3461 - 3471, Apr. 2016.

[64] C. Shi, Y. Tang, and A. Khaligh, "A Three-Phase Integrated Onboard Charger for Plug-in Electric Vehicles," *IEEE Trans. on Power Electron.*, vol. PP, no. 99, pp.1 - 1, 2017.

[65] S. Haghbin, S. Lundmark, M. Alakula, and O. Carlson, “Grid-connected integrated battery chargers in vehicle applications: Review and new solution”, *IEEE Trans. on Ind. Electron.*, vol. 60, no. 2, pp. 459-473, Feb. 2013.

[66] N. Sakr, D. Sadarnac, and A. Gascher, “A review of on-board integrated chargers for electric vehicles,” presented at the *Eur. Conf. Power Electron. Appl.*, Lappeenranta, Finland, CD-ROM, 2014.

[67] C. Shi, Y. Tang and A. Khaligh, “A Three-Phase High Power-Level Integrated Onboard Charger for Plug-in Electric Vehicles”, *IEEE Transactions on Power Electronics*, vol.33, no. 6, pp. 4716 - 4725, Mar. 2018.

[68] C. Shi, and A. Khaligh, “A Two-Stage Three-Phase Integrated Charger for Electric Vehicles with Dual Cascaded Control Strategy,” *Journal of Emerging and Selected Topics in Power Electronics*, DOI: 10.1109/JESTPE.2018.2797913, in press.

[69] C. Shi, Y. Tang and A. Khaligh, “A Single-Phase Integrated Onboard Battery Charger Using Propulsion System for Plug-in Electric Vehicles,” *IEEE Transactions on Vehicular Technology*, vol. 66, no. 12, pp. 10899–10910, Dec. 2017.

[70] C. Y. Oh, D. H. Kim, D. G. Woo, W. Y. Sung, Y. S. Kim and B. K. Lee, "A High-Efficient Nonisolated Single-Stage On-Board Battery Charger for Electric Vehicles," in *IEEE Transactions on Power Electronics*, vol. 28, no. 12, pp. 5746-5757, Dec. 2013.

[71] T. Bang and J. W. Park, "Development of a ZVT-PWM Buck Cascaded Buck–Boost PFC Converter of 2 kW With the Widest Range of Input Voltage," in *IEEE Transactions on Industrial Electronics*, vol. 65, no. 3, pp. 2090-2099, March 2018.

[72] C. Tse, M. Chow, and M. Cheung, “A family of PFC voltage regulator configurations with reduced redundant power processing,” IEEE Trans. Power Electron., vol. 16, no. 6, pp. 794–802, Nov. 2001.

[73] C. Yao, X. Ruan, W. Cao, and P. Chen, “A two-mode control scheme with input voltage feed-forward for the two-switch buck-boost dc-dc converter,” IEEE Trans. Power Electron., vol. 29, no. 4, pp. 2037–2048, Apr. 2014.

[74] B. Gu, J. S. Lai, N. Kees, and C. Zheng, “Hybrid-switching full-bridge DC–DC converter with minimal voltage stress of bridge rectifier, reduced circulating losses, and filter requirement for electric vehicle battery chargers,” IEEE Trans. Power Electron., vol. 28, no. 3, pp. 1132–1144, Mar. 2013.

[75] Z. Liu, B. Li, F. C. Lee and Q. Li, "Design of CRM AC/DC converter for very high-frequency high-density WBG-based 6.6kW bidirectional on-board battery charger," *2016 IEEE Energy Conversion Congress and Exposition (ECCE)*, Milwaukee, WI, 2016, pp. 1-8.

[76] F. Musavi, W. Eberle and W. G. Dunford, "A High-Performance Single-Phase Bridgeless Interleaved PFC Converter for Plug-in Hybrid Electric Vehicle Battery Chargers," in *IEEE Trans. on Ind. Applic.*, vol. 47, no. 4, pp. 1833-1843, July-Aug. 2011.

[77] B. P. McGrath, D. G. Holmes, P. J. McGoldrick, and A. D. McIver, “Design of a soft-switched 6-kW battery charger for traction applications,” *IEEE Trans. Power Electron.*, vol. 22, no. 4, pp. 1136–1144, Jul. 2007.